T.R.
GEBZE TECHNICAL UNIVERSITY
INSTITUTE OF NANOTECHNOLOGY

PtCu NANOPARTICLES SUPPORTED WITH GRAPHENE DERIVED MATERIALS: SYNTHESIS, CHARACTERIZATION AND THEIR USE AS ELECTROCATALYSTS IN PEM FUEL CELLS

ZEYNEP AYDIN
A THESIS SUBMITTED FOR THE DEGREE OF
MASTER OF SCIENCE
INSTITUTE OF NANOTECHNOLOGY

GEBZE
2021

T.R.
GEBZE TECHNICAL UNIVERSITY
INSTITUTE OF NANOTECHNOLOGY

PtCu NANOPARTICLES SUPPORTED WITH GRAPHENE DERIVED MATERIALS: SYNTHESIS, CHARACTERIZATION AND THEIR USE AS ELECTROCATALYSTS IN PEM FUEL CELLS

ZEYNEP AYDIN
A THESIS SUBMITTED FOR THE DEGREE OF
MASTER OF SCIENCE
INSTITUTE OF NANOTECHNOLOGY

THESIS SUPERVISOR
ASSOC. PROF. ŞÖLEN KINAYYİĞİT

GEBZE
2021

T.C.
GEBZE TEKNİK ÜNİVERSİTESİ
NANOTEKNOLOJİ ENSTİTÜSÜ

GRAFENDEN TÜREVLİ MALZEMELERLE DESTEKLİ PtCu NANOPARTİKÜLLER: SENTEZ, KARAKTERİZASYON VE PEM YAKIT HÜCRELERİNDE ELEKTROKATALİZÖR OLARAK KULLANIMLARI

ZEYNEP AYDIN
YÜKSEK LİSANS TEZİ
NANOTEKNOLOJİ ENSTİTÜSÜ

DANIŞMANI
DOÇ. DR. ŞÖLEN KINAYYİĞİT

GEBZE
2021

GEBZE TEKNİK ÜNİVERSİTESİ	**YÜKSEK LİSANS JÜRİ ONAY FORMU**

GTÜ Fen Bilimleri Enstitüsü Yönetim Kurulu’nun 22/01/2021 tarih ve 2021/03 sayılı kararıyla oluşturulan jüri tarafından 27/01/2021 tarihinde tez savunma sınavı yapılan ZEYNEP AYDIN’ın tez çalışması Nanobilim ve Nanomühendislik Anabilim Dalında YÜKSEK LİSANS tezi olarak kabul edilmiştir.

JÜRİ

ÜYE
(TEZ DANIŞMANI) : DOÇ. DR. ŞÖLEN KINAYYİĞİT

ÜYE : DR. ÖĞR. ÜYESİ OSMAN EKSİK

ÜYE : PROF. DR. NERGİS ARSU

ONAY

Gebze Teknik Üniversitesi Nanoteknoloji Enstitüsü Yönetim Kurulu’nun
…..…/…..…/..….… tarih ve ………/……... sayılı kararı.

İMZA/MÜHÜR

SUMMARY

PEM fuel cell (PEMFC) is an environmentally friendly energy conversion system that directly transforms chemical energy into electrical energy with water as a by-product. In order to use PEMFC commercially, it is necessary to reduce the production cost and increase its efficiency. At this stage, it is vital to decrease the amount of Pt catalysts in membrane electrode assembly unit (MEA) responsible for ~70% of PEMFC expenses.

In this thesis, five different carbon black-graphene nanoplatelets composite supported PtCu nanoparticles (NPs) were produced with synergistic contribution of a secondary copper metal, which is cheaper than platinum. Two methods, organometallic synthesis and thermal decomposition, were used to synthesize PtCu NPs under various conditions. The resulting materials were characterized by TGA, FT-IR, Raman, XRD, XPS, TEM, SEM-EDS. Electrochemical surface area (ECSA) were calculated by cyclic voltammetry (CV). Most effective synthesis method for supported PtCu NPs is the thermal decomposition under dynamic varigon gas at 300 ^{0}C for 1 hour.

In the second part, PtCu/CB:GNP (50:50), PtCu/CB:GNP (30:70) and PtCu/CB:GNP (70:30) were prepared by optimized thermal decomposition method to study the effect of carbon support ratios on electrochemical activity. According to ECSA values, all three catalysts were reported to be electrochemically superior compared to commercial %20 wt Pt on carbon Vulcan XC-72. We believe that the carbon corrosion and durability issues are minimized with the introduction of a hybrid support having GNP. Moreover, decrease of precious metal Pt without compromising from catalyst activity is achieved. Our studies will be towards direct investigation of such catalysts in PEMFCs.

Keywords: PtCu bimetallic nanoparticles, Bimetallic nanocatalyst, Graphene nanoplatelet, Carbon black, Organometallic synthesis, Thermal decomposition.

ÖZET

PEM yakıt pilleri (PEMFC), kimyasal enerjiyi doğrudan elektrik enerjisine dönüştürebilen ve bunu yaparken yan ürün olarak yalnızca su üreten çevre dostu bir enerji dönüşüm sistemidir. PEMFC'nin ticari olarak kullanılabilmesi için üretim maliyetinin düşürülmesi ve veriminin artırılması gerekmektedir. Bu aşamada, PEMFC giderlerinin ~% 70'inden sorumlu membran elektrot montaj ünitesindeki (MEA) Pt katalizör miktarını azaltmak hayati önem taşımaktadır.

Bu tezde, platinden daha ucuz olan ikincil bir bakır metalinin sinerjik katkısıyla karbon siyahı-grafen nanoplatelet kompozit destekli beş farklı PtCu nanopartikülleri (NP'ler) üretilmiştir. PtCu NP'leri farklı sentez koşulları altında sentezlemek için organometallik ve termal dekompozisyon olmak üzere iki sentez yöntemi kullanılmıştır. Elde edilen malzemeler TGA, FT-IR, Raman, XRD, XPS, TEM, SEM-EDS ile karakterize edildi. Elektrokimyasal yüzey alanları (ECSA), döngüsel voltametri (CV) ile hesaplandı. Destekli PtCu NP'ler için en etkili sentez yöntemi; varigon gazı altında 300 ^{0}C, 1 saat süren termal dekompozisyon olduğu raporlandı.

İkinci bölümde, elektrokimyasal aktivite üzerinde karbon destek oranlarının etkisini araştırmak için optimize edilmiş termal dekompozisyon yöntemi ile PtCu/CB:GNP (50:50), PtCu/CB:GNP (30:70) ve PtCu/CB:GNP (70:30) NP'ler sentezlenmiştir. ECSA değerlerine göre, üç katalizörün de elektrokimyasal olarak, ticari karbon Vulcan XC-72 destekli % 20 Pt'ye kıyasla daha üstün olduğu bildirildi. Bizler, GNP'ye sahip hibrit desteğin devreye girmesiyle karbon korozyonu ve dayanıklılık sorunlarının en aza indirildiğine inanıyoruz. Ayrıca, sentezlenen bu hibrit destekli NP'ler ile katalizör aktivitesinden ödün vermeden değerli Pt metalinin katalizör içindeki oranı azaltılmıştır. İleriye yönelik çalışmalarımız, doğrudan PEMFC'ler için bu tür katalizörlerin araştırılmasına yönelik olacaktır.

Anahtar Kelimeler: PtCu nanopartiküller, Bimetalik nanokatalizör, Grafen nanopletler, Karbon siyahı, Organometalik sentez, Termal dekompozisyon.

ACKNOWLEDGEMENTS

Throughout my graduate life, several people have helped me tremendously in bringing my thesis to this stage and gaining unique experiences. I owe a great debt of gratitude to these people, especially my supervisor, Assoc. Prof. Solen KINAYYIGIT. Thanks to her, I was able to scientifically improve myself and gain experience abroad by participating on an international project.

Ahmet Musap Mert, who goes beyond just being a colleague in a laboratory and is a true friend, deserves a special thank you. Thanks to him, we were able to successfully cope with several challenging issues in the lab. I am grateful to him for his supportive and helpful attitude throughout my master education.

I would like to thank Prof. S.C. Edman TSANG and Dr. Tugce AYVALI from the Department of Inorganic Chemistry at University of Oxford, where I had the opportunity to do an internship for 2 months, for all the scientific and emotional supports they provided me during my internship.

I also would like to appreciate all my colleagues at Şişecam Science and Technology Center for their patience and encouragement during this stressful period. I would also like to acknowledge Gebze University (BAP-GTU-SU-004 and 2019-A-101-17) and TUBITAK (Project No: 216-Z-124) for their financial support.

Among all these thanks, I owe the most special thanks to my dear family. I feel very lucky because of being a member of this family. In all kinds of difficult circumstances, my dear mother Kezban AYDIN and my brother Bilal AYDIN stand behind me and never stop supporting me. My dear father who passed away deserves the most special and most precious of thanks. I never cannot pay the labor of my dear father Hüseyin AYDIN, who raised me as an educated, self-confident and independent woman and made every sacrifice for my education.

This thesis is dedicated to my lovely father, who has always been in my heart.

TABLE of CONTENTS

LIST of ABBREVIATIONS and ACRONYMS

Symbols and Abbreviations	**Descriptions**
eV	: Electron Volt
nm	: Nanometer
BE	: Binding Energy
CV	: Cyclic Voltametry
ECSA	: Electrochemical Active Surface Area
FTIR	: Fourier-transform Infrared Spectroscopy
ICP-MS	: Inductively Coupled Plasma Mass Spectrometry
MNPs	: Metal Nanoparticles
NPs	: Nanoparticles
ORR	: Oxygen Reduction Reaction
PEMFCs	: PEM Fuel Cells
SEM	: Scanning Electron Microscopyy
TEM	: Transmission Electron Microscopy
TGA	: Thermogravimetric Analysis
XPS	: X-Ray Photoelectron Spectroscopy
XRD	: X-Ray Diffraction

LIST of FIGURES

LIST of TABLES

1. INTRODUCTION

Energy is one of the most important factors that determine the economic developments, living standards and competition power of the countries in the international arena. Nowadays, the need for energy is amplifing exponentially with the continuous increase in the world population, the increasing spread of industrialization and urbanization and the rapid progress in technological developments. For all these reasons, the investigation for alternative renewable energy sources and their usage areas have gained importance worldwide with the decrease in the reserves of fossil fuels, which have a crucial aspect of energy sector such as petroleum and natural gas, the release of harmful gases (especially CO and nitrogen oxides-NO_x) into the atmosphere and increased environmental issues awareness such as global warming [1].

Fuel cells are electrochemical conversion devices that directly convert the energy generated from the electrochemical reaction of a fuel into the direct current (DC) electricity in a single step and without any combustion steps. They are an ideal alternative energy source that operates with an energy efficiency of up to %70, uses the most abundant hydrogen element in nature as fuel and releases only water to the environment as a by-product. With these adventages, fuel cells can be one of the good alternatives to internal combustion engines currently in use and powered by fuels such as petrol or diesel [2].

There are various types of fuel cells such as Solid Oxide Fuel Cells (SOFCs), Alkaline Fuel Cells (AFC), Phosphoric Acid Fuel Cell (PAFC), Direct methanol fuel cells (DMFC), Molten Carbonate Fuel Cells (MCFC) and Polymer Electrolyte Membrane Fuel Cells (PEMFCs). Although they all have their own advantages and disadvantages, PEM fuel cells attract more attention than others with some unique features. These features can be listed as follows; low operating temperature (80 ^{0}C), good energy density, robustness and no greenhouse gases emissions such as CO_2 and use of existing air in the environment as the oxidant [3].

PEM fuel cells are electrochemical cells where two basic electrochemical reactions take place. These reactions are the oxidation of hydrogen (hydrogen oxidation reaction) at the anode and the reduction of oxygen (oxygen reduction reaction) at the cathode and they enable hydrogen to turn into water by electrochemical combustion and to obtain energy with zero emission. Both reactions require catalysts to proceed. However especially the reduction reaction occurring in the cathode region is critical because it directly affects the efficiency and the cost of the PEM fuel cells [4]. The sluggish rate of the oxygen reduction reaction (ORR) requires more catalyst loading in the cathode region and this is the most important limit for the commercialization of PEM fuel cells. In addition to this negative situation, the formation of the reduction product hydrogen peroxide (H_2O_2), - by using two electrons in the reaction mechanism prevents the transfer of four electrons that is necessary for ORR. The formation of hydrogen peroxide also dramatically affects the decomposition rate of organic compounds in the reaction environment [5].

Therefore it is very important to use the right catalyst to prevent all these negative factors. The catalytic activities and stabilities of selected catalysts in reaction conditions for PEM fuel cells should be high. Platinum is the most efficient catalyst that is widely used in fuel cells, petroleum chemicals and energy industries because of its unique catalytic properties such as long service life, its remarkable catalytic performance, unsaturated d-orbital ($5d^9$ $6s^1$) and resistance to lose its valence electrons [6]. However, Pt is a very expensive element with low abundance in the nature. These facts increase the cost of PEM fuel cells and negatively affects its competitive ability with other energy sources. Recently, cost-effective and highly active new types of ORR (oxygen reduction reaction) electrocatalysts prepared with Pt and less expensive and less noble 3d transion metals (Cu, Ni, Co, etc) alloys are found promising solution to obtain reasonably priced fuel cells. This type of Pt-based nanoparticles is catalytically more active compared to pure Pt catalyst due to change in the d-band position [4]. In addition, Pt-based nanoparticles' activities strongly depend on the distribution, size and shape of the nanoparticles. For all these reasons,the control should be provided on the three factors (distribution, size and shape) mentioned above to obtain the catalyst with the best activity under specific reaction conditions [7].

Many physical or chemical methods such as chemical reduction, sound waves, UV radiation, thermal decomposition, chemical vapor deposition (CVD) or electrochemical synthesis are used in the preparation of nanoparticles as catalysts [8]. Apart from these synthesis methods, organometallic synthesis is very useful for obtaining well-controlled nanostructures. Organometallic approach uses, metal-organic complexes as the source of metal nanoparticles and based on the reduction of these complexes under mild reaction conditions and presence of gas pressure, offers significant advantages for the synthesis of controllable nanostructures [9]. With well-tuning of the reaction parameters, organometallic synthesis method expands the control area on critical issues such as size distribution, chemical composition, surface condition and size of metal nanoparticles and paves the way for the formation of well-defined nanostructures.

Insufficient durability that is mainly associated with ORR electrocatalyst in use at the cathode is one of the most important obstacle to commercialization of fuel cells [10]. Today, carbon-supported Pt electrocatalysts are still widely used in PEM fuel cells. Present investigations indicate that the carbon-based electrocatalyst support materials play a critical role in the activity and stability of the catalyst [11]. It has been recognized that choosing the right support material affects the durability of the electrocatalyst by preventing catalyst degradation, Pt dissolution, sintering and agglomeration during the fuel cell test [12]. Although carbon black is currently the most available support material for fuel cell catalysts, it is oxidized in the presence of oxygen throughout long fuel cell operation. This carbon oxidation is called carbon corrosion and results in the separation of Pt particles from the support material [11]. Hence, it is essential to explore and utilize more durable catalyst support materials to enhance the activity and satability of PEM fuel cell catalysts [13].

Carbon support materials include carbon black (CB) [14], carbon nanotubes (CNTs) [15], carbon nanofibers (CNFs) [16], mesoporous carbon spheres [17], graphenes [18], and others are still the most popular and practical for Pt-based electrocatalysts as support materials because of several properties [19]. However among them, graphene has attracted a great deal of attention as a new generation of promising support material for PEM fuel cells due to its unique physicochemical properties such as huge specific surface area, excellent electrical/thermal conductivity, great mechanical strength and quick charge transport mobility [20].

In the first part of this thesis study, by using the synergistic interaction of CB and graphene-derived graphene nanoplatelet (GNP) materials, hybrid CB:GNP (50:50) carbon supported five diffrent PtCu electrocatalysts were synthesized under various synthesis methods and conditions in order to explore the synthetic conditions for a potential electrocatalyst. Investigation of the tuning of the properties of the bimetallic PtCu NPs was made with the change of reaction parameters. Produced PtCu NP samples were fully characterized with ICP-MS, TGA, XRD, XPS, TEM, SEM-EDS and FTIR and Raman spectroscopies. Finally, cyclic voltammetry (CV) analyses were carried out in order to understand the effect of structural differences in nanoparticles on their electrochemical properties in an attempt to use them as potential electrocatalysts for PEM fuel cells.

The key idea of the second part of the thesis is to evaluate the influence of varying carbon support ratios on bimetallic nanoparticle creation and carbon corrosion that may appear during electrochemical tests. Adhering to this purpose, the thermal decomposition process, which gives the best electrochemical results under dynamic varigon gas at 300 ^{0}C for 1 hour, was preferred as the synthesis method for all catalysts synthesized in this section. Three different bimetallic electrocatalysts, PtCu/CB:GNP (50:50), PtCu/CB:GNP (30:70) and PtCu/ CB:GNP (70:30), were synthesized in accordance with this synthesis condition. In addition to these catalysts, using the same synthesis method, monometallic Pt/CB:GNP (50:50) and Cu/CB:GNP (50:50) supported NPs were also synthesized to further investigate the synergistic interaction of Pt and Cu elements both structurally and electrochemically in bimetallic structures. Structural characterizations of these five different nanostructures were made by ICP-MS, XRD, TEM, SEM-EDS and Raman spectroscopy. Electrochemical surface area (ECSA) values of both mono- and bimetallic nanostructures were compared with the commercial 20% wt Pt on carbon Vulcan XC-72 catalyst by CV technique.

1.1. Synthesis Techniques of Nanostructures

With the development of nanotechnology, the way has been opened for the creation of nanostructures with quite different physical and chemical properties than those of bulk structures. A substance including particles, aggregates, and filaments smaller than 100 nm is considered as a nanomaterial [21]. They are greater in size than individual atoms and molecules, but nonetheless smaller enough with different properties compareded to bulk solids. Thus, they do not follow either absolute quantum chemistry nor classical physics principles and hence have properties that vary greatly from those predicted [22].

Small-sized particles with a very large ratio of surface area-to-volume are created by the reconfiguration and production of nanomaterials. This property of nanomaterials has contributed to enhancement of optical, electrical, mechanical and functional characteristics of matter. In addition, nanotechnology is mainly accountable for the success of this promising modern interdisciplinary technology at diverse potential application areas such as drug, medicine, textile, food, agriculture and energy [21,23].

Especially, for metal NPs, the electronic features, such as conductivity, magnetism, etc., vary widely from bulk metal because the electronic states in the valence band and the conductivity band decrease to such a degree that the electronic properties change significantly with the decrease in size. The quantum size effect indicates that the electronic state of matter decreases continuously from the bulk system (three-dimensional system) to the quantum dots (zero-dimensional system) (Figure 1.1) [24,25].

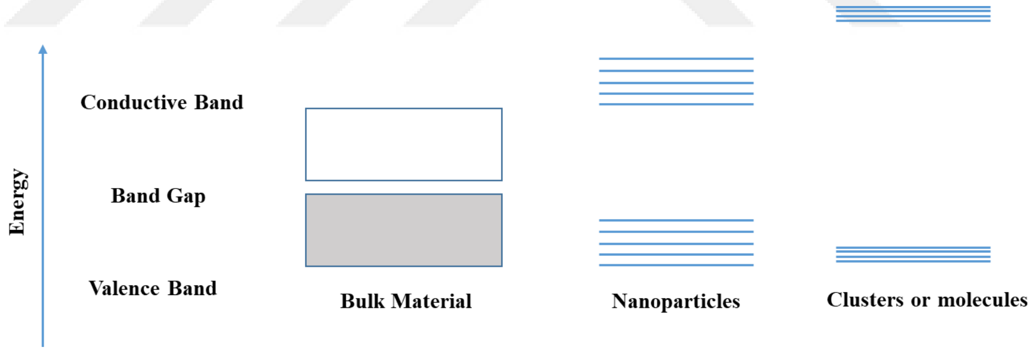

Figure 1.1: The electronic state of matters.

Being able to explain how nanoparticles (NPs) are formed by chemical processes is one of the most important points for their manipulation of well-defined structure and size. For this purpose, many scientists have conducted studies to explain the formation process of nanostructures. Among these scientists, the studies of LaMer, Turkevich and Finke are particularly striking [26,27].

The production of sulphur sols from the degradation of sodium thiosulfate in hydrochloric acid was explained by LaMer in 1950. In the principle put forward with this study, it was claimed that homogeneous nucleation continues until a nucleus of critical size is obtained [26]. Following LaMer’s studies, Turkevich and his co-workers attempted to describe the stepwise formation of gold NPs focused on nucleation, growth, and agglomeration via electron microscopy [28]. Afterwards , Finke and Watzky announced a two-step procedure for the reduction of metal salt in 1997, and then a more general procedure for the creation of transition metal nanoclusters was documented [29].

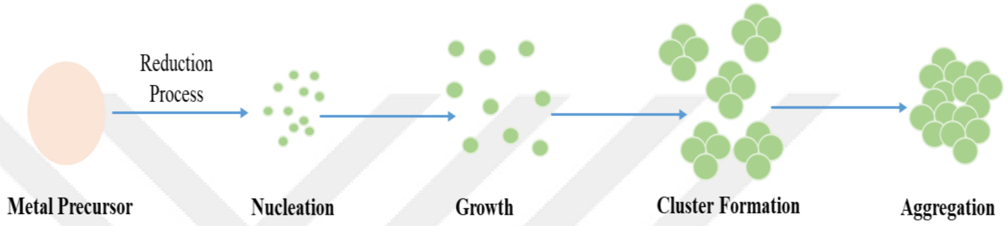

Figure 1.2: A representation of formation of NPs: nucleation, growth and aggregation processes during the synthesis.

Three stages simplify the basic mechanistic construction of NPs; nucleation, growth and agglomeration (Figure 1.2). Factors that influence particle size, shape and composition are dependant on the difference between the redox potential of the metal salt, the reducing agent, and the reaction conditions (the rate of addition, the reaction temperature etc). Metal salt in the reaction medium is reduced in the first step of the nucleation process to provide zero-valent metal atoms. These metal atoms then collide with other atoms around them, forming first permanent seeds of durable metal nuclei. Depending on the quality of the metal-metal bonds and the difference between the redox potential of the metal salt and the reducing agent added, the diameter of the "seeds" could be well below 1 nm [26,30,31].

In fact, in all forms of nanostructures, the control of size and shape is a consideration, as both would have an influence on the substance's physical and chemical characteristics [32]. In order to understand the characteristics of the products, various forms of rules can be implemented depending on the size and shape of the nanostructures. For this purpose, there are a number of fabrication techniques for nanostructures in the literature. The key parameters for the effectiveness of these different techniques can be described as 1. control of scale, shape, crystal structure, 2. prevention of nanoparticle agglomeration, 3. Use of eco-friendly precursors 4. amount of harmful by-product and 5. stable chemical and physical properties of synthesized nanostructures [33–35].

All synthetic methods in literature for the production of nanomaterials can be grouped into two main procedures; these are called, bottom-up and top-down methods (Figure 1.3). Top-down method involves reducing bulk structure to nano-size by physical methods such as cutting and abrasion. It starts from larger structures until the designed shape and structure is obtained. This approach has an effective success especially in the design of semiconductor devices offered to the consumer and it is used effectively in miniaturizing the components of more efficient and fast high-tech machines and devices [35].

There are various physical methods to obtain micro / nano sized structures using the top-down approach. Among these methods, the most commonly used by the electronics industry are; lithography (photolithography, X-ray lithography, and electron beam), mechanical milling, wet and plasma etching and sputtering [33,36]. These techniques are more expensive than bottom-up methods and require advanced equipments for the production.

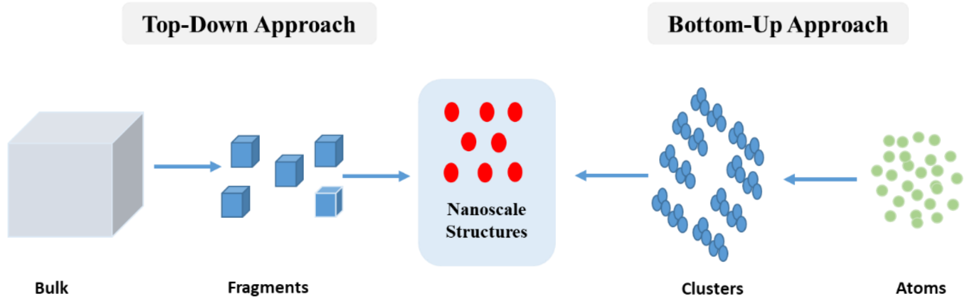

Figure 1.3: Schematic representation explaining top-down and bottom-up approaches in nanoparticle synthesis.

In contrast to the top-down approach, the bottom-up approach involves arrangement and organization of individual elements such as atoms, molecules and biological cells to create a nano-sized structure by the direct manipulation of atoms or molecules. In bottom-up technique, atoms or molecules form nano-sized units by self-assembly with physical and / or chemical interactions [36].

These methods allow nanoparticle synthesis in two different media, liquid and gas phase. Unlike top-down methods, nanostructures of a wide variety of sizes and structures such as 0 D, 1D, and 2D can be synthesized with simple chemical equipment via bottom-up approach. In addition to all these, the morphology, size and shape of nanoparticles can be easily manipulated by making small changes such as temperature, pressure, precursor used in the synthesis method [26].

There are a variety of approaches to produce nanostructures that are well defined in shape and size using the bottom-up technique. Examples of these approaches are; chemical vapor deposition (CVD), chemical reduction, electrochemical method (electrolysis), microemulsion method, pyrolysis, photochemical (irradiation) method, solvothermal / hydrothermal synthesis, sol-gel process, sonochemical method, thermal decomposition, green synthesis approach and organometalic synthesis approach.

1.1.1. Chemical Vapor Deposition (CVD)

CVD, one of the bottom-up synthesis methods fort he production of nanostructures, is defined as chemical vapor deposition on the relevant substrate in a chamber under high temperature and pressure [37]. Thanks to this method, two dimensional (2D) nanostructures can be formed on the desired substrate in the presence of a catalyst or without a catalyst [38]. CVD method is often preferred for synthesis of 2D materials because of the creation of high purity and high quality crystal structures and allowing large scale production with limited defects on the substrate [39].

In the CVD method, gas phase reactive precursors with sufficient activity can either deposit on the substrate and/or react with the substrate to form the designed thin film on the substrate that held in the chamber (Figure 1.4). While reaction or/and decomposition occurs on the substrate, by-products formed as a result of side reactions are removed with the carrier gas dynamically passing through the system [40].

By using the CVD method, 2D structures (e.g graphene, h-BN nanosheets, transition metal dichalcogenides (TMDs) , metal carbides, borophenes, antimonene, silicone) that are used in especially optical, electronic and semiconductor technologies can be synthesized in large scale [39–41].

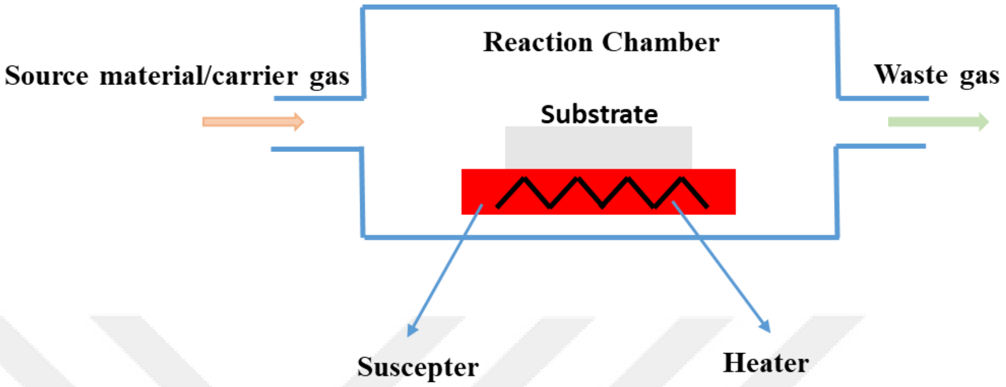

Figure 1.4: A Schematic of conventional CVD reactor.

1.1.2. Chemical Reduction Method

Chemical reduction (Figure 1.5) is a common synthesis method especially to obtain graphene from graphene oxide and metal nanoparticles (MNPs) from various metal salts. It is a cost-effective and simple technique with the use of simple laboratory equipments [42]. In the chemical reduction method, the most necessary material for the formation of nanostructures is the careful selection of the reducing agents. These reducing agents reduce the metal ions that act as nuclei in the reaction environment and nanoparticle growth occurs on these nuclei. Phenyl hydrazine, ascorbic acid, hydroxylamine, hydroquinone, glucose, sodium borohydride, alkaline solutions, and pyrrole are among the chemicals that are often used as chemical reducing agents [42–44].

Strong reducing agents allow the formation of smaller NPs compared to weak reducing agents. However, as the NP size decreases, the surface energy increases and extreme thermodynamic instability occurs. NPs are susceptible to agglomeration due to Ostwald ripening and rapidly nucleate [45]. In order to prevent agglomeration and preserve their stability, various cappling agents (stabilizers) such as ligands or polymers (polyvinyl pyrrolidone (PVP), polyacrylates, polyacrylamides, poly(ethylene glycol)

(PEG), polyvinyl alcohol (PVA) etc.) are used to keep the nanoparticles stable and prevent their coalescence [46,47].

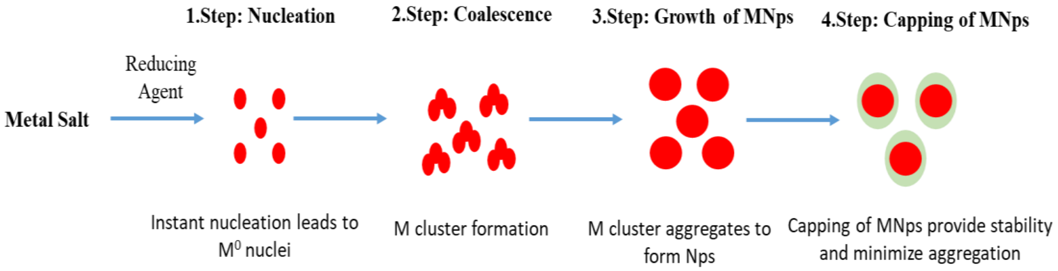

Figure 1.5: Schematic representation of chemical reduction method for the formation of MNPs.

1.1.3. Electrochemical Method

Electrochemical method, another chemical method used in MNP synthesis, is worth mentioning since it usually allows obtaining NPs with desired size and shape by adjusting the current density [48]. Using this synthesis method, high purity MNPs can be obtained quickly and easily. In addition to being a fast and simple method, it has taken its place in the literature as an eco-friendly synthesis method, since no environmentally hazardous reducing agents nor any toxic chemicals are used in MNP formation via this method [49].

Nanoparticle production by simple electrochemical reaction is as follows; the bulk metal structure at the anode region is oxidized and then formed metal cations migrate to the cathode region where reduction occurs to produce metal or metal oxide NPs in the zero oxidation state (Figure 16.) [50]. During the NP formation reaction, stabilizing agents such as polymers and surfactants are used to avoid undesirable by-products and also to obtain MNPs with desired properties [51–53].

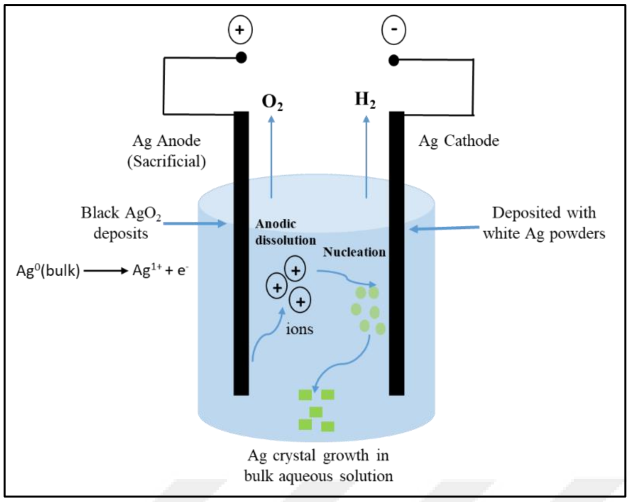

Figure 1.6: Experimental set-up of electrochemical formation of Ag NPs in distilled water.

1.1.4. Microemulsion Method

Microemulsion technique, which is one of the methods developed for the synthesis of nanomaterials, can prevent the growth and aggregation of NPs. Microemulsion synthesis method, also known as reverse micelle synthesis, offers versatile and reproducible NP synthesis and has an advantage over other synthesis methods such as CVD and elecrochemical methods in terms of forming homogeneous and monodispersed nanoparticles of various metals, oxides and chalcogenites [54,55].

In the synthesis of several types of NPs, reverse micelles (Figure 1.7) are commonly used today as nanosized aqueous droplets found in many formulations of water-in-oil microemulsions. The reaction takes place in aqueous core of reverse micelles, which can be dispersed in an organic solvent and stabilized with a surfactant [56,57]. The dimensions of the aqueous core are nanoscale and the product obtained at the end of the reaction is homogeneous [58].

The synthesis of a simple compound such as AB using the microemulsion synthesis method is carried out as follows; first, two identical microemulsions are prepared and two different reactants (A and B) are added into these two microemulsions, and then these two microemulsions are mixed and the resulting mixture is left to mix continuously. The droplet collision results in reactant exchange, during which the reaction takes place within the droplets that serve as a nanoreactor. The two reverse micelles form an encounter pair (EP) which, after collision, transforms to a fused dimer (FD). Because of the large surface area, the surface tension of the FD becomes very high and it can not maintain its geometry. The FD breaks down into two smaller stable droplets containing the substance precipitated.

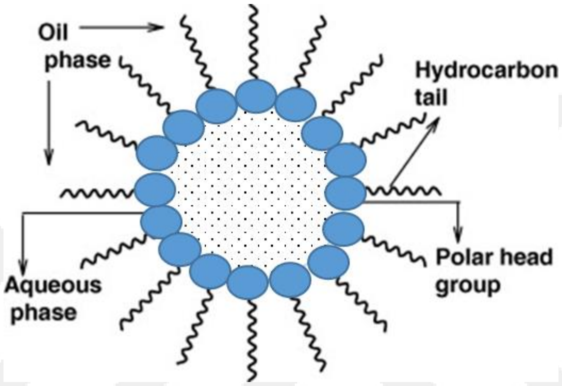

Figure 1.7: A typical reverse micellar structure.

1.1.5. Pyrolysis Synthesis Method

In the pyrolysis method, one of the frequently used methods in the NP synthesis, the main aim is to isolate the solute and the solvent from the solution, which is carried out by heating the solution This process evaporates the solvent and finally creates the NPs [59]. The most frequently used technique in the pyrolysis process is the spray pyrolysis where the solution of the precursor is sprayed in very small droplets and then the aerosols of these droplets are heated and/or diluted to evaporate the solvent from the environment [60]. Each droplet is usually converted into a single product particle in the manufacture of microparticles by spray pyrolysis. However, in order to obtain NPs (<100 nm) using the spray pyrolysis method, either impractical small droplets or impractical precursor solutions at very low concentrations are required. Therefore, it is desired to produce a number of NPs from each precursor droplet [59,61].

1.1.6. Photochemical (Irradiation) Synthesis Method

Photochemical synthesis (Figure 1.8) depends on the absorption of photons (of usually visible, UV or VUV (vacuum ultraviolet)) by a photochemically active compound which in return rearranges or decomposes into reactive species called radicals. In photochemical processes, the photons must be absorbed by the active compound (i.e there is an overlap between the emission spectrum of the light source and the absorption spectrum of the irradiated medium); or else, most of the light would pass through the solution without doing any reaction. Then, rapid chemical reactions are triggered by the generated reactive radicals, leading to the formation of various intermediates or products [62,63].

The solvent used in the photochemical synthesis method is a very critical parameter. Chlorine-containing solvents are generally not preferred in this type of synthesis as they may cause chlorination of the substrate. While strong absorbent solvents intercept photons from reaching the substrate, hydrocarbon-based solvents can be used in photochemical synthesis because they absorb shorter wavelengths [64].

The key advantages of photochemistry are the ability to conduct chemical reactions by altering the strength of the irradiation light and simple scale-up of the reaction. In addition to all these advantages, photochemical synthesis is a cost-effective and relatively an environmentally friendly method since there is no need for dangerous and expensive materials during synthesis compare to with hazardous chemical reducing agents [62,65].

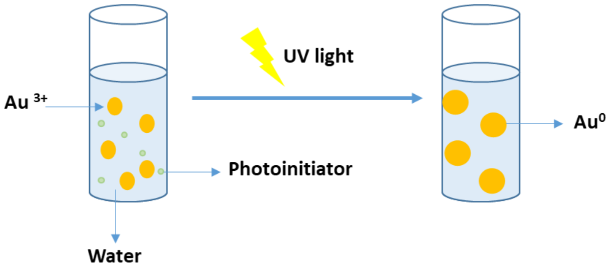

Figure 1.8: Schematic representation of gold NP synthesis by photochemical method.

1.1.7. Solvothermal / Hydrothermal Synthesis Method

Solvothermal reactions are defined as chemical reactions that take place at a temperature above the boiling point of the solution with a reaction pressure above 1 bar and are often preferred especially for the synthesis of metal oxide NPs such as Fe_2O_3, NiO, Co_3O_4, CeO_2, MgO, and CuO [66,67]. The medium in which the reaction takes place can be any solvent; from water to alcohol, organic or inorganic solvent. The term “hydrothermal” is used when the reaction medium is water and again the synthesis occurs in a closed vessel at a controlled temperature and pressure. In these two synthetic methods, since high pressures are used to obtain NPs, the reactions take place in autoclaves which are pressure-resistant sealed containers.

In addition to metal oxides, by using this process, free metals, chalcogenides, pnictides, and other materials can also be synthesized. The use of eco-friendly solvents for particle growth and homogeneous nucleation is the key benefit of hydrothermal synthesis. With control of different reaction parameters, such as pH, temperature, pressure, time, medium of reaction, and concentration, direct crystal structure formation of nanomaterials from the solution allows the rate and the uniformity of product nucleation, growth and oxidation to be properly regulated. Therefore, in this process, the scale, morphology, structure, and properties of materials are well regulated [68,69].

1.1.8. Sol-Gel Synthesis Method

Hydrolysis and polycondensation reactions are the basis of the chemistry of the wet chemical sol-gel process (Figure 1.9) [70]. A metal alkoxide dissolved in an appropriate solvent, mostly ethanol, is the precursor for the synthesis. The substance is hydrolyzed by the addition of a little water and that becomes a polymeric material, generally assisted by making the solution slightly acidic. A loose gel with liquid filled pores is the resulting substance, which could be transferred to a surface via dipping. Liquid elimination and material densification is accomplished by thermal treatment; the higher the temperature, the denser the resulting film would be. If complete densification is required, temperatures of 600 ° C, often even up to 1000 ° C, can be used. The benefit of using this technique is the construction of an inorganic network primarily linked to polymeric materials, particularly with noncovalent interactions [71,72].

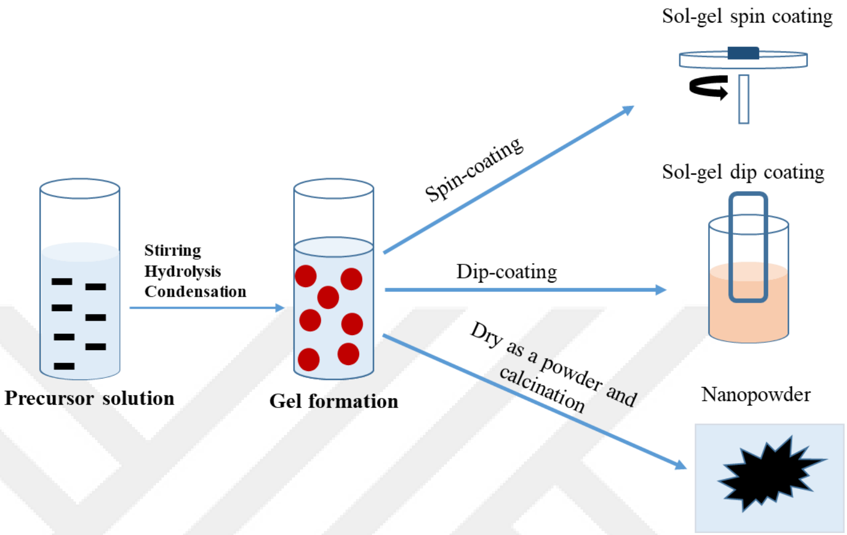

Figure 1.9: A simple representation of the sol-gel process pathway.

1.1.9. Sonochemical Synthesis Method

The scientific field in which molecules undergo chemical reaction due with the use of strong ultrasound radiation (20 kHz-10 MHz) is sonochemistry. This method in the production of nanostructures is a well-defined and well-researched area due to its simplicity and diverse applicability [73,74].

The accoustic cavitation is the physical phenomenon essential 15ort he sonochemical method. This can be separated into three main phases: (i) formation, (ii) growth, and (iii) bubble implosive collapse in a liquid that generates high pressure and temperature, accompanied by high cooling speeds [73,75,76]. These mechanisms are primarily accountable 15ort he selective and well-defined shape and size nanoparticle synthesis [77].

Using the ultrasonic process, nanomaterials can be easily synthesized. In addition, in the following aspects relevant to nanomaterials, the sonochemical approach contributes to all other techniques: (i) preparation of amorphous products; (ii) injection of nanomaterials into mesoporous materials; (iii) deposition of nanoparticles on ceramic and polymeric surfaces; and (iv) regulation of nanomaterial morphology [73].

1.1.10. Thermal Decomposition Method

Thermal decomposition is one of the effective method for especially synthesis of inorganic NPs to generate stable monodisperse suspensions with the capacity for self-assembly [78]. It is much faster, safer and also more economical than traditional approaches such as super critical techniques, metal salt reduction, microwave heating, micro emulsion techniques etc. In this method, nanoparticle nucleation takes place when the metal precursor is applied to a heated solution in the absence of a surfactant, while the growth state occurs at a higher reaction temperature [79].

Many different metal precursor such as inorganic and organic salts and metal-organic frameworks (MOFs) structures can be used to obtain metal nanoparticles using thermal decomposition synthesis method [79,80]. The direction of decomposition of the precursor dependent on the characteristics of gaseous environment prevailing during the heating process, the heating schedule itself and the organic group characteristics [81].

1.1.11. Green Synthesis Approach

Green nano-technology (Figure 1.10) usually indicates the synthesis of nanoparticles or nanomaterials by means of biological pathways, including some micro-organisms, plants and viruses or their components, such as proteins and lipids, with the assistance of various biotechnological instruments [34,82]. Green synthetic techniques contain polyoxometallates, polysaccharides, tollens, irradiation, and biological mixed-valence approaches. All of these approaches reduce the use of costly chemicals, require less energy and produce ecologically responsible products and by-products. The dry biomass of the plants and metallic salt, as bioreducing agent and precursor respectively, have been used in the general green synthesis procedure using plants to obtain MNPs [34].

For the production of nanomaterials based on green synthesis, three principal steps should be followed: (i) the preference of a solvent that using as medium, (ii) the selection of an environmentally safe reduction agent and (iii) the choosing of an ecofriendly and nontoxic material as a capping agent for the stabilization of the synthesized NPs [83].

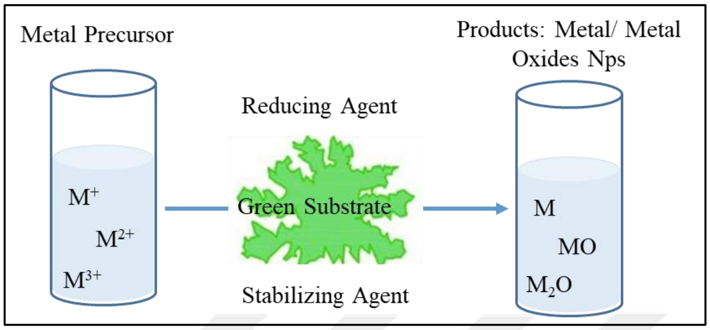

Figure 1.10: A simple representation of the green synyhesis process for production of metal/metal oxides NPs.

1.1.12. Organometallic Synthesis Approach

Organometallic synthesis (Figure 1.11) method is one of the methods developed to provide complete control over the size, shape and distribution of nanostructures [84]. In the existence of appropriate stabilizing agents, which may be multiple functional molecules including such surfactants, polymers, dendrimers, etc., the organometallic synthesis method relies on the use of metal complexes as the source of metal and their reduction or decomposition [85,86].

The use of organometallic precursors enables the synthesis of MNPs showing a regulated scale, shape and surface environment in mild reaction conditions. The method of synthesis involves the removal of ligands from an organometallic complex under mild conditions (room temperature or below, low gas pressure), with minimal or desirably no polluting reactants. The appropriate example is the dihydrogen reaction of an olefinic precursor that leads to the formation of an alkane that is unable to develop a strong bond with the expanding metal surface in these circumstances. To create NPs, the naked atoms formed in these conditions can condense.

Utilizing reactive gasses such as H_2 or CO to achieve naked zerovalent metal atoms, the decomposition prosses are carried out [87]. All of these naked atoms will decide to be closer to each other in order to create permanent seeds. Until the through reaction, regulation of size and prevention of agglomeration are crucial. Therefore stabilizers generate a steric barrier surrounding MNPs via chemical or physical connections between the surface of the NP and the stabilizer. The stabilizers such as polymers and dendrimers restrict the uncontrolled growth of particles by electrostatic forces resulting from ligands or sterical hindrance coordination. Olefinic and allylic complexes are commonly used metal precursors since they are reduced with the use of dihydrogen pressure under relatively mild conditions and ligands, turning into alkanes that avoid from the attachment of NPs surfaces. Tris-Allyl Rhodium ($Rh(C_3H_5)_3$), bis-1,5-cylooctadiene nickel (Ni $(COD)_2$), 1,5-Cylooctadiene 1,3,5-cylooctatrien ruthenium (Ru(COD)(COT)), tetra-allyl dirhenium ($Re_2(C_3H_5)_4$) are some of the examples for this kind of organometallic complexes which are efficiently able to decompose [85,86,88].

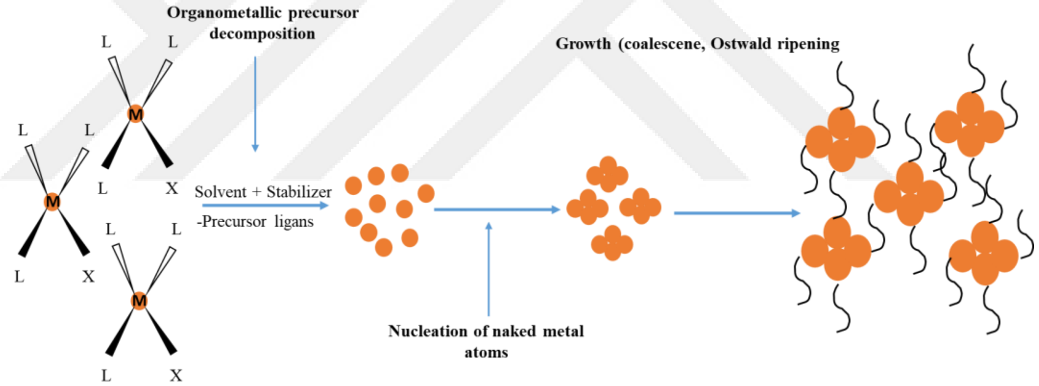

Figure 1.11: Representation of organometallic approach for production of MNPs.

1.2. Electrocatalysts towards PEM Fuel Cells: Working Principles, Catalyst and Support Materials

1.2.1. Operation Principle of PEM Fuel Cells

Unlike conventional combustion technologies, fuel cells (Figure 1.12) obtain electrical energy by converting the chemical energy of a fuel directly into an electrical signal as a result of electrochemical reactions. Although fuel cells are similar to batteries in many respects, they do not need to be recharged periodically like batteries to produce electricity. As long as the fuel source is provided, fuel cells can continue to generate electrical energy. The main reason for this difference is that the fuel cell is continuously fed with fuel and air (or O_2) from an external source. Contrary to this situation, batteries have a limited amount of fuel and oxidant that they use up [89,90].

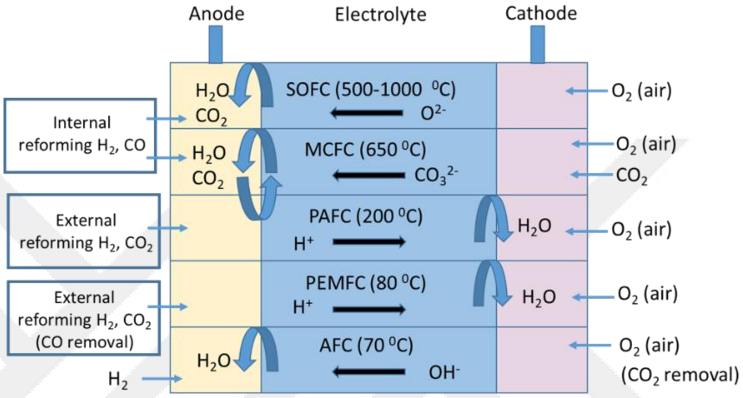

Figure 1.12: The basic scheme of different fuel cells.

Electrochemical reactions occur in fuel cell:

Anode: $2H_2 \rightarrow 4H^+ + 4e^-$

Cathode: $O_2 + 4H^+ + 4e^- \rightarrow 2H_2O$

Overall: $2H_2 + O_2 \rightarrow 2H_2O$ + Energy

Proton exchange membrane (PEM) fuel cells, which can transform chemical energy directly to electrical energy, attract considerable interest due to their superior advantages such as high power density, high efficiency of energy conversion, quick start-up, low orientation sensitivity, and environmentally friendly nature. A schematic representation of a simple PEM fuel cell is showed in Figure 1.13. As can be understood from Figure 1.13, the most important component of PEM fuel cells is the membrane electrode assembly (MEA), and this structure consists of two electrodes (anode and cathode) with a catalyst layer, a polymer membrane separating these electrodes, and a gas diffusion layer (GDL). The polymer membrane that separates the anode and cathode electrodes from each other consists of Nafion and acts as an electrolyte in the environment during the fuel cell test and ensures that the protons formed in the anode are transmitted to the cathode [91].

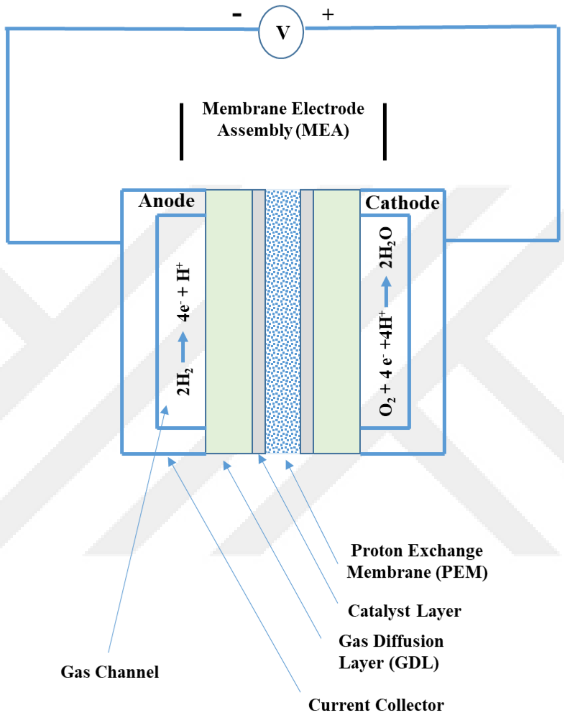

Figure 1.13: The schematic representation of a simple PEM fuel cell.

During the fuel cell test, the fuel (e.g. H_2) is oxidized with the aid of the catalyst layer in the anode region, thereby producing both electrons and protons. These protons are then transported to the cathode area along the PEM membrane, while the generated electrons are carried to the cathode electrode with the help of the external circuit. These protons and electrons that reach the cathode area then interact electrochemically with the oxidant in the catalyst layer that namely oxygen in the feed air, and generate water and heat. In summary, electricity, water and heat are produced during a PEM fuel cell test without creating any environmentally harmful by-products [92,93].

The most important problem arising in the commercialization of PEM fuel cells is the expensive nature of the MEA structure [94,95]. Today, many studies are carried out to eliminate this problem and to develop the membrane where only H^+ passage is allowed, catalyst layer and GDL layers in order to expand the usage areas of PEM fuel cells. For this purpose, various membranes have been developed for use in the PEM fuel cell, namely perfluorinated (PFSA, PFCA, PFSI), partially fluorinated (PTFE-g-TFS and PVDF-g-PSSA), non-fluorinated (NPI, BAM3G, SPEEK, SPPBP, MBS-PBI), acid-base blends (SPEEK/PBI/P4VP, SPEEK/PEI, SPSU/PBI/P4VP etc.) and supported composite membrane [93].

The gas diffusion layer (GDL) layer, another component in the PEM fuel cell, is porous to provide gas permeability, and because of its porous nature, carbon papers are often used in PEMFC as GDL layer. Another PEM fuel cell component that is located between the membrane and GDL layer and plays a major role in the cost of the MEA structure is the catalyst layer. In this layer, the catalyst is distributed over a support material to ensure stability and prevent agglomeration and provide high performance throughout fuel cell performance. The type of catalyst used commercially in PEM fuel cells is carbon supported Pt catalyst [92,96]. However, due to the expensive and scarce nature of Pt metal, many studies have been done and continue to be done in the literature in order to lower the catalyst cost in PEM fuel cells. Details of the catalyst and support material types used in PEM fuel cells are discussed under their respective titles in the following sections.

1.2.2. Oxygen Reduction Reaction (ORR) Mechanism in PEMFC

Despite its being environmentally friendly, highly efficient and with high power density, the most important factor in the commercialization of PEM fuel cells is the very high production cost. In particular, the cost of the catalyst layer required for faster and more efficient redox reactions mentioned in the previous chapters is one of the most important obstacles to the spread of PEM fuel cells. In addition to the expensive catalyst layers, the short operation time of membranes used in PEMFCs makes it a priority research topic to increase the durability throughout the PEMFC performance [97]. In addition to all these issues, one of the most significant barriers for the use of this technology, especially in public transport systems, is that it is not yet fully developed to provide an adequate hydrogen storage system [98].

For the release of energy in PEMFCs, two important electrochemical reactions must occur efficiently. The first of these is the hydrogen oxidation reaction (HOR) occurring in the anode part and the other is the oxygen reduction reaction (ORR) occurring in the cathode part. At this point, it is important to understand the kinetics and mechanism of these redox reactions occurring in the PEMFCs [99].

As opposed to HOR, the rate of ORR is rather sluggish and has a more chemically complex reaction mechanism. Among with these adverse effects, the chemicals used in the cathode portion are exposed to very extreme conditions [6,20]. It is common for PEMFC efficiency and durability to decline when all these negative effects come together and to be seen as an important obstacle to the widespread use of fuel cells.

In order to eliminate all these negativities, the amount of Pt loaded on the catalyst layer is much higher in the cathode part than in the anode part. When it comes to PEMFC performance to be more efficient, it is very important that the surfaces of Pt metals attached to the MEA surface are electrochemically active and large [92,96].

Carbon black supported Pt NPs are already widely used in the market as PEMFC cathode region catalyst. However, due to their high aspect ratio, these Pt NPs have a very active surface area and are more vulnerable to agglomeration and leaking on the carbon support during fuel cell performance (Figure 1.14) [92]. This situation directly results in the decrease in the electrochemical active surface area (ECSA) of Pt nanocatalysts and naturally impairs the efficiency of the fuel cell.

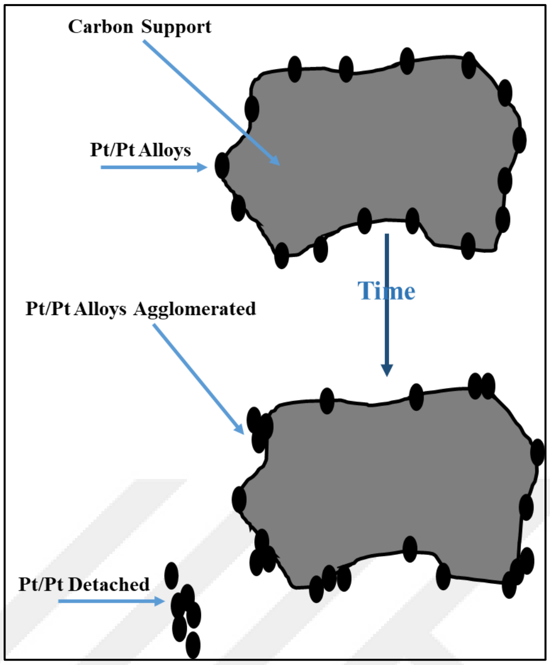

Figure 1.14: Nanocatalyst degradation process on carbon support.

Three main reasons that cause performance decrease in PEMFCs due to MEA degradation are membrane degradation, chemical contamination and catalyst degradation [100]. A decrease in conductivity will occur as problems arise in the transmission of protons from anode to cathode due to membrane degradation. Moreover, H_2 crossover also produces H_2O_2 during the reaction with O_2, leading in the degradation of both the catalyst and the membrane portion. Also, this reaction is exothermic and the heat released can play an extra role in the breakdown of the polymer-based membrane [96,97].

The formation of pollutant by-products such as CO and SO_x during hydrogen production causes the catalyst to be poisoned, and causes a decrease in kinetics, ohmic and mass transfer, which affects fuel cell performance negatively. These types of impurities both damage the structure of the catalyst and accelerate carbon corrosion, causing serious performance decreases. The deteriorating catalyst structure can cause Pt nanocatalysts to sinter, detach, and displace on the carbon support [92,96].

The above-mentioned degradation mechanism can be explained in three steps. First, metal NPs migrate through the carbon support and clump together, namely agglomerates. Secondly, these agglomerated metal structures undergo an electrochemical re-deposition process called the electrochemical Ostwald ripening. Finally, the electrochemical oxidation reaction that causes carbon corrosion occurs on the carbon support. To minimize and if possible eliminate all these negative side effects, the catalysts and support materials used in PEMFC should be reinterpreted with innovative approaches [92,101].

1.2.3. Catalyst in PEM Fuel Cell

Electrochemical catalysts play a major role in the production of electrochemical reactions in a much shorter and more efficient manner by reducing the activation energy of electrochemical reactions in order to ensure that existing electrochemical devices can operate at high performance and produce electrochemical devices with high efficiency. Platinum, palladium, ruthenium and platinum-based transition metal alloys are frequently preferred electrocatalysts in electrochemical devices such as fuel cell, electrolyzers, electrochemical pumps, electrochemical inerters, electrochemical dehumidification, etc. [10].

In the working mechanism of PEMFCs, catalysts are needed for ORR and HOR reactions to occur efficiently and quickly. The electrocatalysts are used in pure form or in supported forms. However, the active surface areas of electrocatalysts used in pure form are lower than the supported catalysts and deteriorate in shorter periods during fuel cell performance and thus affecting the test performance, negatively.

It is expected that the catalysts preferred for PEM fuel cell will have certain properties such as activity, selectivity, stability and poisining resistance. Perhaps the most important of these properties is that the catalyst should be optimally active enough to activate electrochemical reactions, but at the same time not adversely affect other important factors such as reactants and products. Selectivity is another important feature sought in PEMFC catalysts. Thanks to this feature, the desired product can be obtained with high efficiency by eliminating by-products and intermediate products as much as possible. In addition to all these two features, an ideal PEMFC catalyst must be stable for long periods under harsh fuel cell test conditions (operating temperature, reactive chemicals, high voltage, acidic environment etc.) and must be able to withstand contamination from the fuel itself throughout the test [102].

Since it contains these four properties, Pt metal stands at a very important point as a PEM fuel cell catalyst. Thus, Pt is the most ideal noble metal for both H-bonding at the anode side and oxygen bonding at the cathode side, showing the highest activity compared to noble metals such as Rh, Re and Au [102,103].

In addition to high activity, Pt catalysts are also particular importance for PEM fuel cell in terms of selectivity. Oxygen reduction and adsorption without creating by-products such as hydrogen peroxide (H_2O_2) in the ORR reaction that takes place at the cathode, which is one of the most challenging factors in the popularization and cost reduction of PEM fuel cells, is carried out with Pt catalysts (Figure 1.15). In the adsorption process, the affinity for oxygen and the oxygen intermediates of Pt catalyst arises from the position of Pt in the d band with regard to the level of Fermi [103].

Together with their activity and selectivity, Pt catalysts exhibit remarkable performance in terms of stability under PEM fuel cell operating conditions and poisoning resistance against fuel-borne pollutants. It has taken place in the literature that the Pt (111) has the highest stability and substantially reduced poisoning rate, among other Pt structure options [104,105].

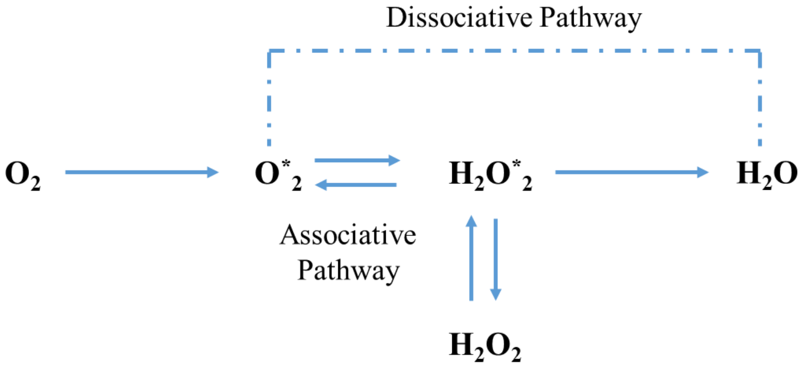

Figure 1.15: Representation figure of dissociative and associative pathway for O_2 in ORR mechanism.

Apart from Pt, also known as platinum group metals (PGMs) and consisting of Ru, Rh, Pd, Os, Ir are also used as electrocatalysts. When looking at the electromotive force (emf) which defined as the voltage produced by an electrical source values of these metals

(Table 1.1), it is understood that especially Pt and Pd elements are very active [106][107]. In addition to being highly active, Pt and Pd elements have very high hydrogen absorption capability, and due to these properties, they are very suitable catalysts for hydrogenation. Furthermore, platinum group metals are more resistant to corrosion than other metals and are more likely to stay inert in reactions where they are used as catalysts [107].

Table 1.1: Atomic numbers and emf values of platinum group metals (PGMs).

Metal Propertiy	**Pt**	**Pd**	**Rh**	**Ru**	**Os**	**Ir**
Atomic Number	78	46	45	44	76	77
Efm (M/M^{+2}) (vs. NHE)	9.85	9.90	4.33	6.80	8.12	4.70

Despite all the positive properties mentioned above, Pt metal is an expensive element and may have some stability and activity problems when used as a catalyst in its monometallic state. New types of catalysts such as alloy, heterstructures or core-shells (Figure 1.16) have been developed in liretarur with inert metal additions such as Cu, Ni, Co, Ti, Cr in order to prevent such negativities and improve durability of Pt catalyst [103,104]. In the literature, there are studies carried out to increase the activity and durability of the Pt catalyst with the addition of noble metals such as Pd, Au, Ru and Ag as well as non-noble metal elements.

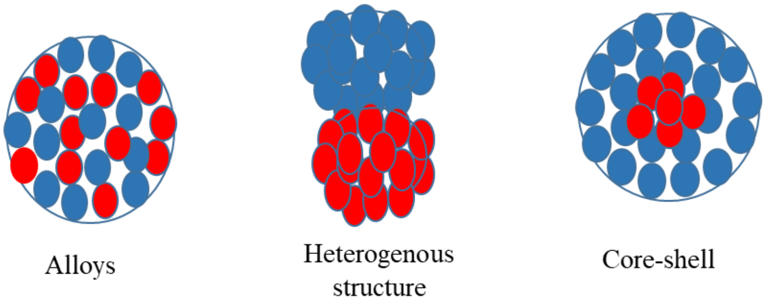

Figure 1.16: Pt-based bimetallic/ trimetallic catalysts: alloys, heterogenous structure and core-shell.

Much more durable electrocatalysts can be developed by manipulating parameters such as size and distribution in the preferred catalysts for PEMFC. The change in geometry and structure of the surface decreased the more oxidizable portion of the alloy and improved electronic factors for further development. By using the dispersion support materials of these expensive platinum-based electrocatalysts, more homogeneous and well dispersed catalysts can profit from both the catalyst loading amount and the cost. Nanoparticles of very small size and homogeneously dispersed on a suitable support material with a high surface area show great activity as a catalyst. This situation is explained by the particle size effect [108–110]. However, when it comes to the acidic environment in the PEM fuel cell, such small nano-structures cannot be efficient as catalysts because they cannot show sufficient oxygen reduction activity in such environments. Beacuse edges and corners are more common in Pt electrocatalysts with small particle size than large ones, and they can react with the reactants in the environment and block the reaction path of oxygen species in this way. This is why it should be optimum for the Pt scale. Recent studies have shown that the optimal size of Pt nanoparticles for better operation should be between 2 and 4 nm [110].

1.2.4. Pt-based Bimetallic Alloys as Electrocatalysts for PEMFC

Due to the kinetic limitations of ORR under standard PEMFC system parameters, the high overpotential loss of ~0.4 V on the cathode, or about 70 % of the total loss, is also a massive issue to the commercial feasibility of PEMFCs [111]. The development of Pt-based catalysts appears to be an elegant alternative to these issues and has attracted a great deal of attention as a way of achieving high efficiency and substantially reducing PEMFC costs [112]. Therefore, detailed studies on the production of Pt-based electrocatalysts have been carried out. The beginning of these studies goes back to the development of a series of Pt-alloy catalysts (Pt-V, Pt-Co-Cr, Pt-Ir-Cr, Pt-Rh-Fe, etc.) by United Technologies Corporation (UTC) in the 1980s that can be used as ORR catalysts for phosphoric acid fuel cells (PAFCs) [113].

The ORR behavior relies greatly on the electrode-electrolyte interface structure. Hence, detailed awareness of the interface structure is necessary in order to create effective catalysts [114]. Considering the acidic operating conditions of PEMFCs, many studies have shown that Pt-based catalysts are active and stable under these conditions compared to commercial Pt/C catalysts.

Changing the geometrical configuration and/or the electronic structure of the Pt surface atoms are often the preferred approach in order to minimize the Pt loading while increasing the ORR activity. By alloying Pt with other metals, this aims could be accomplished. This has been extensively observed in Pt-based metal transition alloys. Due to the nature of alloy structures, a variety of transition metals alloyed with Pt appeared in varying activities [113]. Pt-alloying with non-noble metals such as Ni, Co, Cu, Fe not only decreases Pt loading for PEMFCs, but also helps improving the catalytic activity. In the early 1990s, Murkenjee and at. all reported early studies on the utilization of Pt alloys as ORR catalysts for PEMFCs [115,116]. At high temperatures (900 °C) and under an inert atmosphere, they developed a series of Pt alloys, including Pt-Ni, Pt-Co, Pt-Cr, Pt-Mn, and Pt-Fe. According to this study, it was determined that the Pt (75): M (25) composition was the most effective catalyst based on crystallographic considerations. In the late 1990s, Johnson Matthey also completed notable studies on binary alloys such as Pt-Fe, Pt-Mn, Pt-Ni, Pt-Cr, Pt-Cu, and Pt-Ti. To enhance performance for fuel cell, Pt alloys with a 50:50 Pt:M ratio were heat-treated at different temperatures. It was noticed that if Pt-Ti, Pt-Mn, and Pt-Fe were used as the catalysts (20 wt % Pt alloy on Vulcan carbon), a 20–40 mV efficiency improvement could be achieved [117].

In order to explain the electrochemical activities of Pt-alloy catalysts, it is essential to clarify the kinetic mechanism. One of the accepted explanations in the literature is that dissolution or leaching of the more readily oxidizable base metals in bulk alloys has caused the surface roughening of the Pt alloy to be observed [118]. Through an increase in surface area, this dissolution or leaching of transition metal may lead to greater activity. The low-index crystal planes of Pt have also been observed to display higher ORR reactivity than the high-index crystal planes [110]. On the other hand, the structural effect, the OH_{ads} inhibition effect, and the electronic effect are usually known as the major alloying effects.

Jalan and Taylor claimed that increased ORR activity of Pt alloys may be attributed to the decrease in the inter-atomic distance of Pt-Pt. They suggested that more suitable sites for dissociative oxygen adsorption would be given by smaller Pt-Pt bond distances. The lattice contraction alloys are more effective than Pt, but much less active are those with lattice expansion. A series of Pt alloys were investigated by Min *et al.* and an association between the nearest neighbour distance of Pt-Pt and the particular ORR behavior was established [119]. According to this study, a dozen Pt alloys (Pt_3Ni_{11}, Pt_3Cu_9, Pt_3Co_{11} and so on), show greater specific behaviors than Pt alone since these alloys have smaller Pt-Pt neighbour distances. They also observed that the Pt-Pt nearest-neighbour distance of the synthesized alloys was defined by the heat-treatment temperature [120].

In PEMFCs, most species of surface oxygen (surface hydroxide or oxide) are known to be poisoning species instead of intermediates and the reaction rate is regulated by the concentration of unpoisoned sites [121]. Thus, surface adsorbed OH on Pt may be an intermediate as well as a poisoning species in ORR. It was found that Pt alloys were capable of preventing the formation of OH_{ads} on Pt and thus increase the catalytic activity of ORR. Mukerjee *et al*. found that for certain Pt alloys (PtCr/C, PtMn/C, PtFe/C, PtCo/C,and PtNi/C), the onset potential of OH, which was considered to normally occur above 0.8 V on Pt/C, shifted to more positive potentials [115].

Consequently, bimetallic NPs can be categorised into three major groups depending on the mixing pattern; core–shell structures, heterostructures, and intermetallic or alloyed structures. Bimetallic alloy NPs are very important nanomaterials among all bimetallic NPs, because of their applications in various catalytic reactions such as catalytic reforming reactions, pollution control, and oxidation of alcohol. A significant approach to designing the electronic and geometric structures of NPs to boost their catalytic activity and selectivity is the addition of a second metal. In certain cases that mentioned above, due to strong synergy effect between the metals, bimetallic alloy NPs have higher catalytic efficiencies than their monometallic equivalents. Thanks to their synergistic effect, particular physical and chemical properties of bimetallic alloys are greatly enhanced.

1.2.5. Carbon Support Materials

As mentioned in previous sections, one of the most important obstacles to the spread of PEM fuel cells is the expensive nature of the MEA structure. At this point, the preferred support material is very critical to reduce the Pt loading amount in the expensive catalyst layer in the MEA structure, to improve the catalyst distribution and to increase the mass transfer on the electrode. Carbon support materials greatly affect size, shape and distribution of PEM fuel cell electrocatalysts, not only in catalyst performance and preparation, but also in the transmission of electrons generated during electrochemical reactions and in the difussion of gases [122–124].

Carbon supports with large surface area, optimum porosity for gas flow, high conductivity, contributing positively to catalytic activity and resistant to corrosion are preferred in PEM fuel cells. At this point, the use of appropriate carbon support material especially during the oxygen reduction reaction (ORR) occurring in the cathode part is very critical, as the reaction takes place in the range where the carbon is oxidized. Oxidation of carbon during the fuel cell test causes the interaction between carbon and catalyst to weaken and catalysts to migrate through the support. This situation adversely affects the catalyst performance and causes a shortened catalyst life during testing [125]. Carbon black (CB) is commonly used as a material for PEMFC carbon support. In particular, the Vulcan XC-72 is often used in PEMFCs due to its high surface area and low electrical resistance properties. However, these properties do not make CB an ideal support material for PEM fuel cells. In addition to these advantages, CB has serious disadvantages such as low electrochemical stability and insufficient Pt usage that will affect PEM fuel cell performance dramatically [126].

With the discovery of new types of carbon derived nanostructures in the scientific world, innovative carbon structures have been used in PEMFCs in order to prevent the negativities caused by carbon black. Almost all of these innovative carbon structures are graphene-derived carbon supports. Due to its unique properties, graphene has become a desired material for use in many areas [126]. These unique properties of graphene include its mechanical properties which contributed to it being known as the strongest material ever known, high surface area (2630 m^2/g) and high electrical conductivity [127,128].

Thanks to all these unique properties and the unique structure of defective regions and C = C bonds in its structure, graphene and graphene-derived carbon support materials such as carbon nanotubes (CNTs), graphene nanosheets (GNS), graphene oxide (GO), reduced graphene oxide (RGO) and graphene nanoplateletes (GNPs) are promising structures as they improve the interaction between catalyst and support in synthesizing supported electrocatalysts [129,130].

Among graphene-derived carbon materials, graphene nanoplateletes (GNPs) consists of approximately 10 layers of graphene and distinguishes from other graphene-derived carbon support materials by showing the properties of both single layer graphene and high graphite carbon. For that reason, it has various characteristics; high stability, high surface area, advanced conductivity and high mechanical strength resulting from the single layer graphene structure. In contrast to the potential risk of a thin 2D graphene layer, the graphitic structure helps to prevent inefficient stability. Another advantage comes from the synthesis method of GNP which preserves the graphitic structure of graphite. This structure makes GNP more stable and robust under the conditions of the PEM fuel cell [20,131].

In the literature, many carbon supported Pt-based electrocatalyst studies prepared for PEMFCs with different synthesis methods are available. Details of some of these studies are given below.

Elif Das et al. synthesized GNP-supported bimetallic PtNi, PtFe and PtCu NPs using the supercritical carbon dioxide (scCO2) process [132]. For GNP supported bimetallic PtCu catalysts, Pt (COD)Me_2 and Copper (II) hexafluoroacetylacetonate hydrate [$Cu(hfa)_2.H_2O$] were used as metal precursors. Particle size based on TEM images of the PtCu/GNP catalyst was reported as 4.80 ± 0.70 nm. The ECSA value for the PtCu/GNP catalyst was calculated to be 145 m^2/g. However, according to the ICP-MS results, the fact that the PtCu/GNP catalyst contains 19.6% Pt and 2.5% Cu is a problem due to the expensive nature of platinum. The values achieved indicated that the maximum catalytic activity was shown by the PtNi/GNPs catalyst with with 907.5 mA/cm^2 and 0.54 mW/cm^2.

By modifying the deposition order of the metal precursors and the metal composition, mesoporous carbon aerogel (CA) supported PtCu NPs as electrocatalysts were designed efficiently supercritical carbon dioxide (scCO2) by Barim et. all. [133]. In the sythesis, Pt(cod)Me_2 and Cu(tfa)$_2$ were used as metal precursors. This study investigated the effect of annealing process on the nanoparticle formation at 600 ^{0}C, 800 ^{0}C and 950 ^{0}C under N_2 gas. Mean diameter size of PtCu NPs increased from ~1.8 nm to ~4.5 nm with the increase of the annealing temperature. $Pt_{25}Cu_{75}$/CA that annealed at 800 °C displayed the best ECSA value with 137 m^2/g. However, the $Pt_{25}Cu_{75}$/CA sample annealed at 950 °C sample exhibited higher specific activity (0.165 mA/cm^2). The mass activity of this catalysts (0.102 A/mg_{Pt}) was the same as the commercial Pt/C electrocatalyst. Although the results of the study are promising, the high temperature annealing process to obtain homogeneously dispersed nanoparticles is the inconvenient point of the study.

In 2011, Mani et al. investigated the activities of dealloyed binary PtM_3 (M= Co, Cu, Ni) NPs and trimetallic $PtNi_3M$ (M= Co, Cu, Fe, Cr) as electrocatalysts in PEMFCs. All catalysts were prepared by an impregnation/freeze-drying route followed by annealing. According to the ICP-MS, the bimetallic PtCu catalyst with $Pt_{87}Cu_{13}$ composition had an ECSA value of 72 m^2/g after dealloying. For $Pt_{82}Ni_{15}Cu_3$ composition catalysts, the ECSA value was calculated as 116 m^2/g. Although this study gives detailed information about the electrochemical performance of bimetallic and trimetallic structures, information on particle size is not available. However, the preferred protocol for the synthesis of electrocatalysts is costly as it requires high temperatures and vacuum (10^{-3} Torr) [134].

Alloy PtCu electrocatalysts were synthesized on carbon supports of reduced graphene oxide (rGO), Vulcan XC72 (VC) and hybrid (rGO-VC) with the help of oleylamine, octadecene and morpholine borane as reducing agent and surfactants [135]. The average particle size of polyhedral CuPt NPs was 3.5 ± 0.7 nm. Best NP dispersion and support-metal interaction took place over rGO-VC hybrid support. The ECSA values for $Cu_{45}Pt_{55}$/VC, $Cu_{45}Pt_{55}$/rGO and $Cu_{45}Pt_{55}$/ rGO-VC were 73 m^2/g, 56 m^2/g and 119 m^2/g, respectively. The maximum power density of $Cu_{45}Pt_{55}$/ rGO-VC was calculated as 480 mW cm^{-2}. In these studies, 400 ^{0}C annealing was performed, most likely due to the utilization of strong reducing agents and surfactants in the synthesis process ad further completion of the nanostructure formation.

In 2015, Alessandro H.A. et al. investigated the effect of the reaction conditions on the electrochemical activities of MWCN supported PtCu NPs by thermal reduction, chemical reduction and alloy synthesis methods. The produced catalysts showed a Pt loading of 19.6–19.8 wt.%, with a Pt/Cu atomic ratio of 2.60–2.80. $H_2PtCl_6 \cdot 6H_2O$ and $CuSO_4 \cdot 5H_2O$ were used as metal precursors. The particle size of NPs were found using XRD technique as 6 nm, 9 nm and 2.5 nm for alloy synthesis method, thermal reduction and chemical reduction methods, respectively. The corresponding ECSA values were 41.3 m^2/g, 27.3 m^2/g and 43.8 m^2/g for alloy synthesis method, thermal reduction method and chemical reduction method, respectively. As conclusion, the best activity belongs to the MWCN supported Pt_3Cu catalyst generated by chemical reduction method [136].

In 2015, Chen et al. succeeded in synthesizing star-shaped PtCu electrocatalysts by chemical reduction method using $CuCl_2.2H_2O$ instead of $Cu(acac)_2$ as the Cu precursor for the first time. Oleylamine and oleic acid were used as reducing agents, and $H_2PtCl_6.6H_2O$ was used as the Pt precursor. PtCu NPs were prepared on two different supports; rGO and commercial Vulcan XC-72. When the ECSA values were examined, it was seen that the monometallic Pt/rGO catalyst had a higher value. The ECSA values for Pt/rGO, PtCu/rGO and PtCu/XC-72 are 55,7, 45,3 and 41,8 m^2/g, respectively [137].

Alekseenko et al. showed that de-alloyed PtCu/Vulcan XC-72 catalysts were more stable than commercial Pt/Vulcan XC-72. In this study, carbon supported PtCu nanocatalyst, which has the same Pt ratio as the commercial Pt catalyst, was synthesized in liquid phase with sodium borohydride reducing agent. $CuSO_4.5H_2O$ and H_2PtCl_6 were used as metal precursors. A significant part of the NPs found in this material was characterized by a gradient structure. The ECSA values were calculated as ~96 m^2/g and ~75 m^2/g for grad PtCu and alloy PtCu, respectively. After the stability test, ECSA values reduced by 18%, 25% and 29% for grad PtCu, alloy PtCu and commercial Pt/C, respectively [138].

In another study, dealloy PtCu/CNT NPs were synthesized using $NaBH_4$ as the reducing agent by assisted polyol-reduction using microwave irradiation or conventional heating where synthesis conditions changed the electrochemical activity for these electrocatalysts. Mass and surface specific activities as well as ECSA values of electrocatalysts strongly depended on the synthesis conditions with 4.5 fold activity increase compared with commercial Pt/C [139].

Recently, Garcia-Cardona et al. produced PtCu NPs supported on carbon nanofibers (CNFs), multi-walled carbon nanotubes (MWCNTs) and Vulcan carbon XC-72 by the electroless deposition and galvanic exchange [140]. Characterization studies showed that the crystallite size of PtCu alloy core covered by a Pt-rich shell was 3 nm. Pt(Cu)/CNF and Pt(Cu)/MWCNT gave the highest mass activity and specific activity for the O_2 reduction and both of them were relatively more stable than Pt(Cu)/XC-72. ECSA values of Pt(Cu)/CNF, Pt(Cu)/MWCNT, Pt(Cu)/XC-72, PtCu/C (commercial) and Pt/C (commercial) were 70.10 m^2/g, 44,60 m^2/g, 78.40 m^2/g, 86.40 m^2/g and 73.30 m^2/g, respectively.

Liu et al. produced a range of PtCu NPs with different metal ratios by a modified alkaline-ethylene glycol method that successfully gave colloidal PtCu alloy nanoclusters (NCs) stabilized with acetate ions and ethylene glycol, with small particle size (~2 nm) and tunable Pt/Cu ratio. The preferred support material for PtCu NPs were a melem-modified carbon support (MMC). $Pt_{75}Cu_{25}$/MMC showed the highest electrochemical mass activity (1.59 A.mg^{-1}Pt) and specific activity (3.98 mA.cm^{-2}Pt) at 0.9 V of supported NCs ever reported. The ECSA values of the electrocatalysts were calculated as 35 $m^2\ g^{-1}$, 40 $m^2\ g^{-1}$, 57 $m^2\ g^{-1}$, 26 $m^2\ g^{-1}$, 19 $m^2\ g^{-1}$ for $Pt_{90}Cu_{10}$/MMC, $Pt_{75}Cu_{25}$/MMC, $Pt_{60}Cu_{40}$/MMC, $Pt_{40}Cu_{60}$/MMC and $Pt_{25}Cu_{75}$/MMC, respectively [141].

2. MATERIALS

Platinum (II) acetylacetonate >= 99.98 % trace metals, copper (II) acetylacetonate 97 %, anhydrous tetrahydrofuran (THF), anhydrous pentane (C_5H_{12}), Dimetilformamid (DMF), Nafion™ perfluorinated resin solution 5 wt. % and chloroform were purchased from Sigma Aldrich. Graphene Nanoplatelet (GNP) was purchased from XG Sciences and Carbon Black (CB) were provided from Cabot Corporation. Extra pure argon gas and varigon gas (95% argon+5% H_2) were purchased from Linde. GNP and CB were dried prior to use. Pentane was degassed with freze-pump method. All other chemicals were used without further purification. All reactions were taken place using standard Schlenk tube or Fischer-Porter/balloon flask bottle techniques under an inert and dry atmosphere.

3. STRUCTURAL CHARACTERIZATION

Inductively Coupled Plasma Mass Spectrometer (ICP-MS) measurement was performed by using Agilent 7800 ICP-MS for all synthesized catalysts to obtain total metal loading on the hybrid carbon supports. BET surface area and the total pore volume of the hybrid carbon supports (CB:GNP (50:50), CB:GNP (30:70) and CB:GNP (70:30)) were measured using Micromeritics 3Flex Version 5.00 Surface Area and Pore Size Analyzer. The precursors and the synthesized electrocatalysts were characterized by XRD with RIGAKU Smart Lab. XRD instrument was used with wavelength of irradiation of Cu-Kα was 0.154 nm at 2θ angles from 10 to 80 in GTU. FT-IR analysis used for detection of functional group was performed with Perkin Elmer Spectrum 100. Determination of carbon supports and precursors' decomposition temperatures were measured using a Mettler Toledo thermal analysis system TGA / SDTA 851 22.JPEG in a temperature range of 25-900 ^{0}C and with a heating rate of 10 ^{0}C/min under nitrogen gas. The dispersion and composition of the catalysts were observed by FEI (PHILIPS) XL30 SFEG scanning electron microscope (SEM). The homogeneity and particle size of the bimetallic and monometallic nanoparticles over the hybrid carbon supports were characterized by Hitachi HighTech HT7700 transmission electron microscope (TEM). The mean sizes of the nanoparticles on the support were calculated by manually counting NPs on the TEM images with Image J free software. The TEM spicements of catalysts were prepared by placing a few drops of colloidal hybrid carbon supported PtCu, Pt and Cu NPs in THF on holey-carbon copper grids. The WITech alpha 300R Raman Spectrometer in DAYTAM was used to achieve the structure characterization and the defect ratio of the carbon supports before and after the reaction. The XPS data were taken by using the Al Kα x-ray source (hv= 1486.6 eV), with a total resolution of approximately 1.0 eV, and the raw data were analyzed using CasaXPS software in order to identify the different components of the overall signals in the spectra of each element.

4. EFFECT of DIFFERENT SYNTHESIS METHODS on the FORMATION of BIMETALLIC PtCu NANOPARTICLES and a COMPRASION of THEIR ELECTROCHEMICAL ACTIVITIES

4.1. Experimental Method

In this part of the thesis, a series of studies were carried out to determine the most effective synthesis method for electrochemically active bimetallic PtCu NPs. Nanoparticles were obtained using two separate synthesis methods, primarily organometallic and thermal decomposition. In addition, by adjusting these synthesis conditions, the optimum values of parameters such as temperature, pressure and time which are very crucial for creating well-defined NPs were attempted to be found. For this purpose, five different bimetallic PtCu NPs were synthesized and CB:GNP (50:50) carbon supports were used as carbon support material, which have been proven to have a synergistic effect and contributed positively to the electrochemical activity in monometalic Pt electrocatalysts [20].

4.1.1. Preparation of Bimetallic PtCu/CB:GNP (50:50) Nanoparticles

4.1.1.1. Impegrantion Method of Metal Precursors on the Hybrid CB:GNP (50:50) Carbon Support

Basically, two different synthesis methods have been chosen to synthesize hybrid carbon supported PtCu/CB:GNP (50:50) NPs. The first of these synthesis methods is the organometallic synthesis and the other is the thermal decomposition method.

In both synthesis methods, incipient wetness impregnation approach was used to decorate metal NPs on the hybrid CB: GNP (50:50) carbon support. This approach is also known as dry impregnation, its basic rationale is to impregnate metal precursors dissolved in the least amount of solvent possible onto a dry support material. At this point, how much liquid the support material can absorb should be calculated in advance. For this, the relevant solvent is slowly dropped onto the support material with known weighing amount and then the support material is mixed thoroughly. Then, the amount of solvent consumed at the point where the support material starts to sludge is calculated and so the amount of solvent that the support material is saturated with solvent is found.

For all synthesized bimetallic PtCu/CB:GNP (50:50) NPs, Pt(acac)$_2$ and Cu(acac)$_2$ (acac: acetylacetonate) were used as metal precursors. For all synthesized hybrid carbon supported PtCu NPs, calculations were made with a theoretical weight of 20% metal loading on the hybrid carbon support.

According to a typical synthesis method; in the glove box, CB and GNP carbon support materials that previously dried under vacuum and 100 ^{0}C during 8 hours, 155.2 mg are weighed and manually mixed well in the mortar. Then, 3 ml of THF (tetrahydrofuran) + 2 ml of chloroform are added to the mixture of 117.9 mg Pt(acac)$_2$ and 78.5 mg Cu(acac)$_2$, which is weighed in a vial in the glove box, and mixed to obtain a homogeneous mixture. After obtaining a homogeneous mixture, this mixture was absorbed 3 times, 100 μL each time, onto the hybrid carbon support in the glove box and then mixed thoroughly to evaporate the solvent. This process was continued until the homogeneous metal precursor mixture was finished. After the impregnation of the metal precursors on the hybrid carbon support was completed, this prepared solid mixture was taken into the Fisher-porter reactor or balloon glass flask to be removed from the glove box and to proceed to the next step that is reduction of metal precursors to obtain bimetallic PtCu NPs. These samples taken out of the glove box in the Fisher-porter and balloon flask were kept under vacuum for approximately 5 hours to remove the THF and chloroform before reduction process. Such organic solvents remaining in the environment can cause undesirable reactions during the reduction process and can reduce catalytic activity by binding on both the support material and the NPs.

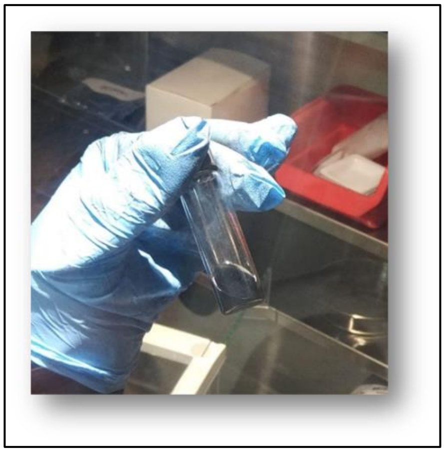

Figure 4.1: Homogeneous mixture of Pt (acac)$_2$ and Cu (acac)$_2$ prepared in glove box and ready to be impregnated on hybrid carbon support CB:GNP (50:50).

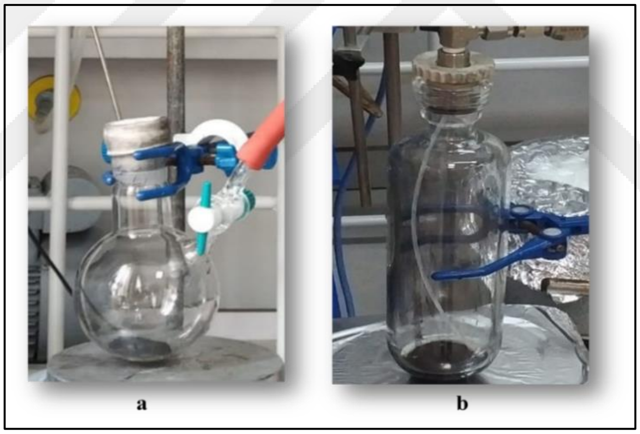

Figure 4.2: Metal precursor mixture impregnated on hybrid carbon support, prepared in glove box and then put into (a) balloon flask and (b) fisher-porter reactor for reduction of metal precursors at the outside of glove box.

4.1.1.2. Synthesis of CB:GNP (50:50) Supported Bimetallic PtCu Electrocataysts

Before starting the synthesis of five different nanomaterials in this section, TGA analysis was performed to understand whether the carbon support materials (CB and GNP) and metal precursors (Pt (acac)$_2$ and Cu (acac)$_2$) used in the synthesis procedure decomposed at 300 ^{0}C as the maximum temperature to be reached during synthesis. The TGA analysis for both carbon supports and metal precursors was done up to 900 ^{0}C. TGA result for carbon supports is presented in Figure 4.3 and for metal precursors in Figure 4.3. According to the TGA result, it was recognized the carbon black (CB) did not lose any weight at 900 ^{0}C, while GNP lost 12 % by weight at the end of 900 ^{0}C. However, both carbon supports remain stable without degradation at 300 ^{0}C which is the maximum reaction temperature. As a result of the TGA presented for carbon black, the weight increase of approximately 3% up to 300 ^{0}C may be due to a setback of the device at that time.

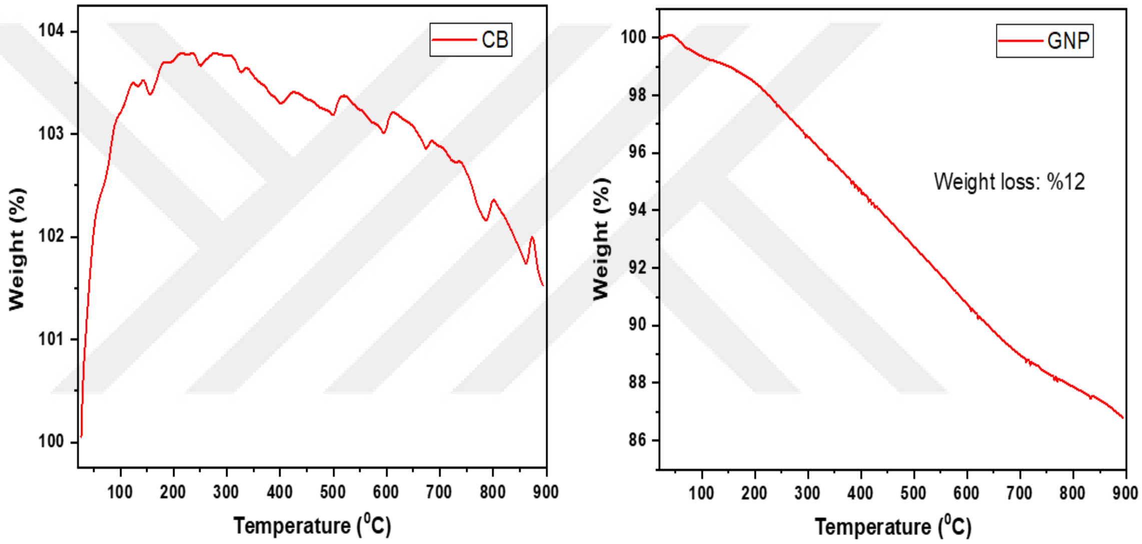

Figure 4.3: TGA result for CB and GNP carbon supports.

According to the TGA analysis performed for metal precursors, it is seen that there is a decrease of 72 % and 94 % by weight for Pt(acac)$_2$ and Cu (acac)$_2$, respectively (Figure 4.4). When the results are examined, it seems to be that the loss of weight ends at approximately 250 ^{0}C and after this point it draws a stable line up to 900 ^{0}C. This weight loss at 250 ^{0}C indicates that there is a loss for the metal Pt and Cu together with the organic structures in metal precursors and may create a challenge especially for the thermal decomposition reaction that will take place at 300 ^{0}C. Nevertheless, the synergetic effect of Pt and Cu elements, which are bimetallic in the electrocatalyst structure, can inhibit this negative situation and can show an effective electrochemical activity despite the weight loss.

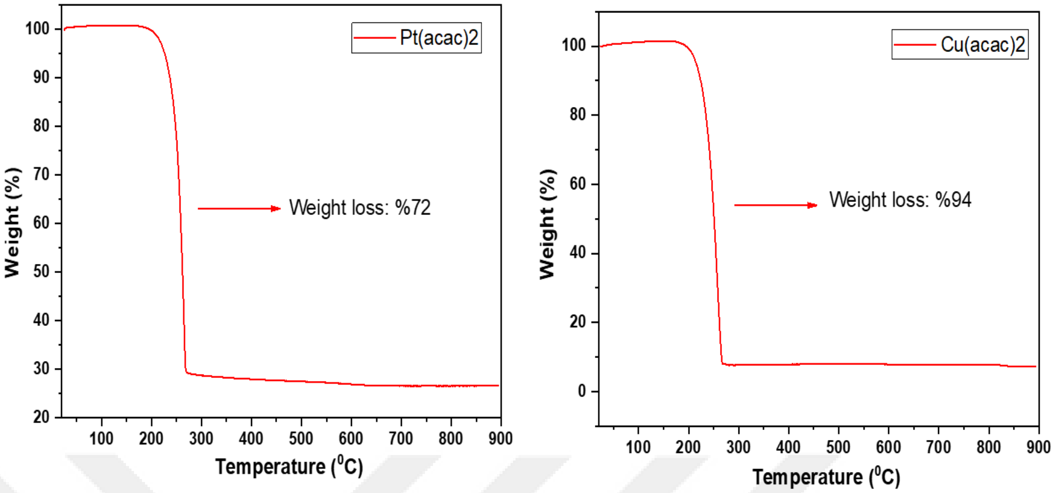

Figure 4.4: TGA result for Pt (acac)$_2$ and Cu (acac)$_2$ metal precursors.

As mentioned before, two different synthesis methods, organometallic synthesis and thermal decomposition, were used to produce bimetallic PtCu NPs. Images showing the experimental equipment of these two synthesis methods are given in Figure 4.5 and Figure 4.6 for thermal reduction and organometallic synthesis, respectively. By using these two synthesis methods, five different PtCu Nps were synthesized at various reaction temperatures and times. The codes of these five distinct bimetallic PtCu/CB: GNP (50:50) NPs are respectively; PtCu (120-2h), PtCu (300-1h), PtCu (300-4h), PtCu (300-1h/70-24h) and PtCu (70-24h) and the details are as follows:

- **PtCu (120-2h):** Based on the organometallic synthesis method, it was obtained as a result of reduction reaction which took place under 3 bar H_2 gas at 120 ^{0}C for 2 hours by using Fisher-porter reactor.
- **PtCu (300-1h):** Based on the thermal decomposition method, it was obtained as a result of reduction reaction which took plece under dynamic varigon gas (mixture of 95 % Argon gas and 5 % H_2 gas) gas at 300 ^{0}C for 1 hour by using balloon flask.
- **PtCu (300-4h):** Based on the thermal decomposition method, it was obtained as a result of reduction reaction which took place under dynamic varigon gas (mixture of 95 % Argon gas and 5 % H_2 gas) gas at 300 ^{0}C for 4 hours by using balloon flask.
- **PtCu (300-1h/70-24h):** Based on the organometallic synthesis method and with using hybrid GB:GNP (50:50) carbon support material. This support material was calcined

under dynamic varigon gas at 300 ^{0}C for 1 hour in the tube furnace before the metal precursor mixture is impregnated onto these hybrid carbon support in the glove box. It was obtained as a result of reduction reaction which took place under 3 bar H_2 gas at 70 ^{0}C for 24 hours by using Fisher-porter reactor.

- **PtCu (70-24h):** Based on the organometallic synthesis method, it was obtained as a result of reduction reaction which took place under 3 bar H_2 gas at 70 ^{0}C for 24 hours by using Fisher-porter reactor.

Table 4.1: A table representation of synthesis methods and synthesis conditions of bimetallic PtCu/CB:GNP (50:50) NPs.

Sample Code	**Synthesis Method**	**Temperature (^{0}C)**	**Gas**	**Time (hour)**	**Support Calcination Process**	**Fisher-Porter/Balloon Flask**
PtCu (120-2 h)	Organometallic	120	3 bar H_2	2	No	Fisher-porter
PtCu (300-1 h)	Thermal Decomposition	300	Dynamic varigon gas	1	No	Balloon flask
PtCu (300-4 h)	Thermal Decomposition	300	Dynamic varigon gas	4	No	Balloon flask
PtCu (300-1h/70-24 h)	Organometallic	70	3 bar H_2	24	Yes (under dynamic varigon gas, 1 hour, 300 ^{0}C)	Fisher-porter
PtCu (70-24 h)	Organometallic	70	3 bar H_2	24	No	Fisher-porter

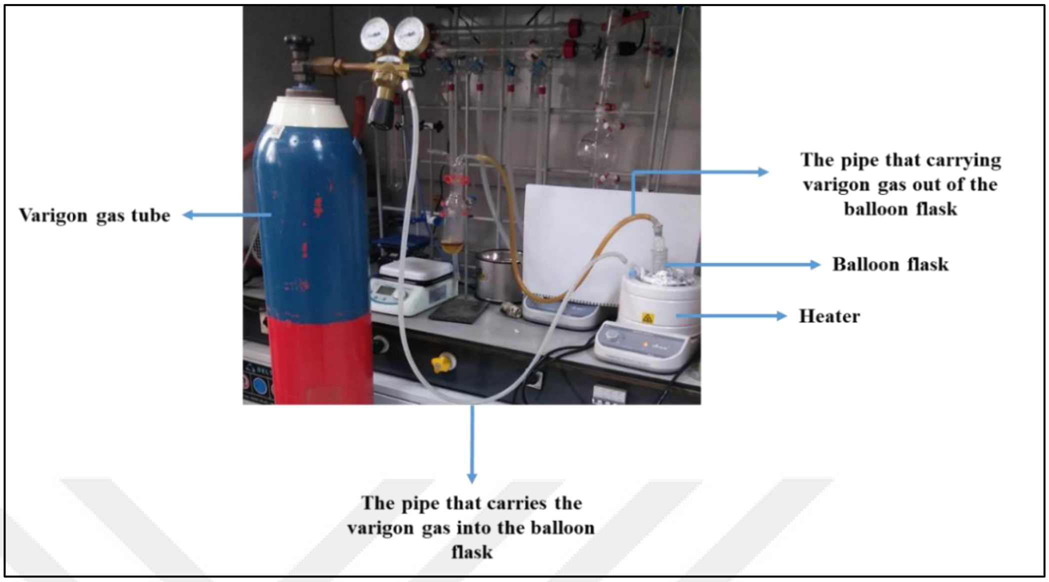

Figure 4.5: Visual showing the synthesis equipment of synthesized PtCu (300-1h) and PtCu (300-4h) catalysts using the thermal decomposition method and dynamic varigon gas.

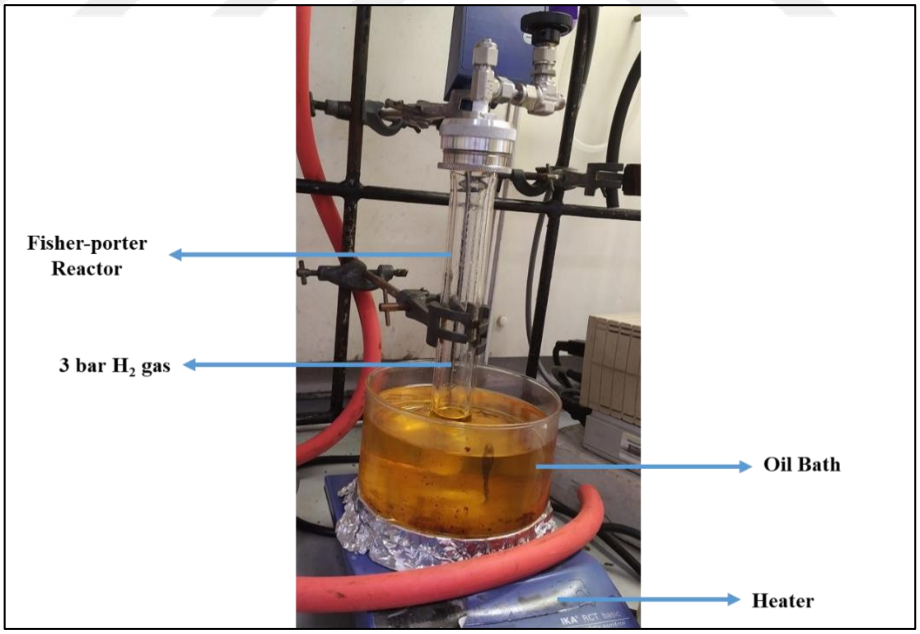

Figure 4.6: Visual showing the synthesis equipment of synthesized PtCu (120-2h), PtCu (300-1h/70-24h) and PtCu (70-24h) catalysts using the organometallic method and 3 bar H_2 gas.

Both synthesis methods performed were environmentally friendly since no harmful chemical reducing agent was used. For organometallic synthesis, H_2 gas, which is a very abundant and clean source in nature, was preferred as a reducing agent and the reaction temperature was kept as mild as possible. In thermal decomposition reduction process, bimetallic PtCu NPs were tried to be obtained with the help of temperature and varigon gas.

After the reaction time for the reduction process was completed, all catalysts were washed with pentane (5 x 40 mL) under an argon atmosphere to remove organic structures that may form on their surfaces and then they was left to dry under vacuum overnight. The preferred pentane for this process is anhydrous pentane, which is deoxygenated by freeze-thaw process. After washing with pentane, a part of the pentane waste belonging to each catalyst is taken into a glass vial and its visual is presented in Figure 4.7. This visual in Figure 4.7 reveals a striking detail. Although a yellowish color is seen in the pentane waste of PtCu/CB:GNP (50:50) electrocatalysts synthesized by the organometallic synthesis method (PtCu (120-2h), PtCu (300-1h/70-24h) and PtCu (70-24h), this is not the case for PtCu (300-1h) and PtCu (300-4h) samples synthesized by thermal decomposition. It may be a signal that the organic (acac) structure in the metal precursors is moving away during reduction process in the samples synthesized by thermal decomposition. In contrast to this, it should be noted that in the samples (PtCu (120-2h), PtCu (300-1h/70-24h) and PtCu (70-24h) synthesized by the organometalic synthesis method, although they were washed with pentane, the organic structure may still have attached to carbon support material and/or NPs. This can adversely affect the electrochemical activities of these catalysts and cause undesirable reactions during the electrochemical process.

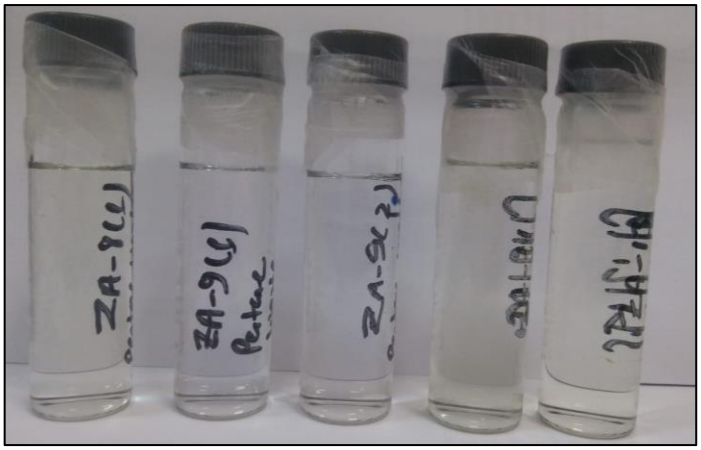

Figure 4.7: Pentane waste from each catalyst after washing with pentane; PtCu (120-2h), PtCu (300-1h), PtCu (300-4h), PtCu (300-1h/70-24h) and PtCu (70-24h) from left to right, respectively.

As stated before, the metal amount in these synthesized catalysts was calculated as 20 % theoretically and based on this calculation, metal loading was made on the hybrid CB:GNP (50:50) carbon support. The data obtained according to the ICP-MS analysis aregiven in Table 4.2.

Table 4.2: ICP-MS results of synthesized electrocatalysts.

Sample Code	% weight of Pt	% weight of Cu
PtCu (120-2h)	8.99	3.77
PtCu (300-1h)	8.50	2.61
PtCu (300-4h)	12.70	4.14
PtCu (300-1h/70-24h)	8.10	3.95
PtCu (70-24h)	9.98	3.82

4.2. Results and Discussion

4.2.1. FT-IR Analysis

FT-IR analysis is a very useful technique used to detect various functional groups in the structure of the substance, and it gives very important clues about the chemical composition of the sample. As mentioned in the previous sections, the yellowish color formed in the pentane wastes of (PtCu (120-2h), PtCu (300-1h/70-24h) and PtCu (70-24h) samples synthesized by organometalic method was read as a sign of the presence of some undesirable structures originating from the (acac) organic group in the metal precursors despite washing with pentane in many times. FT-IR analysis was performed for all synthesized catalysts; PtCu (120-2h), PtCu (300-1h), PtCu (300-4h), PtCu (300-1h/40-24h) and PtCu (70-24h) to clarify this situation and to identify if there are undesirable organic structures.

Before FT-IR analysis of the produced supported PtCu NPs, a separate FT-IR analysis was performed to detect the signals coming from the carbon supports in the catalyst structure (Figure 4.8 and Figure 4.9).

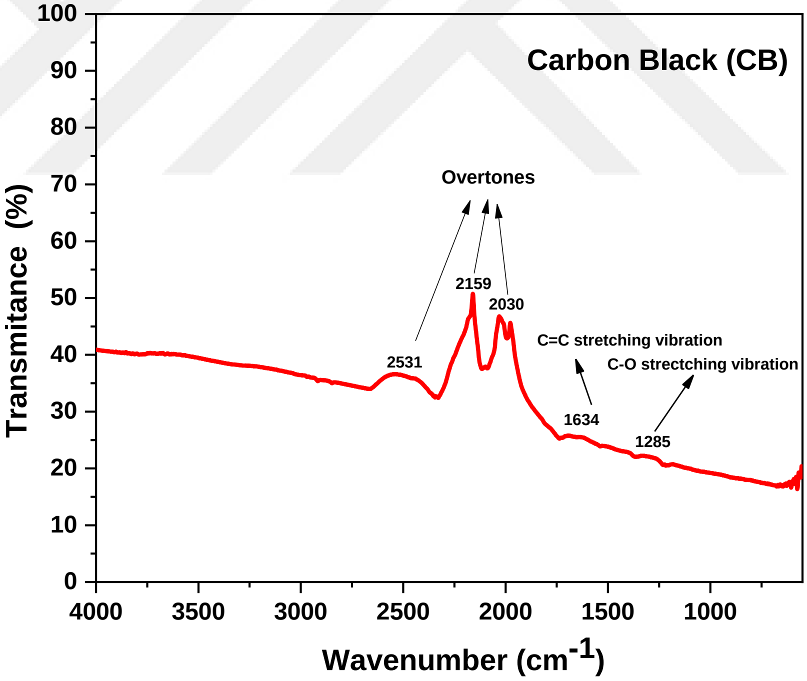

Figure 4.8: FT-IR analysis result for CB.

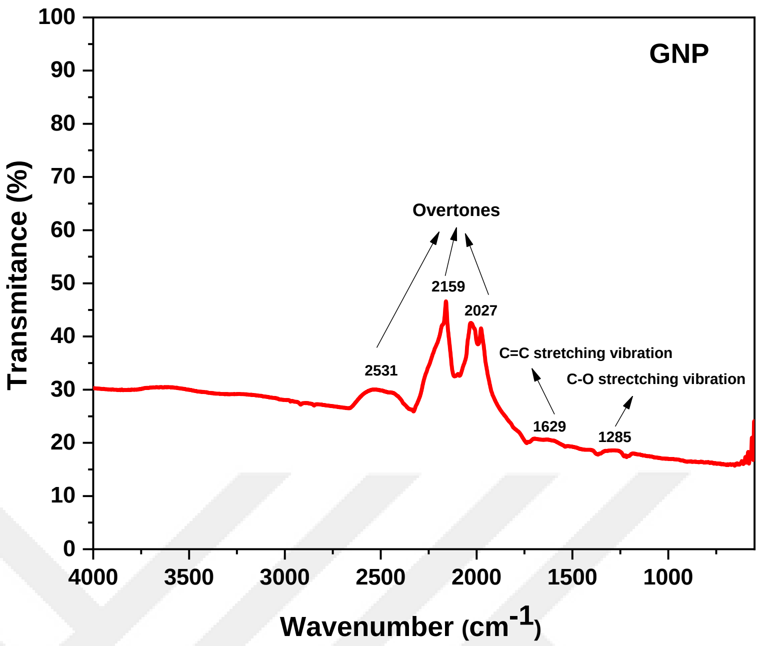

Figure 4.9: FT-IR analysis result for GNP.

Although the results are given as transmitance, the reason that the position of the peaks for both CB and GNP is upward is due to the low IR transmitance of CB and GNP and the device perceives this as absorption of IR.

When the FT-IR peaks of both supports are examined, it is seen that both of them give similar peaks at almost similar positions. C=C stretching band with very small intensity, which occurs at the 1634 cm^{-1} and 1629 cm^{-1} for CB and GNP, respectively. The C-O strectching vibration band at the same point at 1285 cm^{-1} for both carbon supports. This C-O functional group in the carbon support structure makes the carbon support surface partially negative, thus it promotes stronger interaction between the positively charged metal NPs and the carbon support. A broad peak at 2531 cm^{-1} is also observed in the FT-IR spectra for both carbon materials. Although this peak is similar to the O-H functional group in the water, the position of this symmetric and asymmetric OH stretching vibrations band for water is maximum 3656 and 3755 cm $^{-1}$ in the literature. When the spectra of other samples taken with the FT-IR device were examined, it was understood the peaks at 2531 and 2037-1971 cm^{-1} were caused by the device. Thus, these peaks are called as overtones. The fact that no functional groups belonging to water were detected in the FT-IR spectra is an indication to carbon supports were dried well under vacuum before synthesis process.

In addition to carbon supports, FT-IR analysis was performed for both precursors; Pt(acac)$_2$ and Cu(acac)$_2$ and given in Figure 4.10 and 4.11, respectively.

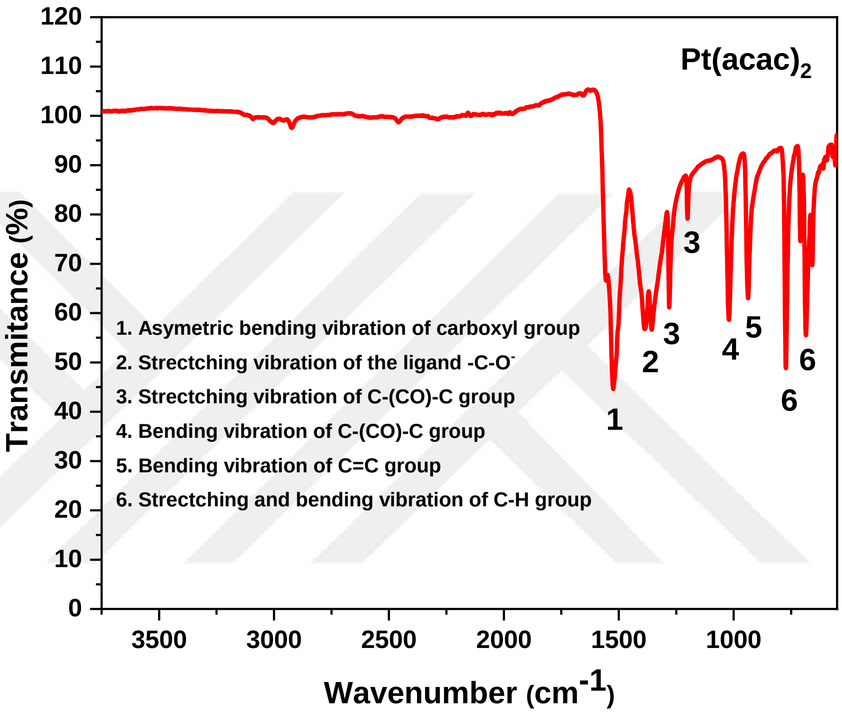

Figure 4.10: FT-IR analysis result for Pt (acac)$_2$.

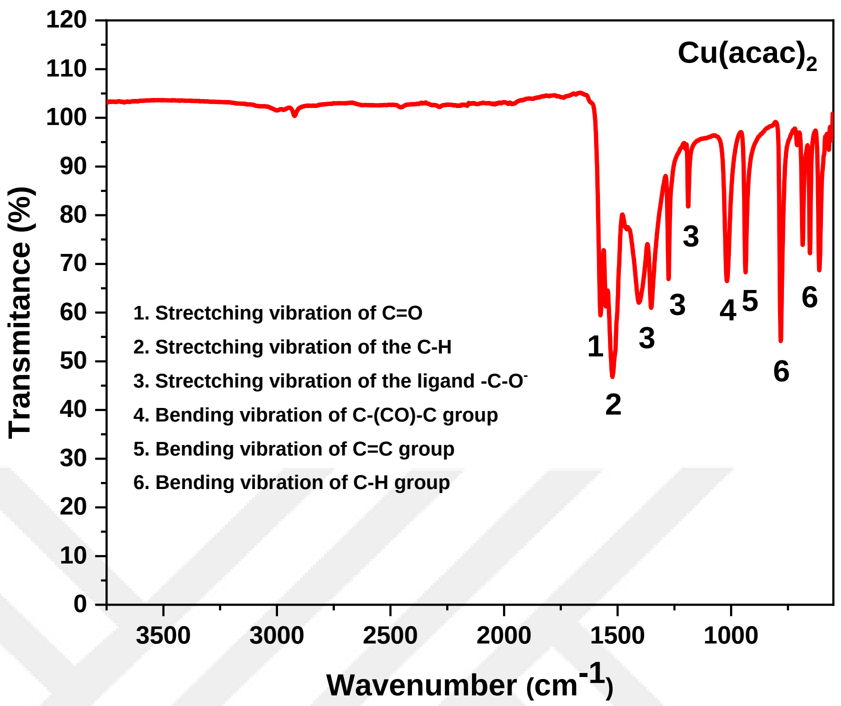

Figure 4.11: FT-IR analysis result for Cu (acac)$_2$.

When the FT-IR spectrum taken for the Pt(acac)$_2$ metal complex was examined, specifically six different functional groups were identified. At 1521, 1387, 1356-1201, 1019, 940 and 772-683 cm^{-1} peaks are belong to asymetric bending vibration of carboxyl group, stretching vibration of the ligand -C-O$^-$, strectching vibration of C-(CO)-C group, bending vibration of C-(CO)-C group, bending vibration of C=C group and strectching and bending vibration of C-H group, respectively. Similar to the Pt(acac)$_2$, peaks belonging to six different functional groups were detected in the Cu(acac)$_2$. At 1572, 1517, 1400-1350-1274-1187, 1018, 937 and 780-652 peaks refer to stretching vibration of C=O, bending vibration of C-H, stretching vibration of C-(CO)-C group, bending vibration of C-(CO)-C, bending vibration of C=C and bending vibration of C-H group, respectively [142]. The explanation of the similar functional groups in these two complexes are noticeable at relatively different points is that their metals are different from each other. FT-IR spectrum of (PtCu (120-2h), PtCu (300-1h/70-24h) and PtCu (70-24h) catalysts prepared according to the organometallic synthesis method is given in Figure 4.12.

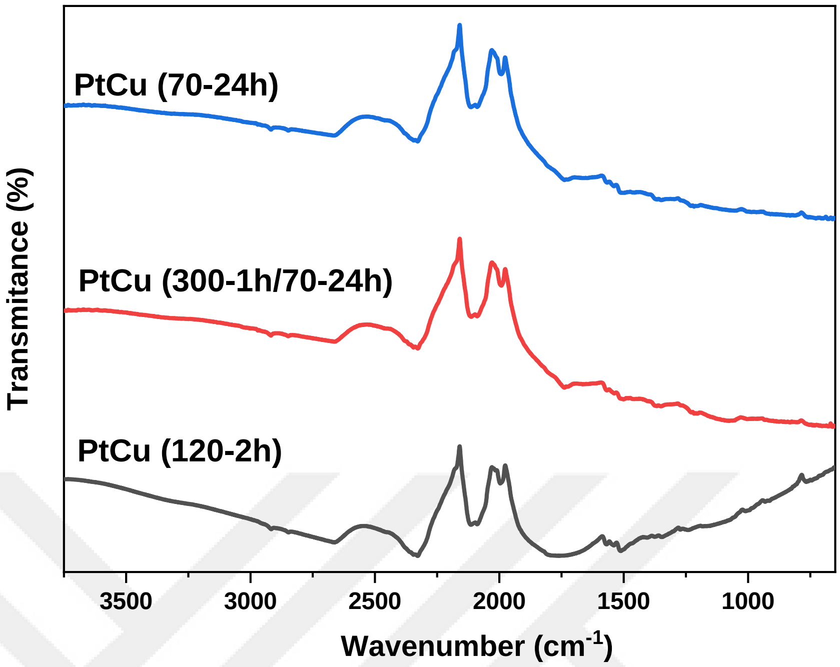

Figure 4.12: FT-IR spectra of (PtCu (120-2h), PtCu (300-1h/70-24h) and PtCu (70-24h) electrocatalysts synthesized by organometallic synthesis method.

Contrary to the organometallic synthesis method, no peak between at 1590 - 700 cm^{-1} was observed in the FT-IR spectrum of PtCu (300-1h) and PtCu (300-4h) catalysts synthesized by thermal decomposition method (Figure 4.13).

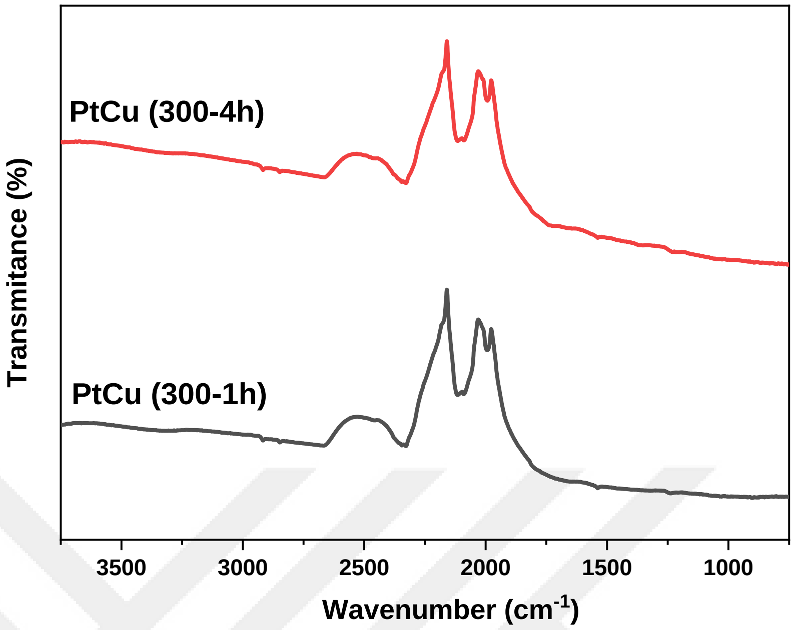

Figure 4.13: FT-IR spectra of PtCu (300-1h) and PtCu (300-4h) electrocatalysts synthesized by thermal decomposition method.

These FT-IR results explain the yellowish color of the pentane residue in catalysts (PtCu (120-2h), PtCu (300-1h/70-24h) and PtCu (70-24h) after pentane washing. Based on these results, it is recognize that catalysts (PtCu (120-2h), PtCu (300-1h/70-24h) and PtCu (70-24h) catalysts may contain undesirable organic structures. The failure to successfully remove undesirable organic structures and metal complexes from the catalyst structure causes undesirable reactions, especially during electrochemical process, and the catalyst is unable to function effectively.

4.2.2. TEM Analysis

One of the most important aspects affecting the catalytic activity of a catalyst is the presence of active sites on its surface. In addition, it is crucial to understand how the synthesis conditions affect the morphology, dispersion and the surface properties of the produced NPs. Theoretically, as the size of the nanostructure decreases, the active surface area increases and the catalytic activity will be thus positively affected. The TEM image and particle size histogram of PtCu (120-2h) and PtCu (300-1h/70-24h) electrocatalysts synthesized according to the organometallic synthesis are given in Figure 4.14.

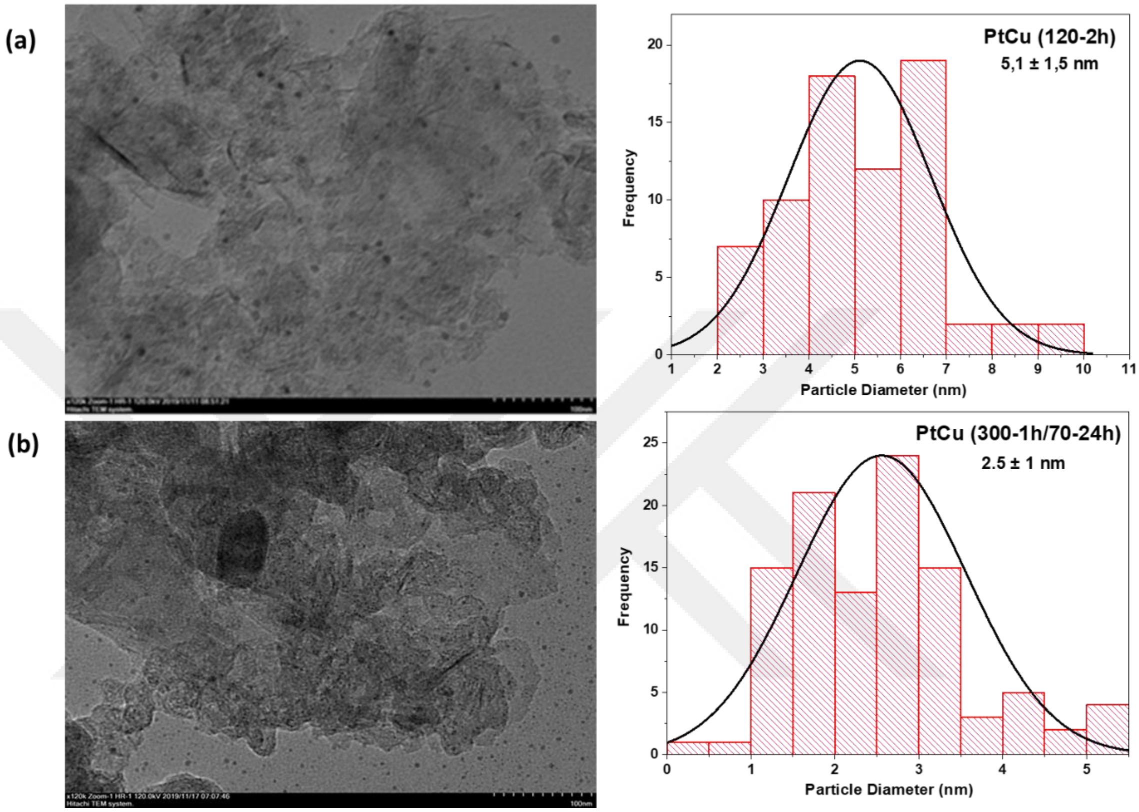

Figure 4.14: TEM image and particle size histogram of (a) PtCu (120-2h) and (b) PtCu (300-1h/70-24h); PtCu / CB:GNP (50:50) electrocatalysts synthesized by organometallic synthesis method (ruler: 100 nm).

TEM images tevealed that spherical and well-defined PtCu NPs with mean size diameters of 5.1 ± 1.5 nm and 2.5 ± 1.0 nm for PtCu (120-2h) and PtCu (300-1h/70-24h) were achieved, respectively. Although both catalysts were synthesized with the organometallic synthesis method, the particle size of the PtCu (120-2h) synthesized at 120 ^{0}C for 2 hours under 3 bar H_2 gas was larger than PtCu (300-1h/70-24h) which was produced at 70 ^{0}C for 24 hours under 3 bar H_2. At high temperatures, it is well known that NPs tend to nucleate faster and this may cause the particles formed to grow in size [30]. At this point, it should be kept in mind the CB and GNP carbon supports used for the PtCu (300-1h/70-24h) catalyst were calcined under dynamic varigon gas for 1 hour at 300 ^{0}C prior to synthesis process and this fact may have caused the particle size to be smaller for the PtCu (300-1h/70-24h) catalyst.

Although PtCu (120-2h) and PtCu (300-1h/70-24) are monodisperse and well-defined spherical MNPs, TEM images show that some NPs are held on the carbon surface of the copper TEM grid rather than on the hybrid CB:GNP (50:50) carbon support. This fact may be due to lack of a strong interaction between the NPs and the hybrid carbon support.

The TEM image of PtCu (70-24h) synthesized at 70 ^{0}C under 3 bar H_2 for 24 hours is presented in Figure 4.15. Interestingly, when the TEM images were examined, no NPs formed on the hybrid carbon support was observed. However, there is also no agglomerated image of any metal complexes that might belong to the metal precursors in the TEM image despite the fact that according to the ICP-MS results given earlier in Table 4.2, the presence of 9.98 % Pt and 3.82 % Cu for PtCu (70-24h) catalyst was proven. There is no NPs observation in the TEM image may mean that the size of the NPs may be much smaller than the TEM device can analyze and too small to determine their mean size diameter. In order to clarify this situation, taking a new image for PtCu (70-24) with a device that has a higher resolution (HR-TEM) mode is one of the future work parts of this thesis.

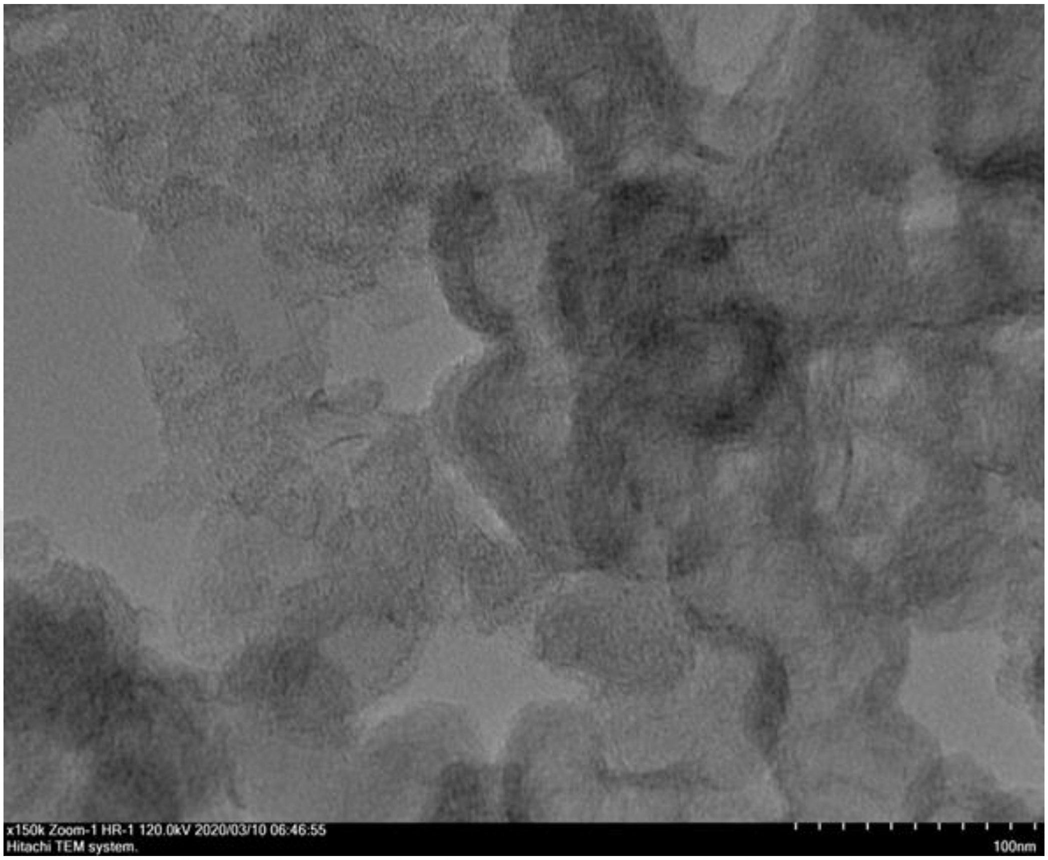

Figure 4.15: TEM image of PtCu (70-24h) (ruler: 100 nm).

PtCu (300-1h/70-24h) and PtCu (70-24h) were synthesized under similar conditions with the only difference as the prior calcination step of the support material for PtCu (300-1h/70-24h) NPs. So this fact enabled the NPs to be distinguished with the TEM device. This may be due to the reality that the surface of calcined hybrid carbon supports are more active than untreated carbon supports, which may result in faster nucleation and formation of slightly larger particle size.

TEM image and particle size histogram of PtCu (300-1h) and PtCu (300-4h) catalysts synthesized according to thermal decomposition method are shared in Figure 4.16.

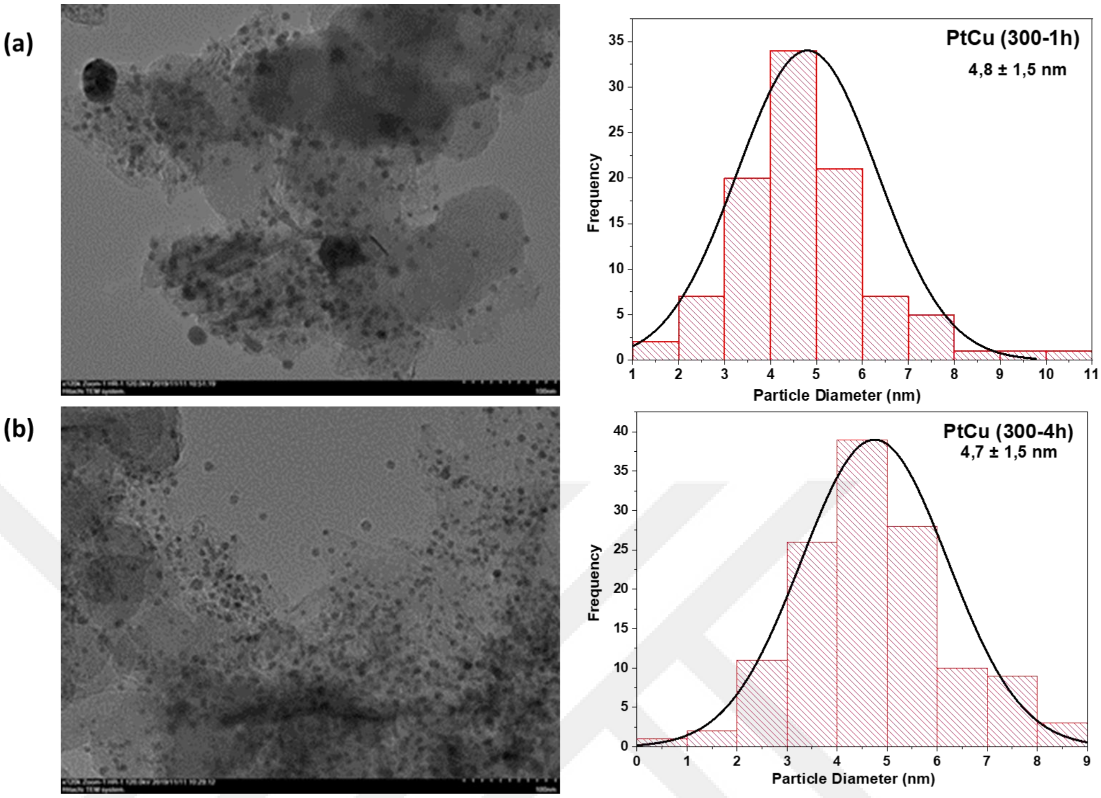

Figure 4.16: TEM and particle size histogram of (a) PtCu (300-1h) and PtCu (b) (300-4h) catalysts prepared according to thermal decomposition synthesis method (ruler: 100 nm).

When the images in Figure 4.16 are examined, it is seen there is regional agglomeration especially in the TEM image of the PtCu (300-1h) catalyst that synthesized at 300 ^{0}C for 1 hours under under dynamic varigon gas. On the other hand, in the TEM image of the PtCu (300-4h) catalyst that synthesized at 300 ^{0}C for 4 hours under under dynamic varigon gas, the presence of NPs attached on the carbon layer of the TEM grid is similar to the samples PtCu (120-2h) and PtCu (300-1h/70-24h) was observed. With observation of the particle sizes of both catalysts are very close to each other, the average particle size was calculated as 4.8 ± 1.5 nm and 4.7 ± 1.5 nm for PtCu (300-1h) and PtCu (300-4h), respectively. To sum up, according to TEM images, it can be said that the relationship between NPs and hybrid carbon support is stronger in the sample of PtCu (300-1h) unlike the other four synthesized catalysts.

Table 4.3 shows the average particle size calculated from TEM images for the synthesized MNPs. As that can be figure out from the results, PtCu (300-1h/70-24h) sample shows the smallest particle size among the synthesized catalysts, and PtCu (120-2h) sample shows the largest particle size, and no particles were observed in the PtCu (70-24h) sample.

Table 4.3: Average particle size of synthesized catalysts calculated based on TEM images.

Sample Code	**Average Particle Size (nm)**
PtCu (120-2h)	5.1 ± 1.5
PtCu (300-1h)	4.8 ± 1.5
PtCu (300-4h)	4.7 ± 1.5
PtCu (300-1h/70-24h)	2.5 ± 1.0
PtCu (70-24h)	NPs were too small

4.2.3. SEM-EDS Analysis

The EDS technique is performed by the SEM device and provides very helpful semi-quantitative information about the surface chemistry of the samples. In EDS technique, each element is represented by a specific color and the distribution of these elements on the surface can be presented visually by their mapping.

Figure 4.17 presents the mapping created using the EDS technique for synthesized PtCu (120-2h), PtCu (300-1h), PtCu (300-4h), PtCu (300-1h/70-24h) and PtCu (70-24h). In the images, green, yellow and red colors represent carbon, platinum, and copper elements, respectively. Although the surfaces of PtCu (300-1h/70-24h) and PtCu (70-24h) speciments are covered by carbon supports, a more homogeneous image is formed for the speciments PtCu (120-2h), PtCu (300-1h) and PtCu (300-4h). The surface of these synthesized bimetallic NPs is free of contamination and can interact directly with the reaction medium, ensuring that the catalytic activity is also more successful. Thus, this EDS mapping results may be a sign of presenting a challenge in electrocatalytic activity tests, especially for PtCu (300-1h/70-24h) and PtCu (70-24h) as electrocatalysts. Because electrocatalytic activity is carried out by the electrochemically active metals surface on the carbon support so the catalytic activity will be influenced positively by the direct interaction of metal surfaces with the reaction medium.

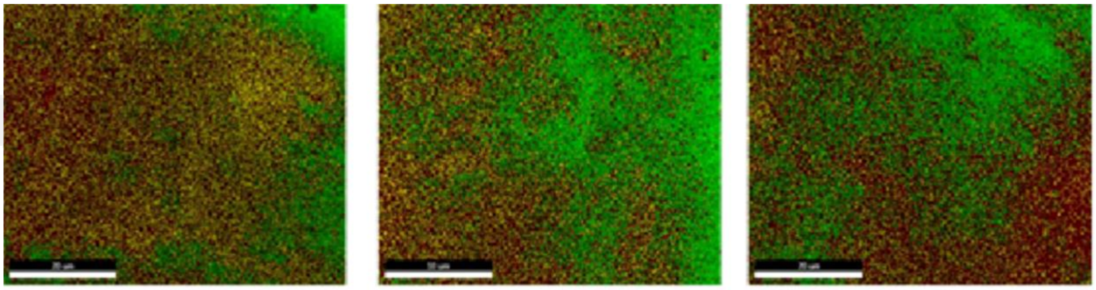

(a) PtCu (120-2h) **(b) PtCu (300-1h)** **(c) PtCu (300-4h)**

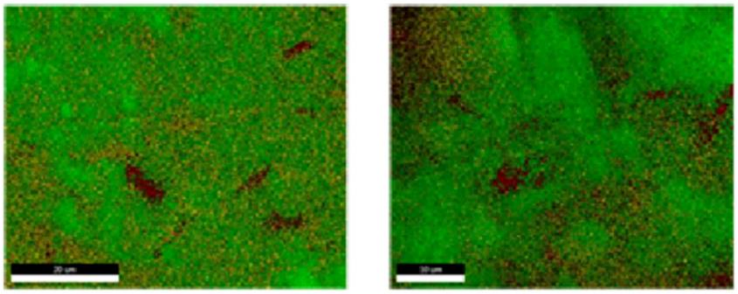

(d) PtCu (300-1h/70-24h) **(e) PtCu (70-24h)**

Figure 4.17: SEM-EDS mapping images of (a) PtCu (120-2h) NPs, (b) PtCu (300-1h) NPs, (c) PtCu (300-4h) NPs, (d) PtCu (300-1h/70-24h) NPs and (e) PtCu (70-24h) NPs; In the images, green, yellow and red colors represent carbon, platinum, and copper elements, respectively.

The numerical values of SEM-EDS results are given in Table 4.4. The atomic and molar distribution of the Pt and Cu elements values of the five synthesized catalysts were calculated based on these results also are given in the same table. According to these results, the total metal loading by weight percentage is calculated 31.37 %, 21.33 %, 26.10 %, 20.67 % and 24.84 % for PtCu (120-2h), PtCu (300-1h), PtCu (300-4h), PtCu (300-1h/70-24h) and PtCu (70-24h), respectively. However, at this point it should be kept in the mind that the EDS results are semi-quantitative and do not fully reveal the chemical compositions of the samples. On the other hand, SEM-EDS results prove that Pt and Cu elements are present in the structure of PtCu (70-24h) catalyst like ICP-MS results. This reinforces the claim that the bimetallic PtCu NPs formed in the PtCu (70-24h) catalyst are very small in size and therefore cannot be visualized with TEM.

Table 4.4. Results of weight, atomic and molar values of synthesized catalysts calculated according to SEM-EDS result.

Sample Codes	**C (K)**		**Pt (L)**		**Cu (K)**		**Atomic Ratio**	**Molar Ratio**
	Weight %	Atomic %	Weight %	Atomic %	Weight %	Atomic %		
PtCu (120-2h)	64,75	95,57	28,76	2,61	2,61	1,81	$Pt_{59}Cu_{41}$	Pt_3Cu_2
PtCu (300-1h)	78,67	97,78	17,64	1,35	3,69	0,87	$Pt_{61}Cu_{39}$	Pt_3Cu_2
PtCu (300-4h)	73,90	96,86	19,91	1,61	6,19	1,53	$Pt_{51}Cu_{49}$	Pt_1Cu_1
PtCu (300-1/70-24h)	79,33	97,94	17,54	1,33	3,13	0,73	$Pt_{65}Cu_{35}$	Pt_9Cu_5
PtCu (70-24h)	75,15	97,24	20,10	1,60	4,74	1,16	$Pt_{58}Cu_{42}$	Pt_7Cu_5

4.2.4. XRD Analysis Results

X-Ray diffraction (XRD) is a physical method which is used to gather information about the crystal structure of the material. In this technique, the X-ray diffractometer focuses on a pure material and a detector collects the X-rays produced as a result of the acceleration of the electron beams. XRD is based on the diffraction of X-rays in a characteristic order, depending on the atomic sequences of each crystal phase. These diffraction profiles for each crystal phase define the crystal like a fingerprint [143].

It is especially beneficial to use the XRD technique in order to understand whether the Pt (111) surface, which is the most active surface at the electrochemical interface under reactive conditions in Pt-based electrocatalysts, is distinct in the catalyst structure.

XRD spectra of PtCu (120-2h), PtCu (300-1h/70-24h) and PtCu (70-24h) catalysts prepared using organometallic synthesis method are shown in Figure 4.18.

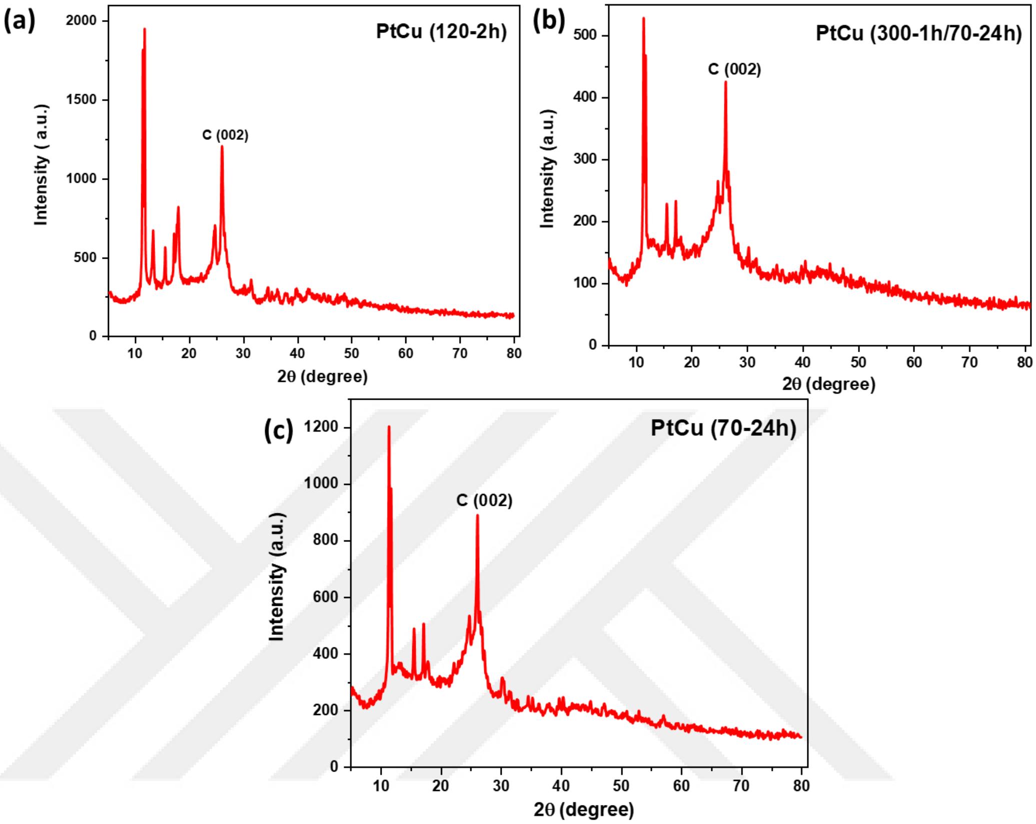

Figure 4.18: XRD spectrum of (a) PtCu (120-2h), (b), PtCu (300-1h/70-24h), and (c) PtCu (70-24h) NPs prepared by the organometallic synthesis method.

Five XRD peaks at 2θ (degree) = 11.36, 15, 54, 17.14, 24.72 and 26.10 are common in all three samples of PtCu (120-2h), PtCu (300-1h/70-24h), and PtCu (70-24h) NPs (Figure 4.18). The characteristic peak positioned at 26.10 corresponding to (002) lattice plane of graphite structure of carbon black. At 2θ=40-45, a hump (100) lattice peak indicate the presence of disordered amorphous carbon especially for PtCu (300-1h/70-24h), and PtCu (70-24h) catalysts. In addition to these peaks, there is another peak at 13.32° in the XRD spectrum of the PtCu (120-2h) catalyst. However, despite the presence of all these peaks, the fact that the apparent peak of the Pt (111) surface at ~40°, was not observed in the XRD spectrum for all three samples. Similar to the spesific Pt peaks, Cu (111), Cu (200) and Cu (220) peaks belonging to Cu at 45°, 40° and 75°, respectively, are not significant for all three catalysts.

The expected Pt and Cu peaks for PtCu (120-2h), PtCu (300-1h/70-24h) and PtCu (70-24h) catalysts were not observed in the XRD spectrum led to the idea that Pt and Cu complexes could still exist in these catalysts. The XRD spectrum was also taken for the metal complexes Pt $(acac)_2$ and Cu $(acac)_2$ used to validate this idea and are given in Figure 4.19. The XRD spectrum in Figure 4.19 may proves that the metal complexes still exist in the composition of PtCu (120-2h), PtCu (300-1h/70-24h), and PtCu (70-24h) catalysts synthesized according to the organometallic synthesis method despite repeated washing with pentane.

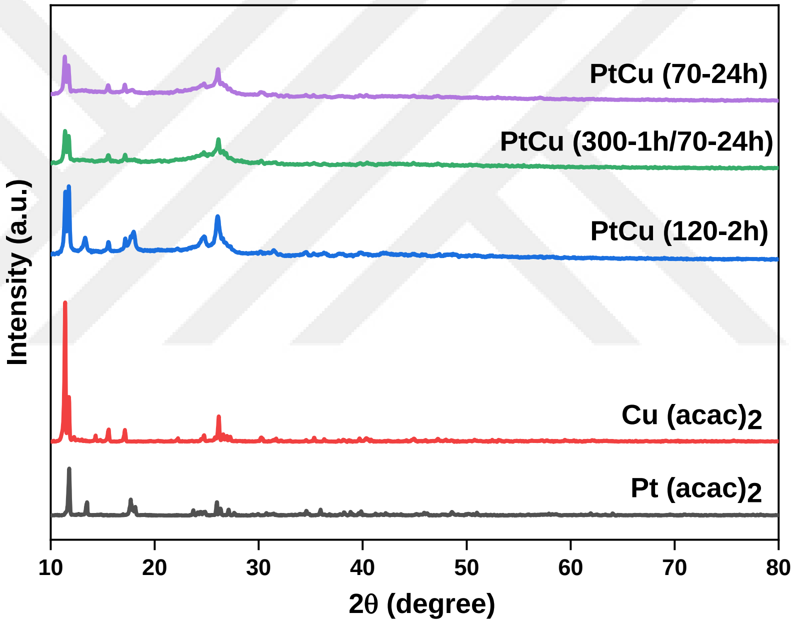

Figure 19: Comparative image of the XRD spectrum of metal complexes Pt $(acac)_2$ and Cu $(acac)_2$ with the XRD spectra of PtCu (120-2h), PtCu (300-1h/70-24h) and PtCu (70-24h) catalysts synthesized by organometallic synthesis method.

Contrary to the organometallic synthesis method, the peak of the face-centred cubic (fcc) Pt (111) surface in the XRD spectrum of the PtCu (300-1h) and PtCu (300-4h) catalysts prepared by thermal decomposition appeared at $2\theta = 40.66°$ and 40.80°, respectively (Figure 4.20) In addition to the Pt (111) surface, fcc Pt (200) and Pt (220) surfaces are also present in the XRD spectrum. Pt (200) peak is located at 47.06° for PtCu (300-1h) and at 46.68° for PtCu (300-4h). The peak of the Pt (220) surface is at $2\theta =$

68.44° and 68.82° for PtCu (300-1h) and PtCu (300-4h), respectively. The C (002) peak of the hybrid carbon support is at 26° in these NPs. No XRD peaks for nano Cu were found in both catalysts. This may be due to a possible overlap between the specific XRD peaks of both Pt and Cu at the similar location where the Cu peak is hidden under the Pt peaks.

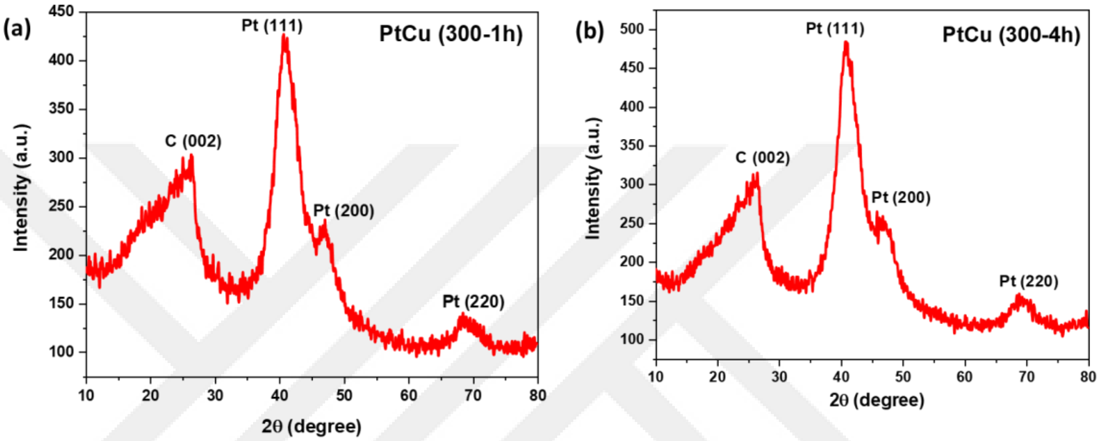

Figure 4.20: XRD spectra of (a) PtCu (300-1h) and (b) PtCu (300-4h) catalysts prepared by thermal decomposition method.

Based on all XRD results, it is concluded that the organometallic synthesis method to achieve PtCu (120-2h), PtCu (300-1h/70-24h) and PtCu (70-24h) NPs were less efficient due to milder reaction conditions compared to the thermal decomposition method used for PtCu (300-1h) and PtCu (300-4h) NPs. However, the fcc Pt peaks in the XRD spectrum for PtCu (300-1h) and PtCu (300-4h) NPs revealed that bimetallic PtCu decoration was successfully applied on the hybrid carbon support during the thermal decomposition.

This difference in the two synthesis methods may be that the mild reaction conditions that form the basis of the organometallic synthesis method may not be sufficient to successfully reduce metal precursors with the (acac) structure. In addition, unlike the thermal decomposition method, no gas enters and exits the reaction environment during the organometallic synthesis. This situation may result to reaction of organic structures separated from the metal precursor with the stable 3 bar H_2 gas to create

Hacac structure in the reaction environment and the binding of unwanted chemical species on the carbon support and the NPs [88].

4.2.5. Raman Analysis

Raman spectroscopy is a type of vibration spectroscopy, based on optical excitation where the wavelength of the absorbed light differs from the wavelength of the emitted light. This difference in wavelength is called as inelastic phonon scattering [144]. In Raman spectroscopy, vibrational transitions in the nucleus of a molecule are examined in the UV-Vis (400-800 nm) region. In the identification of an unknown sample, it is very important to know the energies of the scattering and vibrational transitions of the different molecules in the sample [145].

When working with carbon supported Pt-based electrocatalysts, the observation of the G and D bands characteristic for the carbon structure by Raman spectroscopy provides a significant knowledge for comprehension of the structure. The distinctive peaks of graphitic structures are the G peak near 1340 cm^{-1} which is created by sp^2 hybridized carbon atoms and D peak around 1590 cm^{-1} which is provided due to sp^3 hybridized carbon atoms of disordered graphene [146]. Moreover, the intensity ratio of D band to G band (I_D/I_G) provides very utility information about the structural organization of atoms on the carbon support. To describe the amount of disorder in carbon materials, the ratio of I_D/I_G is often used as a criterion. The D band is quite visible when the defects are present on the carbon lattice. Intensity of D band increases with the amount of defects. The Raman spectra of all the produced PtCu NPs are demonstrated in Figures 4.21 and 4.22.

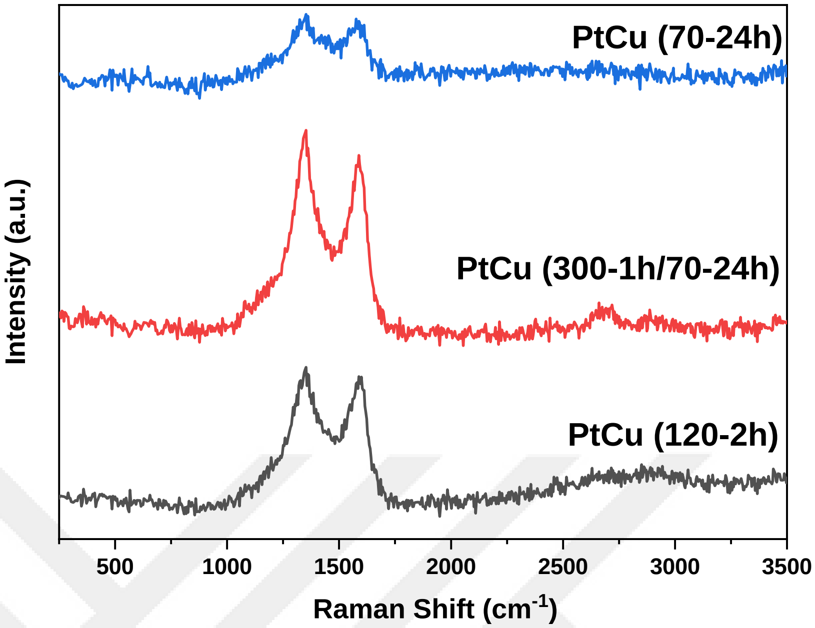

Figure 4.21: Raman spectra of PtCu (120-2h), PtCu (300-1h/70-24h) and PtCu (70-24h) catalysts prepared by organometallic method.

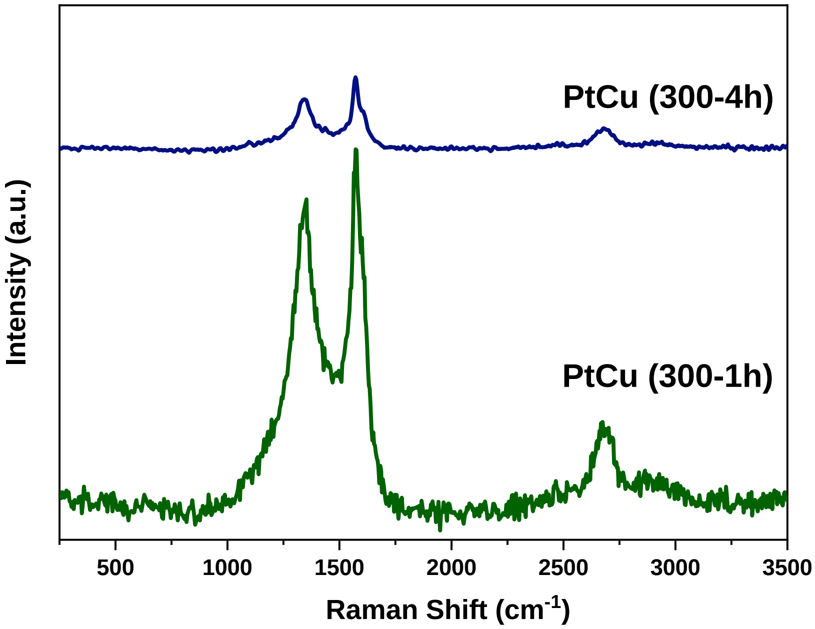

Figure 4.22: Raman spectra of PtCu (300-1h) and PtCu (300-4h) catalysts prepared by thermal decomposition.

Table 4.5: Calculated I_D/I_G and I_{2D}/I_G ratios for synthesized electrocatalysts.

Sample Codes	**I_D/I_G and I_{2D}/I_G Ratios**	
	I_D/I_G	**I_{2D}/I_G**
PtCu (120-2h)	1.01	0
PtCu (300-1h)	0.95	0.74
PtCu (300-4h)	0.95	0.88
PtCu (300-1h/70-24h)	1.04	0.78
PtCu (70-24h)	1.01	0

I_D/I_G and I_{2D}/I_G ratio were calculated with respect to Raman spectra and showed in Table 4.5. Although hybrid CB: GNP (50:50) is used as support material in all prepared catalysts, the defects on hybrid carbon will be different according to the preferred synthesis method. The results in Table 4.5 indicate that the PtCu (120-2h), PtCu (300-1h/70-24h) and PtCu (70-24h) samples prepared according to the organometallic synthesis method have higher I_D/I_G ratio than those of PtCu (300-1h) and PtCu (300-4h) which were prepared with the thermal decomposition method. Although organometallic synthesis method led to successful bimetallic PtCu decoration on the hybrid carbon support, still, both XRD and Raman spectroscopy indicated that thermal decomposition is the most suitable synthesis method for PtCu NPs formation. The reason why the organometallic synthesis method creates more defects on the carbon support is due to the interaction between the unreduced metal complexes and organic structures within the carbon support, in addition to the interaction of NPs and carbon support. The reason for the relatively higher I_D/I_G ratio of PtCu (300-1h/70-24h) compared to the other two catalysts among the organometallic synthesis method may be that the hybrid carbon support was pre-calcined at 300 ^{0}C under dynamic varigon gas for 1 hour.

In addition to the D and G bands observed in the Raman spectra, there is a third peak called 2D peak at ~2700 cm^{-1} for PtCu (300-1h), PtCu (300-4h) and PtCu (300-1h/70-24h) catalysts. The 2D band is the distinctive peak for the graphene structure where the I_{2D}/I_G ratio is dependent on the number of graphene layers [147]. Different ratio of I_{2D}/I_G as ∼2–3, 2> I_{2D}/I_G> 1 and I_{2D}/I_G <1 is usually an monolayer graphene, bilayer graphene and multilayer one, respectively [148]. According to the results in Table 4.5, the I_{2D}/I_G

band is less than 1 in these three samples. This represent that the hybrid carbon support (CB:GNP=50:50) features multilayer graphene for these three type of PtCu NPs. The common point of these three samples is that, the hybrid carbon support in all was treated with dynamic varigon gas at 300 ^{0}C. For PtCu (300-1h), PtCu (300-4h), this process is the preferred synthesis method for generation of bimetallic NPs is thermal decomposition while for the PtCu (300-1h/70-24h) catalyst prepared according to the organometallic synthesis method, this process is the calcination of carbon supports before synthesis. The specific 2D band for graphene was not observed in PtCu (120-2h) and PtCu (70-24h) NPs prepared with the organometallic synthesis method. Considering the superior electrochemical and mechanical properties of graphene, the graphene-derived formation of the carbon support can provide an advantage to catalysts in electrochemical tests.

4.2.6. XPS Results

XPS technique is a surface sensitive characterization method and provides valuable information about the chemical state of the relevant substance. This technique is usually carried out by exciting testing surfaces with mono-energetic Al ka x-rays that allow photoelectrons to be released from the sample surface. An electron energy analyzer is required to evaluate the energy of the photoelectrons emitted. The atomic identity, the chemical state and the quantity of the measured element can be defined from the binding energy and intensity of the photoelectron peak [149].

The XPS technique provided useful knowledge for the determination of the chemical state especially of Pt and Cu elements in five distinct bimetallic PtCu synthesized electrocatalysts. In Figures 4.23, 4.24 and 4.25, XPS results obtained for Pt 4f, Cu 2p and C 1s and O 1s of bimetallic PtCu catalysts are shared, respectively. According to these results, the presence of both Pt and Cu nanoparticles in all synthesized PtCu catalysts has been proven, and the idea of very small particle size to be viewed with a TEM device, which suggested for the PtCu (70-24h) catalyst is encouraged.

According to the XPS results, it is observed that the metallic Pt (Pt ^{0}) is the most dominant form of Pt among all the synthesized bimetallic catalysts (Figure 4.23). Contrary to PtCu (300-1h), PtCu (300-4h) and PtCu (70-24h) catalysts, Pt $^{+2}$ and Pt $^{+4}$ peaks were not observed in PtCu (120-2h) and PtCu (300-1h/70-24h) catalysts which may belong to PtO and PtO_2 structure, respectively. These results contribute in particular to the presence of a Cu-rich formation in the samples PtCu (120-2h) and PtCu (300-1h/70-24h), which avoids the oxidation of Pt and serves as a shell on the external surface. Although this situation inhibits the oxidation of Pt, it may cause Cu nanoparticles, which are non-nobel metal and easily oxidized in acidic environment, to leach on the carbon support and adversely affect electrochemical performance during electrochemical tests.

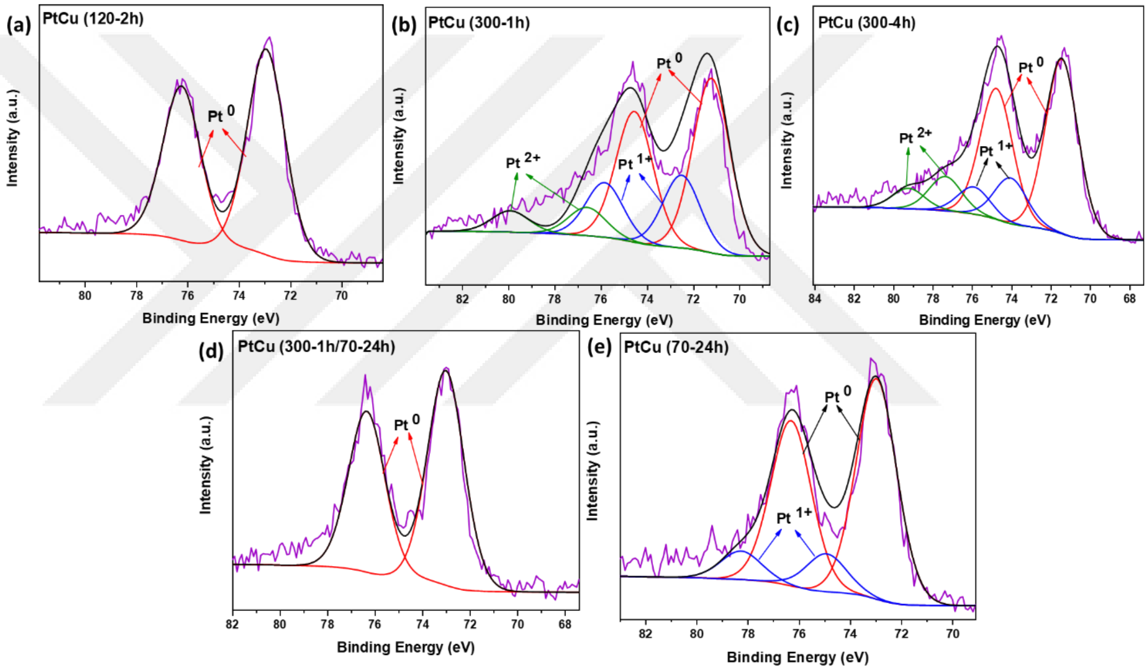

Figure 4.23: Pt 4f XPS data of (a) PtCu (120-2h), (b) PtCu (300-1h), (c) PtCu (300-4h), (d) PtCu (300-1h/70-24h), and (e) PtCu (70-24h).

It was previously reported that the peaks corresponding to metallic Pt 4f $_{7/2}$ and Pt 4f $_{5/2}$ were positioned at 71 eV and 74 eV, respectively [150]. The shifting of these values towards high energy binding energy refers to the interaction of Pt and Cu metal atoms in the bimetallic alloy structure and to the interaction of PtCu NPs on the carbon support. For all synthesized bimetallic nanostructures, the Pt 4f peak shifted to high binding energy (Table 4.6), an indication of the interaction between bimetallic PtCu NPs and carbon support [151]. However, when examined with the value in Table 4.6, it can be shown that the shift to high energy is more clear in catalysts synthesized by the organometallic synthesis method.

The XPS results for Cu 2p demonstrated that there is no metallic Cu in PtCu (120-2h), PtCu (300-1h/70-24h) and PtCu (70-24h) catalysts synthesized by the organometallic synthesis method (Figure 4.24). Unlike these three catalysts, the presence of metalic Cu located at about 932 eV was observed for catalysts PtCu (300-1h) and PtCu (300-4h) (Table 4.6). The peaks observed at approximately 939-944.2 eV for , (120-2h), PtCu (300-1h/70-24h) and PtCu (70-24h) catalysts are called the satellite peaks associated with a shake up process of the open $3d^9$ shell of Cu $^{+2}$ [152]. The appearance of a well-known shake-up satellite in the Cu 2p spectra as an indicator of the existence of the Cu(II) species is well known [152]. Although Cu (II) presence was detected in all synthesized catalysts, the satellite peak was detected only in catalysts synthesized by organometallic synthesis method used under milder conditions (70°C, 3 bar H2, 24 h). This experimental result is most likely due to the presence of unreacted $Cu(acac)_2$ metal complex in the PtCu (120-2h), PtCu (300-1h/70-24h) and PtCu (70-24h) catalysts structure and thus further optimization of the reaction conditions and the purification steps are necessary.

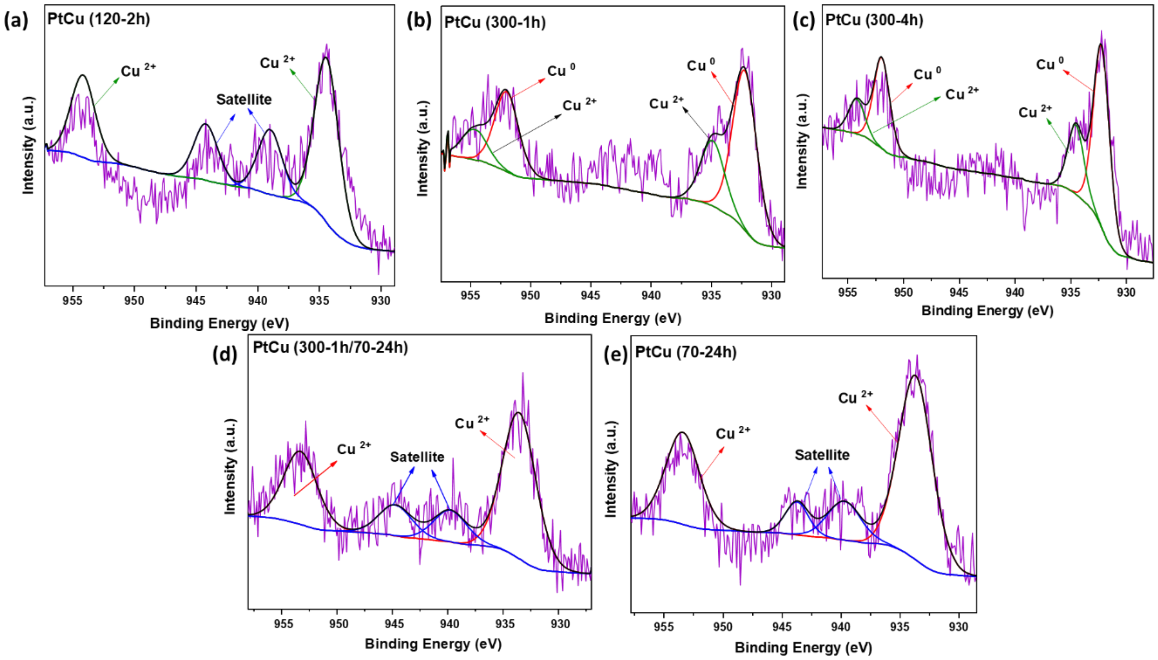

Figure 4.24: Cu 2p XPS data of (a) PtCu (120-2h), (b) PtCu (300-1h), (c) PtCu (300-4h), (d) PtCu (300-1h/70-24h), and (e) PtCu (70-24h).

The C 1s and O 1s XPS spectra of the synthesized PtCu NPs are shared in Figure 4.25. The C 1s spectrum for all catalysts was similar, and the C 1s region was detected at around 284.5 eV. Obtaining a peak at similar binding energies for C 1s in all bimetallic catalysts indicates successful nanoparticle decoration on carbon support for all catalysts. However, considering the fact that all catalysts were synthesized air-sensitively, it should be noted that the shifts observed in O 1s will give critical information about the catalyst structure. When the binding energy values in Table 4.16 are examined, it is seen that there are significant shifts for O 1s depending on the synthesis method. The observation of O 1s peak at nearly 532 and 533 eV for catalysts synthesized by the organometallic synthesis method and by thermal decomposition method, respectively. This result can suggest that the catalysts surfaces show different properties. Thus, it is seen that the XPS results coincide with the FTIR and XRD results.

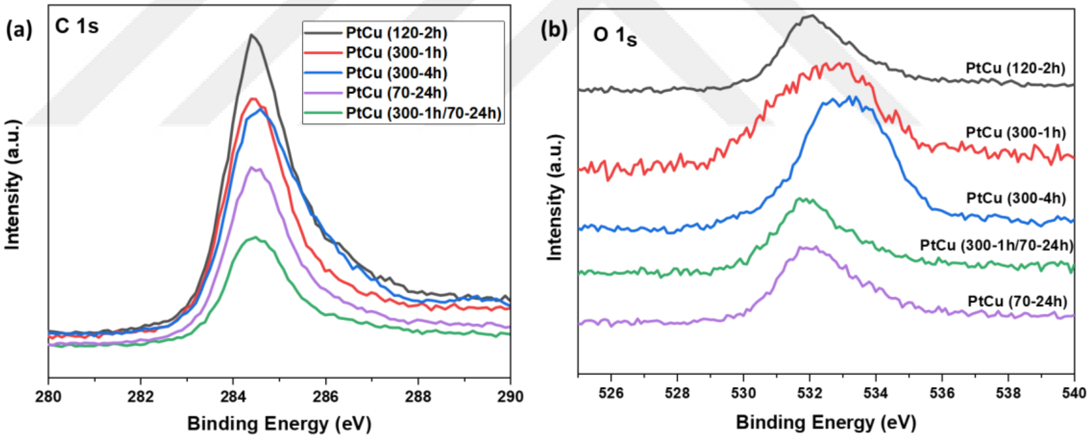

Figure 4.25: The XPS data of (a) C 1s and (b) O 1s.

Table 4.6: Pt 4f, Cu 2p, C 1s and O 1s binding energies of synthesized catalysts.

Sample Codes	**Binding Energy (eV)**											
	Pt ^{0} 4f		**Pt $^{2+}$ 4f**		**Pt $^{4+}$ 4f**		**Cu ^{0} 2p**		**Cu $^{2+}$ 2p**		**C 1s**	**O 1s**
	Pt 4f $_{7/2}$	**Pt 4f** $_{5/2}$	**Pt 4f** $_{7/2}$	**Pt 4f** $_{5/2}$	**Pt 4f** $_{7/2}$	**Pt 4f** $_{5/2}$	**Cu 2p** $_{3/2}$	**Cu 2p** $_{1/2}$	**Cu 2p** $_{3/2}$	**Cu 2p** $_{1/2}$		
PtCu (120-2h)	72.93	76.23	---	---	---	---	---	---	934.4	954.15	284.4	532.1
PtCu (300-1h)	71.2	74.53	72.5	78.83	76.58	79.91	932.21	951.96	934.87	954.62	284.5	532.9
PtCu (300-4h)	71.73	74.76	74.03	77.36	75.91	79.24	932.2	951.95	934.50	954.20	284.6	533.3
PtCu (300-1h/70-24h)	73.01	76.34	---	---	---	---	---	---	933.5	953.20	284.5	531.7
PtCu (70-24h)	72.97	76.30	74.93	78.26	---	---	---	---	933.63	953.40	284.6	531.9

4.3. Electrochemical Characterization by Cyclic Voltammetry

Many electrochemical tests are available including potential step, potential sweep, rotating disc electrode, rotating ring disc electrode, impedance spectroscopy, cycling voltammetry (CV) in the litreture. A basic electrochemical process is completed in 4 steps. First, the reactants are transported to the electrode surface and then these reactants are absorbed at the electrode surface. In the following third step, charge transfer is provided by redox reactions between the electrode surface and the reactant, and as a result, the final products are transported from the electrode surface [153].

4.3.1. Experimental Methods

3 electrode system is used as an electrochemical cell for the following CV studies as shown in Figure 4.26.

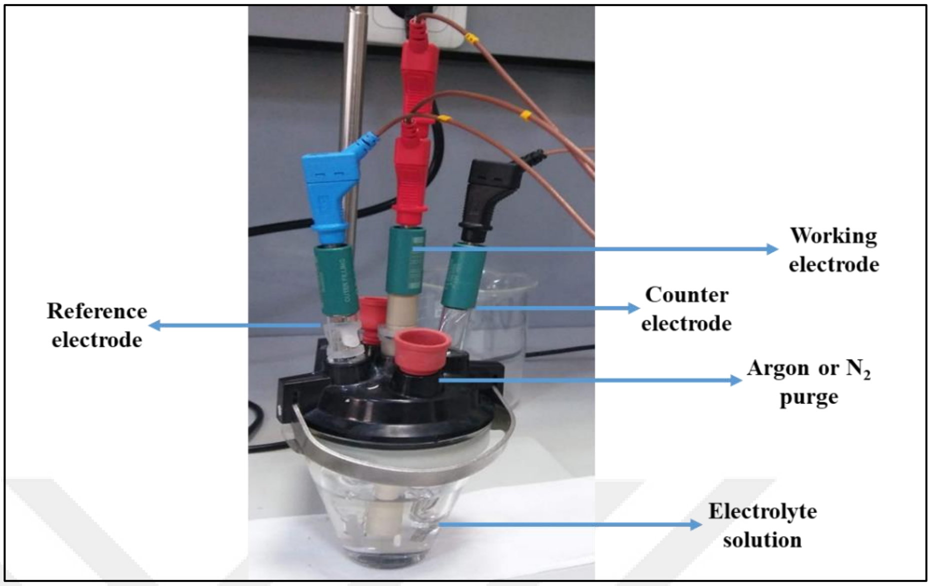

Figure 4.26: A three-electrode system.

The electrodes mentioned as three electrodes are respectively working electrode (WE), counter electrode (CE) and reference electrode (RE). The working electrode can be formed of carbon, gold or platinum embedded in glass or similar inactive material. The counter electrode is made of platinum with a large surface area in order for electrochemical reactions to occur rapidly on its surface. Each of the following electrodes will usually be used as a reference electrode; $Pt/H_2/H^+$ (standard/dynamic/normal hydrogen electrode) or $Ag/AgCl/Cl^-$ (silver/silver chloride electrode) or $Hg/Hg_2Cl_2/Cl^-$ (calomel electrode) [153].

The material to be electrochemical tested creates the working electrode where the passing potential or current will be measured. The WE can create a circuit with the CE and the current generated can pass through this circuit. In addition, beside the working electrode the CE can also react electrochemically. However, it is not necessary to measure the electrochemical reaction created by the counter electrode and it should never interact with WE. The main function of the reference electrode, the third electrode system, is to reduce the resistance on the WE potential of the electrolyte solution by making another circuit with RE.

In this part of the thesis, the preferred triple electrode; WE, CE and RE request for CV tests is; 3 mm diameter glassy carbon, platinum plate and silver / silver chloride electrode, respectively.

4.3.2. Cyclic Voltammetry Results

Cyclic voltammetry (CV) is an effective and widespread electrochemical technique widely used to explore the mechanisms of reduced or oxidized molecular species. In the research of electron transfer-initiated chemical processes, which involve catalysis, CV is also valuable [153].

One of the most important points in achieving correct results in CV studies is the proper preparation of the working electrode. At this point, the prepared ink should be properly applied to the conductive part of the working electrode. While preparing the ink, alcohol, water and any other solvent that can dissolve the catalyst powder should be used. Nafion polymer is also added to this mixture to increase adhesion. The working electrode, on which the prepared catalyst ink is dropped, is then left to dry for a certain period of time. The drying process of the ink is critical for the catalyst layer to adhere homogeneously on the glassy carbon. Therefore, the drying process should be done at the lowest possible temperature and slowly.

It is necessary to find the required electrolyte solution during the analysis of cyclic voltametry in order to receive a reliable cyclic voltagram. Dilute acid solution (ranging from 0.1 to 1 M) is commonly utilized as an electrolyte solution as it supplies the proton during electrochemical reactions. The most common electrolytes in the literature are that H_2SO_4 and $HClO_4$. However, considering the possibility of poisoning the Pt catalyst with the sulfur in the H_2SO_4, it is more appropriate to use $HClO_4$ as an electrolyte [154]. This prepared electrolyte solution is purged with inert gas for at least 15 minutes. The purge process with an inert gas must continue while CV experiments continue to obtain the best CV voltagram.

The CV voltagram of the commercial PEM fuel cell catalyst; commercial 20 % wt. Pt on Carbon Vulcan XC-72 with 5 different bimetallic PtCu catalysts prepared by using organometallic synthesis and thermal decomposition method is given in Figure 4.27.

While preparing the working electrode for CV tests, the required amount of Pt was calculated according to the WE electrode area such that 25 micrograms Pt per 1 cm^2. 0.1 M $HClO_4$ was used as the electrolyte. The potentiostat brand used for CV studies was Metrohm Autolab Nova 2.1. Before the voltagram was taken, the device was conditioned to 50 cycles at scan rate of 0.1 V/s.

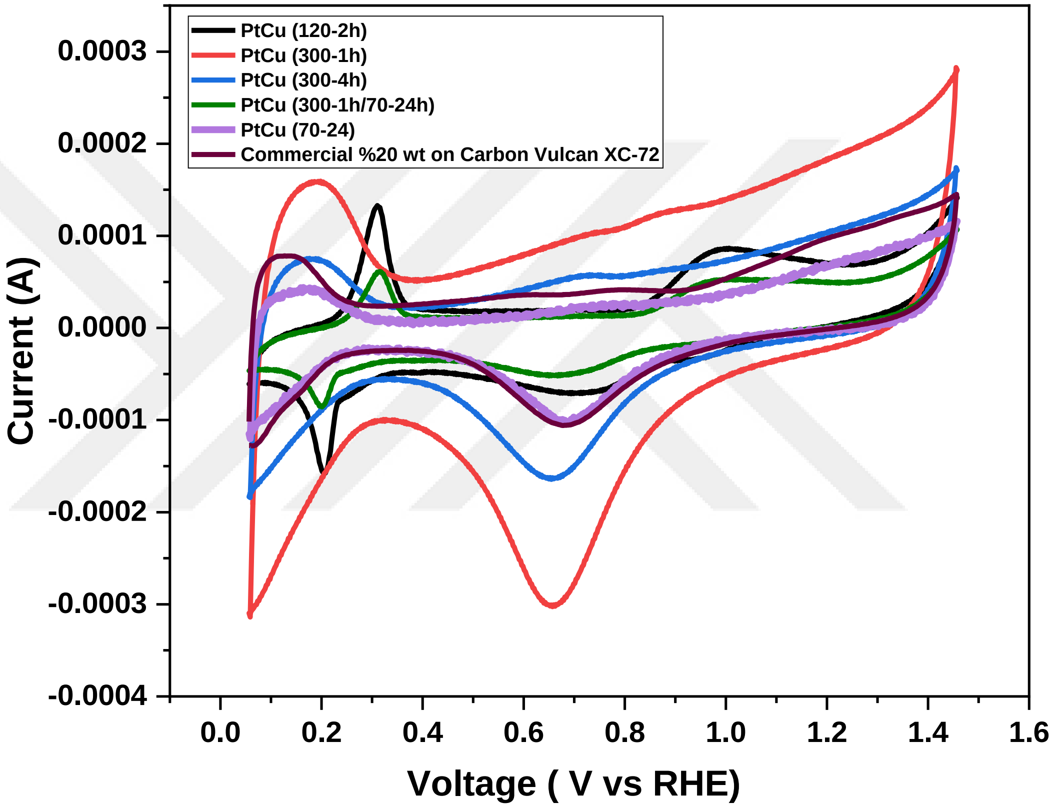

Figure 4.27: Cyclic voltagram in 0.1 M $HClO_4$ of PtCu (120-2h), PtCu (300-1h), PtCu (300-4h), PtCu (300-1h/70-24h), PtCu (70-24h) and commercial %20 Pt on carbon Vulcan XC-72.

4.3.3. Determination of Electrochemical Surface Area

One of the most important information provided by the voltagram obtained at the end of CV studies is the calculation of the ECSA value on this voltagram. The electrochemical surface area (ECSA) of the electrode can be measured by the CV technique using the hydrogen desorption mechanism. For this, the catalyst ink, whose details are mentioned above, is dropped to the glassy carbon electrode and dried, and then it included in the 3 electrode system as a working electrode and the CV voltagram is taken. Hydrogen desorption and absorption peaks are detected after the measurement. And the area of these peaks gives an ECSA value estimate [155]. The ECSA value can be calculated using the formulation given in Equation 4.1 [155].

$$ECSA\ [\ cm^2\ \frac{Pt}{g}\ \text{of Pt}\ ] = \frac{\text{Charge}\ [Q_H,\ \mu\ \frac{C}{cm^2}\ ]}{210\ \left[\mu\ \frac{C}{cm^2}\right] X\ electrode\ loading\ [\ g\ of\ \frac{Pt}{cm^2}]} \tag{4.1}$$

The ECSA value provides an idea of the active surface of the catalyst for charge transfer and the conductive direction for electron transfer in the electrode surface [155]. A total of 5 cycles were made at scan rate of 0.05 V/s for each sample and the third cycle of all catalysts was used for ECSA calculation. The values found for each catalyst according to the ECSA calculation and the particle size according to TEM results made are presented in Table 4.7.

Table 4.7: Particle size and ECSA values of and commercial PtCu (120-2h), PtCu (300-1h), PtCu (300-4h), PtCu (300-1h/70-24h), PtCu (70-24h) and %20 Pt on Vulcan XC-72.

Catalys Types	**Particle Size**	**ECSA (m^2/g_{Pt})**
PtCu (300-1h)	**4.8 ± 1.5**	**99**
PtCu (300-4h)	**4.7 ± 1.5**	**52**
PtCu (120-2h)	**5.1 ± 1.5**	**34**
PtCu (70-24h)	**——**	**33**
PtCu (300-1h/70-24h)	**2.5 ± 1.0**	**16**
Commercial %20 wt Pt on Carbon Vulcan XC-72	**——**	**42**

The trend for increasing ECSA values were as follows:
PtCu (300-1h) NPs > PtCu (300-4h) NPs > Commercial 20 % wt Pt > PtCu (120-2h) NPs > PtCu (70-24h) NPs > PtCu (300-1h/70-24h) NPs.

The best result was achieved with PtCu (300-1h) NPs with 99 m^2/g_{Pt}. Higher ECSA values were observed for Pt (300-1h) NPs and Pt 300-4h) NPs compared to that of the commercial Pt. Contrary to this situation, ECSA values of PtCu (120-2h), PtCu (300-1h/70-24h) and PtCu (70-24h) catalysts prepared by organometallic synthesis method were lower than that of the commercial Pt catalyst. No direct correlation between the ECSA values and the particle size was observed. The ECSA value of PtCu (300-1h/70-24h) catalyst, which has the smallest bimetallic PtCu NPs among the five synthesized catalysts, was found to be the lowest. In addition, the ECSA value of the PtCu (70-24h) catalyst is larger than PtCu (300-1h/70-24h) and almost the same as PtCu 8120-2h).

The CV voltagram in Figure 4.27 also proves that the PtCu (120-2h) and PtCu (300-1h/70-24h) samples prepared by the organametallic synthesis method, still have unreduced metal complexes in the structure despite washing with pentane. The peaks between 0.2 V and 0.4 V in both direction are related to the breakdown and re-deposition of bulk Cu [133]. To make this situation more apparent, the CV voltagram of the metal precursors; $Pt(acac_{)2}$ and $Cu(acac)_2$ were taken using the CH brand potentiostat and the CV results of the metal complexes are presented in Figure 4.28.

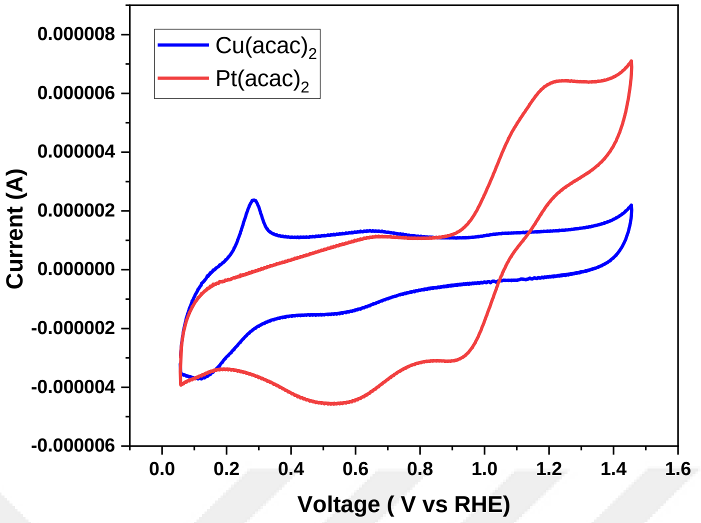

Figure 4.28: Cyclic voltagram in 0.1 M $HClO_4$ results of Pt(acac)$_2$ and Cu(acac)$_2$ metal complexes.

When the CV voltagrams in Figure 4.27 and Figure 4.28 are examined, it is seen that the oxidation peaks at 0.28 V and 0.98 V for PtCu (120-2h) and PtCu (300-1h/70-24h) originate from Cu (acac)$_2$ and Pt (acac)$_2$ complexes, respectively. Thus, it is exhibited that these metal complexes still exist in the catalyst structure. Unlike PtCu (120-2h) and PtCu (300-1h/70-24h) catalysts, these peaks were not observed in CV voltagram for PtCu (70-24h) catalyst prepared by organometallic synthesis method. It is interesting that PtCu (70-24h) has drawn a different voltagram in CV experiments, although it has almost the same crystal structure as PtCu (120-2h) and PtCu (300-1h/70-24h) catalysts according to XRD results.

After a series of structural characterization and CV studies, it was recognized that the especially PtCu (300-1h) sample synthesized under dynamic varigone gas at 300 ^{0}C for 1 hour via thermal decomposition method, was superior to the other four PtCu NPs as an electrocatalyst. Therefore, in the next chapter, the preferred synthesis method for PtCu (300-1h) will be used as the synthesis method (300 ^{0}C, 1 hour, under dynamic varigon gas) in studies to understand how the changing CB:GNP ratios will affect the bimetallic PtCu NPs formation and the behavior of these NPs as electrocatalysts.

5. EFFECT of DIFFERENT CB:GNP RATIOS on the FORMATION of BIMETALLIC PtCu NANOPARTICLES and a COMPRASION of THEIR ELECTROCHEMICAL ACTIVITIES

5.1. Experimental Method

This chapter focuses on the optimization of the hybrid support ratio used for bimetallic PtCu NPs as an attempt to achieve favorable electrochemical properties for the nanomaterial. The preparation method was chosen according to our previous studies on the optimization of reaction conditions. For all the PtCu NPs prepared in this section, the reaction conditions for their preparation were the same.

5.1.1. Preparation of Bimetallic PtCu (300-1h), PtCu (300-1h/30:70), PtCu (300-1h/70:30) and Monometallic Pt (300-1h/50:50) and Cu (300-1h/ 50:50) Electrocalysts

For all the catalysts prepared in this section, the conditions for the preparation of the catalyst PtCu (300-1h) were used. First, all powders were prepared in a glove box with total 20% metal loading on the hybrid carbon support. For all bimetallic PtCu catalysts; Pt $(acac)_2$ (117,9) mg and Cu $(acac)_2$ (78,5 mg) were impregnated hybrid CB: GNP support (CB:GNP (155,2 mg : 155,2 mg), CB:GNP (93,12 mg : 217,28 mg) and CB:GNP (217,28 mg : 93,12 mg)). These powders were then taken out of glove box within a balloon flask and finally, it was exposed to dynamic varigon gas at 300 ^{0}C for 1 hour to form nanoparticles. Than, all spicements were washed with pentane (5 x 40 mL) under an argon atmosphere. The same procedure was repeated with Pt $(acac)_2$ (157.32 mg) and CB:GNP (155.2 mg : 155.2 mg), and Cu $(acac)_2$ (261.7 mg) and CB:GNP (155.2 mg : 155. 2 mg) to achieve pure, monometallic Pt NPs and Cu NPs, respectively.

In the previous section it was shown that these synthesis conditions allow the formation of well-defined bimetallic PtCu NPs on the hybrid carbon support. In order to further understand the interaction of the two metals, their monometallic form, Pt (300-1h/50:50) NPs and Cu (300-1h/50:50) NPs were also synthesized and characterized.

Details of the catalysts synthesized in this section are given in Table 5.1. The PtCu (300-1h) catalyst was re-synthesized and the hybrid carbon support ratios for the monometallic Pt (300-1h/50:50) and Cu (300-1h/50:50) catalysts were set to CB: GNP 50:50 (w:w). All structural and electrochemical tests of the re-synthesized PtCu (300-1h) catalyst, were re-performed, except TEM in this section. The hybrid carbon support ratios; CB:GNP of the bimetallic samples PtCu (300-1h/30:70) and PtCu (300-1h/70:30) were determined as 30:70 (w:w) and 70:30 (w:w), respectively.

Table 5.1: Composition and synthesis conditions of the relevant catalysts.

Sample Codes	**Monometallic/ Bimetallic**	**Composition**	**Carbon Support Ratio (w:w)**	**Synthesis Condition**
Pt (300-1h/50:50)	Monometallic	Pt/CB:GNP	CB:GNP(50:50)	300 ^{0}C, 1 hour, under dynamic varigon gas
Cu (300-1h/50:50)	Monometallic	Cu/CB:GNP	CB:GNP(50:50)	300 ^{0}C, 1 hour, under dynamic varigon gas
PtCu (300-1h)	Bimetallic	PtCu/CB:GNP	CB:GNP(50:50)	300 ^{0}C, 1 hour, under dynamic varigon gas
PtCu (300-1h/30:70)	Bimetallic	PtCu/CB:GNP	CB:GNP(30:70)	300 ^{0}C, 1 hour, under dynamic varigon gas
PtCu (300-1h/70:30)	Bimetallic	PtCu/CB:GNP	CB:GNP(70:30)	300 ^{0}C, 1 hour, under dynamic varigon gas

Although, theoretically, catalysts were prepared with 20% metal loading, the ICP-MS analysis was carried out to determine whether there is a metal loss in the catalyst structure during the reduction process and after the pentane washing step. ICP-MS results are reported in Table 5.2. According to the ICP-MS results, it is claimed that there is no significant metal loss in the catalysts except Cu (300-1h/50:50).

Table 5.2: ICP-MS results of synthesized catalysts.

Sample Code	% weight of Pt	% weight of Cu
Pt (300-1h/50:50)	18.73	0
Cu (300-1h/50:50)	0	14.79
PtCu (300-1h)	15.24	5.05
PtCu (300-1h/30:70)	14.48	4.74
PtCu (300-1h/70:30)	15.87	4.88

5.2. Results and Discussion

5.2.1. BET Analysis

The physical adsorption of gas molecules on a solid surface is clarified by Brunauer, Emmett, and Teller (BET) theory and provides a foundation for an important technique of analysis for the calculation of the specific surface area and porosity of substances. A high specific surface area of the carbon supports preferred for use in PEM fuel cells is an important parameter for being a good support material. High surface area carbon supports allow the nanoparticles forrmation without agglomeration and high pore volume results in more triple phase boundaries of nanoparticles [156].

In a recent study of our research group, the total surface area of CB, GNP and CB:GNP (50:50) was found as 207 m^2/g, 759 m^2/g and 397 m^2/g from the BET analysis, respectively [20].

In this study, BET analysis was performed for various CB:GNP ratios as 50:50, 30:70 and 70:30 to understand how hybrid carbon support ratios have an effect on specific surface area and porosity. The BET analysis result of the relevant carbon supports is given in Table 5.3. As expected, as the CB ratio increases in the hybrid carbon structure, the both total surface area and total pore volume decrease. Among these three carbon supports, CB:GNP (30:70) exhibits the highest total surface area and total pore volume.

Table 5.3 BET analysis of carbon support materials.

Carbon Support Material	**Total Surface Area (m^2/g)**	**Total Pore Volume (cm^3/g)**
CB:GNP (50:50)	480.4	0.60
CB:GNP (30:70)	538.6	0.67
CB:GNP (70:30)	361.9	0.45

5.2.2. TEM Analysis

TEM images were taken for the relevant catalysts in order to analyze the morphology and size of these NPs. The size distributions of the particles are also calculated based on the TEM images. Thus, detailed information was obrained about the distribution, agglomeration and average particle size of monometallic and bimetallic NPs on the hybrid carbon support.

It is understood from the images in Figure 5.1 that the thermal decomposition method performed under dynamic varigone gas at 300 ^{0}C for 1 hour is suitable for the formation of monometallic nano-sized Pt and Cu structures on the hybrid carbon support CB:GNP (50:50). According to the size histograms, mean particle diameter of the NPs were 8.1±2.2 nm for monometallic Pt (300-1h/50:50) and 5.6±2.0 nm for monometallic Cu (300-1h/50:50). As reported in the previous chapter, the particle size of the bimetallic CB:GNP (50:50) carbon supported PtCu (300-1h) sample synthesized under the same synthesis conditions was 4.8 ±1.5 nm (Figure 4.16). These results indicate that the monometallic Pt and Cu NPs have a larger particle size than the bimetallic PtCu NPs under the same synthesis conditions. The results also show the particle size of the monometallic Pt (300-1/50:50) NPs is larger than the monometallic Cu (300-1h/50:50) NPs. It can also be interpreted as Pt $(acac)_2$ complex is reduced faster than Cu $(acac)_2$ complex under the same synthesis conditions and particle size grows faster accordingly. On the other hand, when these two complexes came together, interestingly, they were able to form the bimetallic PtCu NPS, whose particle size was smaller than either both monometallic catalysts. This can be explained by the fact that in bimetallic structures, metals affect each other synergitically and catalytically, and thus, nano-sized catalysts that superior to monometallic structures can be created. From the TEM images, it is also recognized the NPs formed in both monometallic structures are not fully spherical.

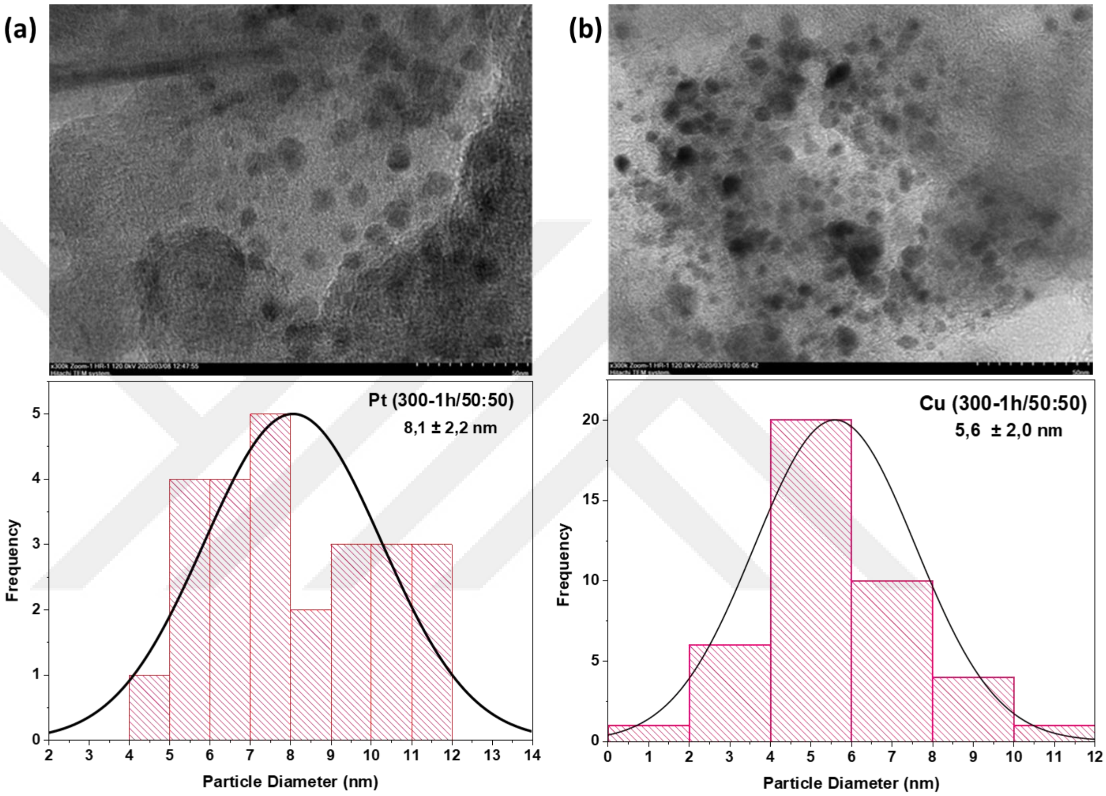

Figure 5.1: TEM images and particle size histogram of (a) Pt (300-1h/50:50) and (b) Cu (300-1h/50:50); ruler: 50 nm.

In Figure 5.2, TEM images are shared for PtCu (300-1h/30:70) and PtCu (300-1h/70:30) prepared by changing the hybrid carbon support ratios with the TEM image of PtCu (300-1h) catalyst that previously shared. The relevant TEM images prove bimetallic NPs formation was achieved successfully even if the carbon support ratios are changed. Based on the TEM images, it can be said that the distribution of bimetallic PtCu on the hybrid carbon support is homogeneous as intended. According to the size histograms, mean particle diameter of the NPs were 6.3±1.9 nm and 5.4±1.6 nm for PtCu (300-1h/30:70) and PtCu (300-1h/70:30), respectively. The particle size of both NPs is greater than the particle size of the PtCu (300-1h) catalyst. Considering that the synthesis conditions for these three catalysts are the same and the only difference between them is the carbon support ratio, it is concluded that the hybrid carbon support ratio should be is CB:GNP (50:50) for the formation of smaller NPs. Although the particle size is smaller than the other two catalysts, the PtCu (300-1h) catalyst has some local agglomeration that is a matter of consideration.

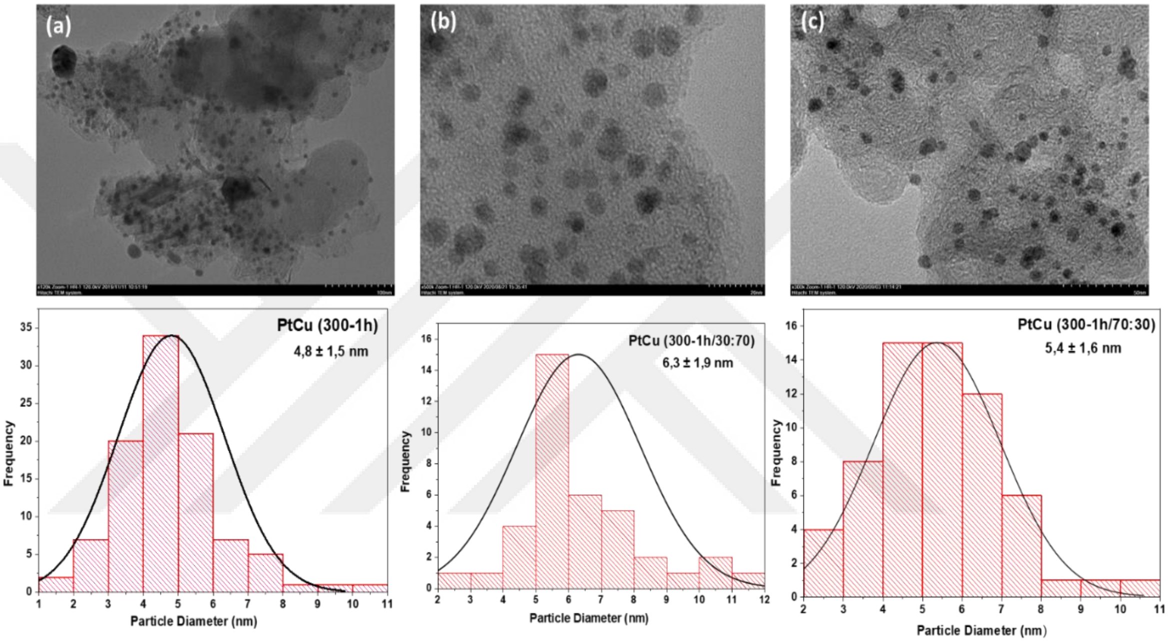

Figure 5.2: TEM images and particle size histogram of (a) PtCu (300-1h), (b) PtCu (300-1h/30:70) and (c) PtCu (300-1h/70:30); ruler: 100 nm for PtCu (300-1h), 50 nm for PtCu (300-1h/70:30) and 20 nm PtCu (300-1h/30:70).

5.2.3. SEM-EDS Results

The data obtained from the SEM-EDS results for monometallic Pt (300-1h/50:50), Cu (300-1h/50:50) and bimetallic PtCu (300-1h), PtCu (300-1h/30:70) and PtCu (300-1h/70:30) are summarized in Table 5.4.

Table 5.4: Results of weight and atomic values of synthesized catalysts calculated according to SEM-EDS result.

Sample Codes	**C (K)**		**Pt (L)**		**Cu (K)**		**Atomic Ratio**
	Weight %	Atomic %	Weight %	Atomic %	Weight %	Atomic %	
Pt (300-1h/50:50)	67.70	97.15	32.30	2.85	-	-	Pt/CB:GNP (50:50)
Cu (300-1h/50:50)	74.01	93.78	-	-	25.99	6.22	Cu/CB:GNP (50:50)
PtCu (300-1h)	83.66	98.28	12.74	0.98	3.60	0.80	$Pt_{55}Cu_{45}$/CB:GNP (50:50)
PtCu (300-1h/30:70)	79.19	97.20	12.95	0.98	7.86	1.82	$Pt_{35}Cu_{65}$/CB:GNP (30:70)
PtCu (300-1h/70:30)	83.38	98.26	13.06	0.95	3.55	0.79	$Pt_{55}Cu_{45}$/CB:GNP (70:30)

According to SEM-EDS results, atomic ratios for bimetallic PtCu (300-1h), PtCu (300-1h/30:70) and PtCu (300-1h/70:30) were calculated $Pt_{55}Cu_{45}$/CB:GNP (50:50), $Pt_{35}Cu_{65}$/CB:GNP (30:70) and $Pt_{55}Cu_{45}$/CB:GNP (70:30) respectively. Based on these results, the PtCu (300-1h/30:70) sample has the lowest atomically amount of platinum among these three catalysts. In addition, PtCu (300-1h) and PtCu (300-1h/70:30) catalysts were found to have the same atomic composition according to these results.

With respect to the EDS results, the mapping images for the PtCu (300-1h), PtCu (300-1h/30:70) and PtCu (300-1h/70:30) specimens are served in Figure 5.3. In the images, the blue, yellow and red colors represent carbon, platinum, and copper elements, respectively. When the images are examined, it is seen that the carbon element is dominant for all three catalysts.

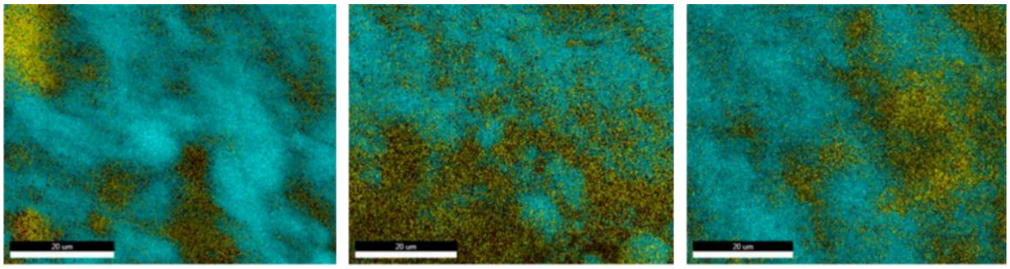

(a) (b) (c)

Figure 5.3: SEM-EDS mapping images of (a) PtCu (300-1h), (b) PtCu (300-1h/30:70) and (c) PtCu (300-1h/70:30) speciments as catalysts.

5.2.4. XRD Analysis

The XRD analysis technique was used to identify the crystal structure phases of the NPs. The XRD patterns of the monometallic Pt (300-1h/50:50) and Cu (300-1h/50:50) catalysts is shown in Figure 5.4 with the bimetallic PtCu (300-1h). Among the three catalysts, the C (002) peak appeared at near $2\theta = 26$ degree. For monometallic Pt(300-1h/50:50), diffraction peaks at 39.76^0, 46.34^0, 67.56^0 and 81.42^0 angles which belong to (111), (200), (220) and (311) layers of fcc Pt structure. For monometallic Cu (300-1h/50:50), diffraction peaks at 43.24^0, 50.36^0 and 74.08^0 angles which represent to (111), (200) and (220) layers of fcc Cu structure. The Pt (111) layer known as the most electrocatalytically active surface of platinum, is positioned at $2\theta=41.42^0$ for PtCu (300-1h) catalyst, which is 1.66 degrees greater than the Pt (111) peak of monometallic Pt (300-1h/50:50) NPs. The appearance of the Pt (111) surface peak in the larger 2θ degree in the bimetallic NPs is a proof for the formation of alloy bimetallic PtCu at nano-scale. Moreover, the XRD peaks for the bimetallic PtCu (300-1h) are broader than the peaks of the monometallic Pt (300-1h/50:50) and Cu (300-1h/50:50) catalysts. This fact confirms the particle size of PtCu (300-1h) is smaller than monometallic Pt and Cu particle size as previously appearing in the TEM images (Figure 5.1 and Figure 5.2).

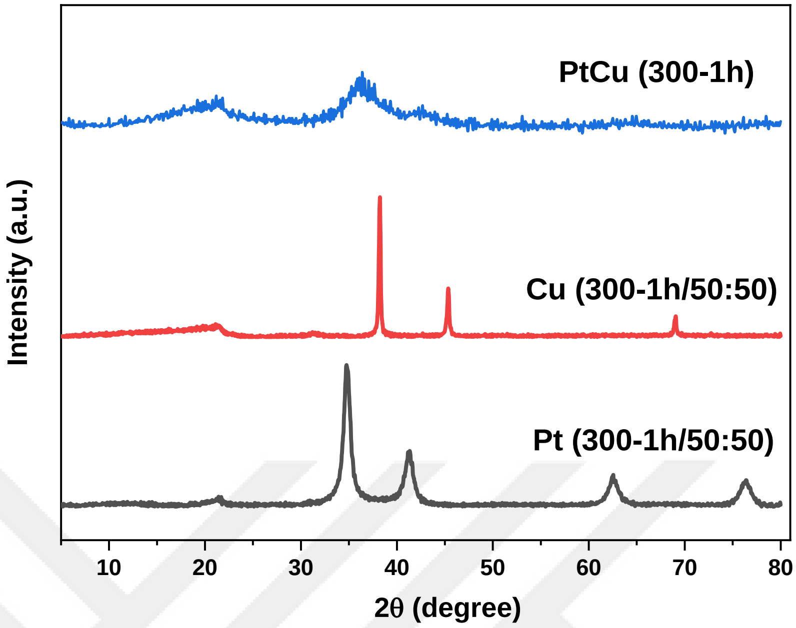

Figure 5.4: XRD patterns of monometallic Pt (300-1h/50:50), Cu (300-1h/50:50) and bimetallic PtCu (300-1h).

XRD spectra for PtCu (300-1h), PtCu (300-1h/30:70) and PtCu (300-1h/70:30) catalysts are given in Figure 5.5. The broad XRD peak observed at about 26^0 in all three catalysts, belongs to the C (002) layer due to the hybrid support having graphitic structure. The Pt peaks at near 41^0, 47^0, 70^0 and 84^0 which indicated to the (111), (200), (220) and (311) plane of fcc structure of Pt. These peaks demonstrated that crystallised Pt nanoclusters were produced on the supports with various surface orientations. On the other hand, when the position of these peaks in the bimetallic structure is compared with the monometallic Pt, it is understood that all of them without exception are formed at greater 2θ than the monometallic Pt (300-1h/50:50) structure. The reason for this situation is that the formation of the alloy bimetallic nano scale PtCu structure with the synergistic effect of Pt and Cu elements.

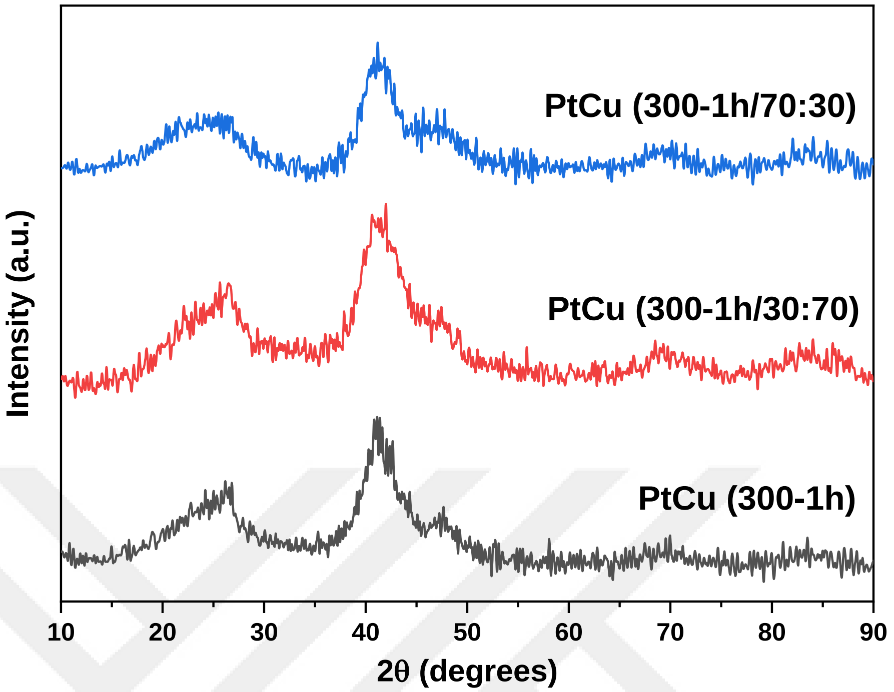

Figure 5.5: XRD patterns of bimetallic PtCu (300-1h), PtCu (300-1h/30:70) and PtCu (300-1h/70:30).

5.2.5. Raman Analysis

The Raman spectra of hybrid carbon support; CB:GNP (50:50), CB:GNP (30:70) and GB:GNP (70:30) are presented in Figure 5.6.

The D band about 1346 cm^{-1} indicates the structure's disorder and demonstrating the sp^3 hybridization. Otherwise, the G band at near 1600 cm^{-1} signaling the existing of the sp^2 hybridized carbon atoms in the hexagonal framework. The intensity ratios of these two bands (I_D/I_G) give strong information about the disorderness and defects of the material [157-158]. In addition to these two bands, another important peak that occurs at about 2700 cm^{-1} is called the 2D band. In addition to these two bands, another important peak that occurs at ~2700 cm^{-1} is the 2D band. In addition, as mentioned before, the ratio of I_{2D}/I_G ~2–3, 2> I_{2D}/I_G> 1 and I_{2D}/I_G <1 indicate to monolayer graphene, bilayer graphene and multilayer one, respectively.

Interestingly, although there is GNP in all three hybrid carbon structures, the 2D band is only apparent for the CB:GNP (50:50) hybrid carbon support. Among these hybrid carbon supports, CB:GNP (70:30) support exhibits the highest disorderness according to their I_D/I_G ratio (Table 5.5). This result can be interpreted as CB:GNP (70:30) carbon support contains more defects and therefore creates a suitable environment for the nanoparticles to be more easily attached to the support. When the numerical values in Table 5.5 are examined, it is understood that the I_{2D}/I_G ratio for CB:GNP (50:50) hybrid carbon support is 0.82, so it contains multilayer graphene. Considering the superior physical and chemical properties of graphene, this may provide an electrochemically advantage for the CB:GNP (50:50) support material.

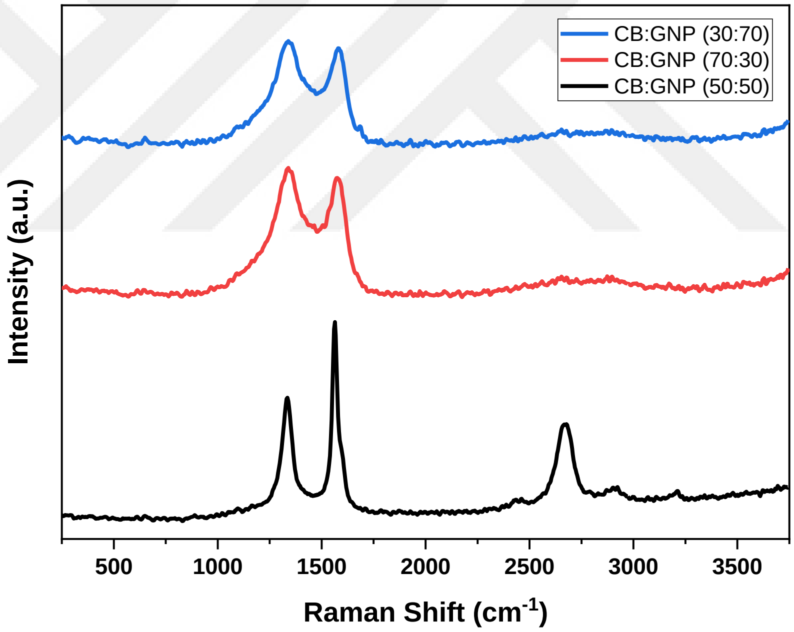

Figure 5.6: Raman spectra of CB:GNP (50:50), CB:GNP (70:30) and CB:GNP (30:70).

Table 5.5: Calculated I_D/I_G and I_{2D}/I_G ratios for hybrid carbon supports.

Sample Codes	**I_D/I_G and I_{2D}/I_G Ratios**	
	I_D/I_G	**I_{2D}/I_G**
CB:GNP (50:50)	0.87	0.82
CB:GNP (30:70)	1.01	0.00
CB:GNP (70:30)	1.02	0.00

The raman results for monometallic Pt (300-1h/50:50) and Cu (300-1h/50:50) are shared in Figure 5.7. D, G and 2D bands are available in both catalyst structures. The D, G and 2D bands are shown at 1339, 1579 and 2681 cm^{-1} and at 1343, 1575 and 2677 cm^{-1} for Pt (300-1h/50:50) and Cu (300-1h/50:50) speciment, respectively. The I_D/ I_G and I_{2D}/I_G ratios for Pt (300-1h/50:50) and Cu (300-1h/50:50) catalysts are demonstrated in Table 5.6. Based on the I_D/I_G ratio, it is seen that the defects in monometallic Pt (300-1h/50:50) catalyst are higher than in monometalic Cu (300-1h/50:50). In addition, hybrid CB:GNP (50:50) supports were used in both samples, its disorderness increased with the respect of I_D/I_G ratio of both catalysts after catalysts sythesized process.

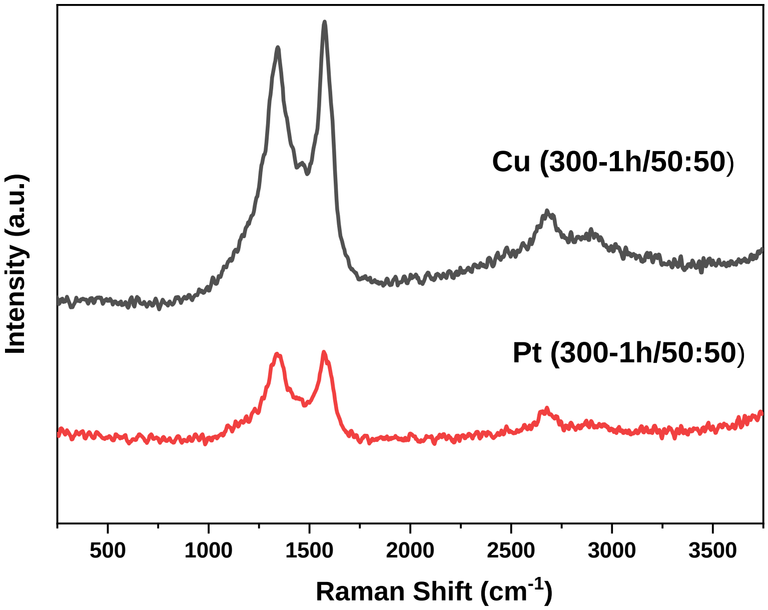

Figure 5.7: Raman spectra of Pt (300-1h/50:50) and Cu (300-1h/50:50).

Table 5.6: Calculated I_D/I_G and I_{2D}/I_G ratios for monometallic Pt (300-1h/50:50) and Cu (300-1h/50:50) catalysts.

Sample Codes	**I_D/I_G and I_{2D}/I_G Ratios**	
	I_D/I_G	**I_{2D}/I_G**
Pt (300-1h/50:50)	1.00	0.94
Cu (300-1h/50:50)	0.98	0.84

The Raman spectra of PtCu (300-1h), PtCu (300-1h/30:70) and PtCu (300-1h/70:30) catalysts are given in Figure 5.8. Interestingly, in the PtCu (300-1h/30:70) catalyst prepared with the CB:GNP (30:70) carbon support, the 2D band appeared in the catalyst structure, although it was not visible in the raman spectra of CB:GNP (30:70) carbon support. At this point, it is thought that the synthesis conditions of the bimetallic PtCu (300-1h/30:70) NPs contribute to the visibility of the 2D band in the structure. Although it has the same synthesis conditions as PtCu (300-1h) and PtCu (300-1h/30:70), the 2D band does not appear for PtCu (300-1h/70:30) due to most likely the low GNP ratio in the carbon support. The I_D/I_G and I_{2D}/I_G ratios for PtCu (300-1h), PtCu (300-1h/30:70) and PtCu (300-1h/70:30) catalysts are given in Table 5.7. According to these results, it is understood that PtCu (300-1h/70:30) catalyst has the highest value in both I_D/I_G and I_{2D}/I_G ratio. At this point, it appears that as the CB ratio increases in the hybrid carbon support composition, it promete the disorderliness in the catalyst structure. Although this allows the successful interaction between NPs and carbon support surface, still, lower electronic properties of CB compared to GNP can be an obstable in the electrocatalytic activity which needs to be checked by electrochemical methods.

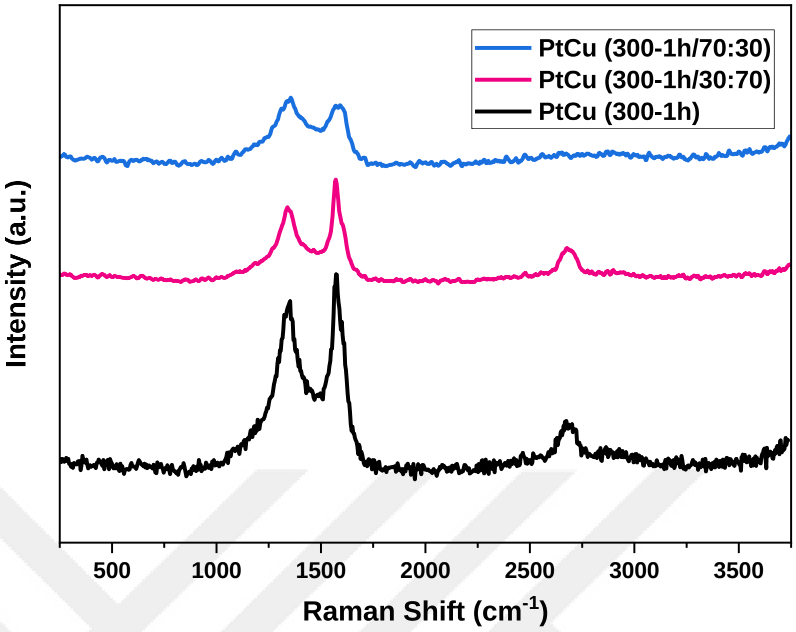

Figure 5.8: Raman spectra of PtCu (300-1h), PtCu (300-1h/30:70) and PtCu (300-1h/70:30).

Table 5.7: Calculated I_D/I_G and I_{2D} / I_G ratios for bimetallic PtCu (300-1h), PtCu (300-1h/30:70) and PtCu (300-1h/70:30) catalysts.

Sample Codes	**I_D/I_G and I_{2D}/I_G Ratios**	
	I_D/I_G	**I_{2D}/I_G**
PtCu (300-1h)	0.95	0.74
PtCu (300-1h/30:70)	0.93	0.84
PtCu (300-1h/70:30)	1.01	0

5.2.6. Cyclic Voltammetry (CV) Results

In this section, for Pt (300-1h/50:50), Cu (300-1h/50:50), PtCu (300-1h), PtCu (300-1h/30:70), PtCu (300-1h/70:30) and commercial 20% Pt on Vulca XC-72 catalysts, CV measurements were taken with Metrohm DropSens potentiostat. Glassy carbon electrode, platinum wire and Ag/AgCl were used as WE, CE and RE, respectively. 0.1 M $HClO_4$ was preferred as the electrolyte solution and was purged with argon both before and during the CV test. The catalyst ink for CV was prepared in the same way as the catalyst ink prepared previously for bimetallic structures and these inks were applied on the working electrode under the same conditions. All samples had 25 μg Pt loading on the electrode surface. For each catalyst, the device is first conditioned by 50 cycles at scan rate of 0,1 V/s. Subsequently, 5 cycles were taken at 0.05 V/s for all catalysts and the 3rd cycle from these cycles was used for ECSA calculations. In all CV cycles, the initial potential and the highest potential was set up at -0.2 V and 1.2 V, respectively.

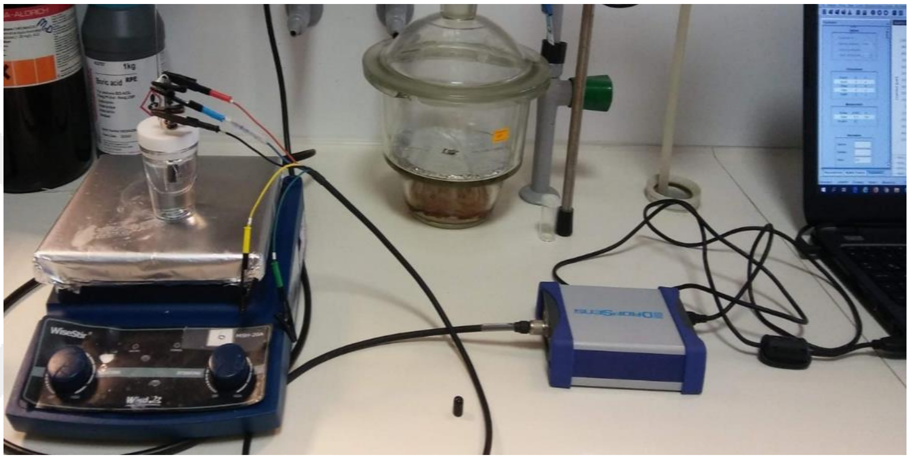

Figure 5.9: CV experimental set up.

Figure 5.10 shows the CV voltagram of monometallic Pt (300-1h/50:50) and Cu (300-1h/50:50) catalysts compared to commercial 20% Pt on Vulcan XC-72 catalyst. The ECSA values were calculated as 16.5, 3.0 and 42 m^2/g_{Pt} for ZA-14: Pt (300-1h/50:50), ZA-15: Cu (300-1h/50:50) and commercial 20% Pt on Vulcan XC-72, respectively. The CV results of both monometallic catalysts were considerably lower than the commercial Pt catalyst. These results also indicate that in particular the monometallic Cu (300-1h/50:50) catalyst shows almost no electrochemical activity. As a result, although preferred synthesis method is effective for forming monometallic Pt and Cu NPs on the hybrid CB:GNP (50:50) support, it is not suitable for synthesizing electrochemically active monometallic catalysts.

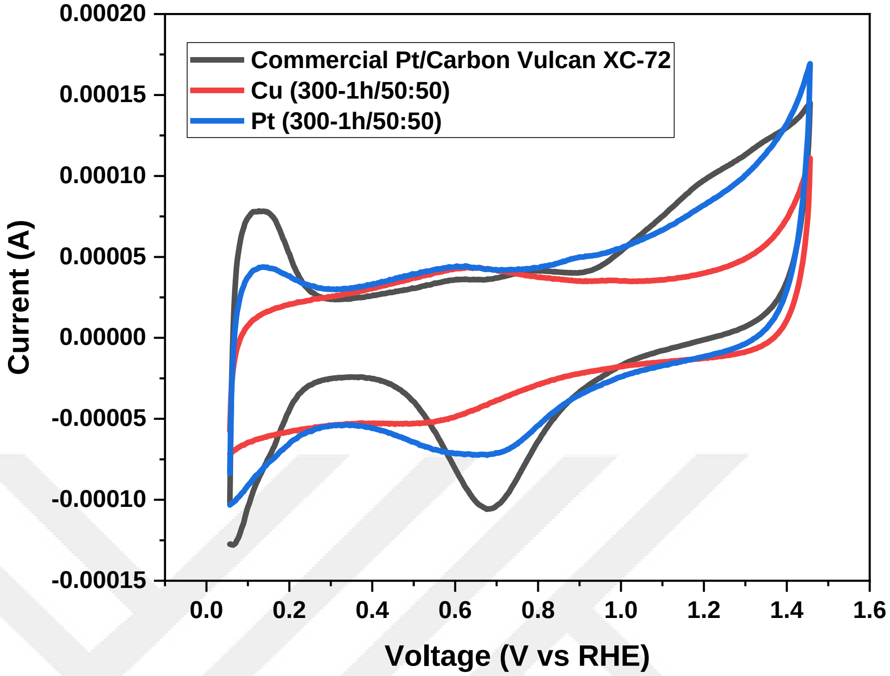

Figure 5.10: Cyclic voltammetry results of Pt (300-1h/50:50), Cu (300-1h/50:50) and commercial 20% Pt on Vulcan XC-72.

Figure 5.11 shows the CV voltagram of bimetallic PtCu (300-1h), PtCu (300-1h/30:70) and PtCu (300-1h/70:30) catalysts compared to commercial 20% Pt on Vulcan XC-72. The ECSA values were calculated as 85, 70, 63 and 42 m^2/g_{Pt} for PtCu (300-1h), PtCu (300-1h/30:70) and PtCu (300-1h/70:30) and commercial 20% Pt on Vulcan XC-72, respectively. The ECSA value of all three bimetallic catalysts was higher than commercial 20% Pt on Vulcan XC-72 catalysts. PtCu (300-1h) hybrid material had the highest ECSA value. However, interestingly, the ECSA value of the re-synthesized PtCu (300-1h) catalyst in this section was lower than the ECSA value found in the previous section. This may be because the potentiostat brands used when conducting CV experiments are different. But in any case, according to ECSA values, PtCu (300-1h) catalyst is two times electrochemically active compared to commercial Pt catalyst.

One of the most important goals of this thesis was to reduce the cost of catalysts, which is one of the biggest obstacles to the commercialization of PEM fuel cells. For this, unlike monometallic Pt catalysts, which are frequently used as commercial catalysts in the market, Cu is included in the catalyst structure as a secondary element, which is more cost-effective than Pt. According to the ICP-MS result, the re-synthesized PtCu (300-1h) catalyst contains 15% wt Pt. In this regard, the catalyst PtCu (300-1h) is superior to the commercial %20 wt Pt on Carbon Vulcan XC-72 not only electrochemically but also in terms of cost.

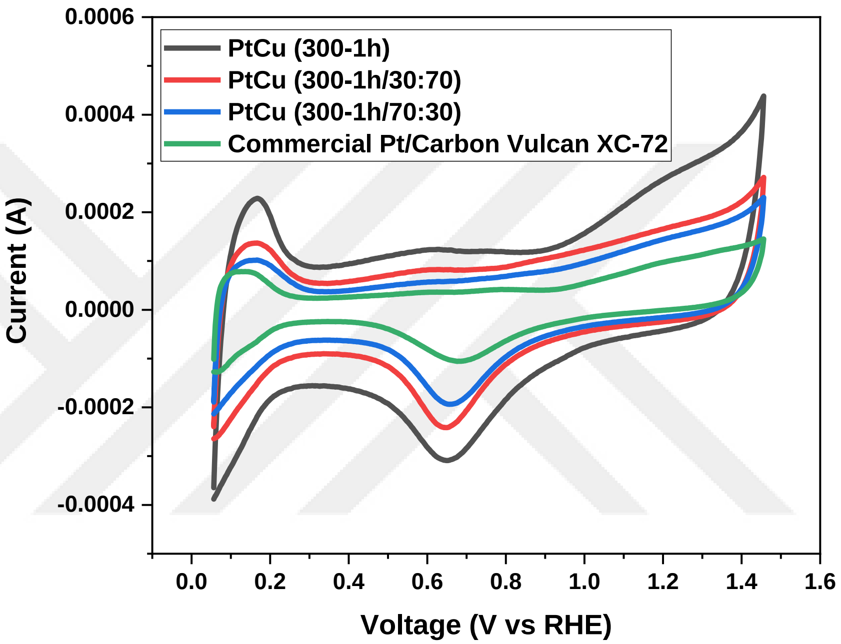

Figure 5.11: Cyclic voltammetry results of PtCu (300-1h), PtCu (300-1h/30:70), PtCu (300-1h/70:30) and commercial 20 % Pt on Vulcan XC-72.

Table 5.8: Particle size and ECSA values of of PtCu (300-1h), PtCu (300-1h/30:70), PtCu (300-1h/70:30) and commercial 20 % Pt on Vulcan XC-72.

Catalyst Types	**Particle Size**	**ECSA (m^2/g_{Pt})**
PtCu (300-1h)	4.8 ± 1.5	85
PtCu (300-1h/30:70)	6.3 ± 1.9	70
PtCu (300-1h/70:30)	5.4 ± 1.6	63
Commercial 20 % wt Pt on Carbon Vulcan XC-72	——	42

When the data in Table 5.8 are examined, it is understood, there is no direct relationship between particle size and ECSA value. Although PtCu (300-1h) with the highest ECSA value has a smaller particle size than the other two catalysts, the same is not true for PtCu (300-1h/70:30).

One of the most important conclusions to be drawn from these results is that although the carbon support ratios are the same, the bimetallic PtCu (300-1h) catalyst has the highest ECSA value, but the ECSA values of monometallic catalysts are lower than the commercial Pt catalysts. This situation can be explained by the fact that Pt and Cu elements come together as alloys to form the nano PtCu structure and display a synergistic effect in catalytic terms.

After a series of structural characterization processes, it is recognized that CB: GNP (50:50), CB: GNP (70:30) and CB: GNP (30:70) hybrid carbon ratios each have advantages and disadvantages. However, as a final product, these hybrid carbon supports are designed to be used in electrocatalysts, and it has been proved with this thesis for bimetallic PtCu nanocatalysts the optimal carbon support ratio should be CB: GNP (50:50) to achieve electrochemically more active NPs.

There is no study in the literature on the electrochemical properties of CB:GNP hybrid carbon supported bimetallic PtCu NPs. However, two studies in the literature on monometallic Pt/CB:GNP electrocatalysts are noteworthy. The first of these belongs to Ece Arıcı and her co-workers. In this study, by using the Pt (dba) (dba: dibenzylideneacetone) complex as the Pt precursor, the researchers synthesized three forms of catalysts supported by CB, GNP and CB: GNP (50:50), using the method of organometallic synthesis. In the elemental analysis by ICP-MS, the amount of Pt for all three catalysts is reported as 21% (wt.). The ECSA values were calculated as 10, 19 and 55 m^2/g_{Pt} for Pt/CB, Pt/GNP, and Pt/CB-GNP NPs, respectively. The ORR and PEM fuel cell results are in parallel with the ECSA values, proving that the CB:GNP (50:50) supported monometallic Pt catalyst gives the best result electrochemically [20].

Another study on CB:GNP hybrid support belongs to Elif Daş and her co-workers. In this study, monometallic Pt NPs was synthesized for PEM fuel cells by using CB and GNP supports at different ratios. Supercritical carbon dioxide deposition was used to design Pt NPs on a carbon support. Seven different Pt NPs were prepared as Pt/GNP:CB

(0:100), Pt/GNP:CB (90:10), Pt/GNP:CB (80:20), Pt/GNP:CB (70:30), Pt/GNP:CB (60:40), Pt/GNP:CB (50:50), Pt/GNP:CB (0:100). According to results, Pt/GNP:CB (80:20) catalysts exhibited higher ECSA compared to the other catalysts and its ECSA values calculated as 52.24 m^2 /g_{Pt}. According to TGA results Pt / GNP:CB (80:20) catalyst contains 21 % Pt (wt). Although Pt/GNP:CB (80:20) has the highest ECSA value, Pt /GNP:CB (60:40) was the most durable catalyst according to the corrosion test. Not only did the Pt /GNP:CB (60:40) catalyst show the highest corrosion resistance among other hybrid catalysts with the lowest ECSA losses (%), and yet it also exhibited the highest performance of PEM fuel cell [18].

Many research efforts have been dedicated to exploring new catalyst support materials in the literature in order to improve the efficiency of fuel cells. In this thesis study, electrochemically optimum hybrid CB:GNP ratio was studied for bimetallic PtCu NPs for the first time in the literature. According to our strategy, not only will hybridization of GNPs with CB avoid the accumulation of these carbon materials, but the synergistic effects between them can also be completely exploited. With this study, the synthesis of CB:GNP supported bimetallic PtCu NPs have been successfully achieved. For all three catalysts; PtCu/CB:GNP (50:50), PtCu/CB:GNP (30:70) and PtCu/CB:GNP (70:30), the ECSA value is higher than the monometallic Pt NPs synthesized in the studies mentioned above with much lower Pt amount.

6. CONCLUSION and the FUTURE WORK

The objective of this study is to determine the impact of synthesis conditions on the formation of bimetallic PtCu NPs and then, by using the most suitable synthetic route, identify the optimum hybrid (CB: GNP) carbon support ratio for the most electrochemially active bimetallic PtCu NPs as a potential electrocatalyst towards PEM fuel cells. For this purpose, in the first experimental section, five different CB:GNP (50:50) supported bimetallic PtCu NPs were synthesized from the metal precursors, Pt(acac)$_2$ and Cu(acac)$_2$, at different reaction temperature, time and process by using mainly organometallic and thermal decomposition synthesis methods. The structural characterization of these five samples, namely, PtCu (120-2h), PtCu (300-1h), PtCu (300-4h), PtCu (300-1h/70-24h) and PtCu (70-24h) were fully characterized with TGA, FT-IR, XRD, XPS, TEM, SEM-EDS and Raman. In addition, ICP-MS analysis was performed to determine the metal ratio Pt:Cu in these NPs.

According to the TEM results, it was observed that these five different synthesis conditions applied achievd the bimetallic nature of PtCu NPs on the hybrid carbon CB:GNP (50:50) support. No agglomeration of NPs were observed in any of these produced nanostructues. Although a variety of characterization methods revealed the presence of both Pt and Cu metal on the PtCu (70-24h) NP structure, one could not observe the particles according to the TEM analysis. This was attributed to the weak resolution of TEM as the nanoparticles formed were most likely <2 nm. Investigation of the PtCu (70-24h) NPs with HRTEM will be a future work.

On the other hand, although all synthesis conditions are suitable for NP formation, especially according to XRD and FT-IR results, metal precursors Pt (acac)$_2$ and Cu (acac)$_2$ are not convenient for organometallic synthesis method. Unlike the thermal decomposition method, in the organometallic synthesis, which is applied at mild temperatures and presence of H_2 gas, the organic pieces of the metal precursors are not completely extracted from the catalyst structure after synthesis and generate undesirable attachments on the carbon support and/or nanoparticles.

According to the electrochemical characterizations, The ECSA values of PtCu (300-1h) bimetallic catalysts synthesized under dynamic varigon gas at 300 ^{0}C for 1 hour by thermal decomposition were higher than the other four synthesized catalysts and commercial 20% wt. Pt on carbon Vulcan XC-72. ECSA values of both catalysts; PtCu (300-1h) and PtCu (300-4h) synthesized by thermal decomposition method were found better than commercial Pt catalysts. On the contrary, according to ECSA values, the electrochemical efficiency of PtCu (120-2h), PtCu (300-1h/70-24h) and PtCu (70-24) catalysts synthesized using the organometallic synthesis remained below the commercial Pt catalyst performance.

With respect to all these structural and electrochemical results, it was determined that the PtCu (300-1h) catalyst obtained at the end of the thermal decomposition reaction that for 1 hour at 300 ^{0}C under dynamic varigon gas as a synthesis method had the most electrochemically active performance. Therefore, in the second part of the thesis, NPs were synthesized under dynamic varigone gas at 300 ^{0}C for 1 hour to examine the effect of carbon support ratios on the formation of bimetallic PtCu NPs and their electrochemical performance.

In the second part of the thesis, although the main purpose is to investigate the effect of changing carbon support ratios on the performance of bimetallic PtCu electrocatalysts, the monometallic Pt (300-1h/50:50) and Cu (300-1h/50:50) catalysts were also prepared by thermal decomposition to recognize the synergic effect of bimetallic nanostructures and their excellent electrochemical behaviours comparison with monometallic nanostructures. Besides the mentioned monometalic structures; including PtCu (300-1h), PtCu (300-1h/30:70) and PtCu (300-1h/70:30) three different catalysts were also synthesized with varying carbon support ratios. Structural characterizations of all synthesized monometallic and bimetallic nanocatalysts were made by XRD, BET, TEM, SEM-EDS, and Raman. Moreover, ICP-MS analysis was carried to evaluate the metal ratio in the synthesized catalysts.

According to TEM images, in monometallic structures, the particle size is larger than the bimetallic PtCu (300-1h) structure, even if the monometallic catalysts have the same synthesis conditions and the same carbon support ratio as the bimetallic catalyst. When the ECSA values of the relevant catalysts were examined, it was understood the bimetallic PtCu (300-1h) catalyst was electrochemically superior to the monometallic structures. This results confirm that the idea of nanoscale bimetallic structures have been displayed to be special in terms of improved features relative to their metallic counterparts. In addition, XRD results show that monometallic structures are formed as sharp peaks. Contrary to this situation, the XRD peaks in the bimetallic structure are broad and the peak positions shift to a higher 2θ values. These XRD results indicate the alloyed bimetallic PtCu particles are formed at the nanoscale.

With respect to TEM images, the smallest bimetallic PtCu nano structures as particle size were observed in CB:GNP (50:50) supported PtCu (300-1h) bimetallic catalysts when the ratio of carbon support changes. According to the results of the BET analysis, although CB:GNP (30:70) carbon support has the highest values of the total surface area and total pore volume, CB:GNP (30:70) supported bimetallic PtCu (300-1h/30:70) catalysts has the larger particle size than both PtCu (300-1h) and PtCu (300-1h/70:30) catalysts based on TEM images. The XRD results show that the Pt (111) surface, known as the most catalytically active surface of platinum, was formed in all these three bimetallic NPs.

The ECSA values of PtCu (300-1h), PtCu (300-1h/30:70) and PtCu (300-1h/70:30) catalysts, were higher than the commercial 20% wt. Pt on carbon Vulcan XC-72. When the ECSA values of these four catalysts are compared, the result is that: PtCu (300-1h) (85 m^2/g_{Pt}) > PtCu (300-1h/30:70) (70 m^2/g_{Pt}) > PtCu (300-1h/70:30) (63 m^2/g_{Pt}) > commercial Pt (42 m^2/g_{Pt}) catalyts. In summary, it has been proven after series of studies that electrochemically the most active hybrid carbon ratio is CB:GNP (50:50) for bimetallic PtCu electrocatalysts.

To sum up, with this thesis study, among the nine different catalysts synthesized, four of them, PtCu (300-1h) (99 m^2/g_{Pt} and 85 m^2/g_{Pt}), PtCu (300-4h) (52 m^2/g_{Pt}), PtCu (300-1h/30:70) (70 m^2/g_{Pt}) and PtCu (300-1h/70:30) (63 m^2/g_{Pt}), showed higher ECSA values than that of commercial Pt. According to our results PtCu (300-1h) NPs was the most promising one to be used as a cathode electrocatalyst towards PEM fuel cells. We believe that hybrid carbon supported bimetallic structures will prevent corrosion and increase the durability of the electrocatalyst. Our future efforts will be towards the study of ORR mechanism and PEM fuel cell performances of this type of PtCu nanostructures.

REFERENCES

[1] Armaroli, N., Balzani, V., (2007), "The Future of Energy Supply: Challenges and Opportunities", Angew. Chemie - Int. Ed., 46 (1–2), 52–66.

[2] Steele, B.C.H., Heinzel, A., (2001), "Materials for Fuel-cell Technologies", Nature, 414 (6861), 345–352.

[3] Cheng, X., Shi, Z., Glass, N., Zhang, L., Zhang, J., Song, D., Liu, Z.S., Wang, H., Shen. J., (2007), "A Review of PEM Hydrogen Fuel Cell Contamination: Impacts, Mechanisms, and Mitigation", J. Power Sources, 165 (2), 739–756.

[4] Gasteiger, H.A., Kocha, S.S., Sompalli, B., Wagner, F.T., (2005), "Activity Benchmarks and Requirements for Pt, Pt-Alloy, and Non-Pt Oxygen Reduction Catalysts for PEMFCs", Appl. Catal. B Environ., 56 (1-2 SPEC. ISS.), 9–35.

[5] Acres, G.J.K., Hards, G.A., (1996), "Electrocatalysts for Fuel Cells", Philos. Trans. R. Soc. A Math. Phys. Eng. Sci., 354 (1712), 1671–1680.

[6] Zhang, J., (2011), "Recent Advances in Cathode Electrocatalysts for PEM Fuel Cells", Front. Energy, 5 (2), 137–148.

[7] Stamenkovic, V.R., Mun, B.S., Mayrhofer, K.J.J., Ross, P.N., Markovic, N.M., (2006), "Effect of Surface Composition on Electronic Structure, Stability, and Electrocatalytic Properties of Pt-Transition Metal Alloys: Pt-Skin Versus Pt-Skeleton Surfaces", J. Am. Chem. Soc., 128 (27), 8813–8819.

[8] Dhand, C., Dwivedi, N., Loh, X.J., Jie Ying, A.N., Verma, N.K., Beuerman, R.W., Lakshminarayanan, R., Ramakrishna, S., (2015), "Methods and Strategies for the Synthesis of Diverse Nanoparticles and Their Applications: A Comprehensive Overview", RSC Adv., 5 (127), 105003–105037.

[9] Amiens, C., Chaudret, B., Ciuculescu-Pradines, D., Collière, V., Fajerwerg, K., Fau, F., Kahn, M., Maisonnat, A., Soulantica, K., Phillippot, K., (2013), "Organometallic Approach for the Synthesis of Nanostructures", New J. Chem., 37 (11), 3374–3401.

[10] Chandran, P., Ghosh, A., Ramaprabhu, S., (2018), "High-Performance Platinum-Free Oxygen Reduction Reaction and Hydrogen Oxidation Reaction Catalyst in Polymer Electrolyte Membrane Fuel Cell", Sci. Rep., 8 (1), 3591.

[11] Yu, P.T., Gu, W., Zhang, J., Makharia, R., Wagner, F.T., Hubert, A., (2009), "Carbon-Support Requirements for Highly Durable Fuel Cell Operation BT - Polymer Electrolyte Fuel Cell Durability", Springer New York, pp. 29–53.

[12] Seselj, N., Engelbrekt, C., Zhang, J., (2015), "Graphene-Supported Platinum

Catalysts for Fuel Cells", Sci. Bull., 60 (9), 864–876.

[13] Maass, S., Finsterwalder, F., Frank, G., Hartmann, R., Merten, C., (2008), "Carbon Support Oxidation in PEM Fuel Cell Cathodes", J. Power Sources, 176 (2), 444–451.

[14] Fang, B., Chaudhari, N.K., Kim, M.-S., Kim, J.H., Yu, J.-S., (2009), "Homogeneous Deposition of Platinum Nanoparticles on Carbon Black for Proton Exchange Membrane Fuel Cell", J. Am. Chem. Soc., 131 (42), 15330–15338.

[15] Mukherjee, S., Bates, A., Lee, S.C., Lee, D.-H., Park, S., (2014), "A Review of Application of CNTs in PEM Fuel Cells", Int. J. Green Energy, 12 (8), 140121063707006.

[16] Chan, S., Jankovic, J., Susac, D., Saha, M., Tam, M., Yang, H., Ko, F., (2018), "Electrospun Carbon Nanofiber Catalyst Layers for Polymer Electrolyte Membrane Fuel Cells: Fabrication and Optimization", J. Mater. Sci., 53, 11633–11647.

[17] Viva, F., Bruno, M., Franceschini, E., Thomas, Y., Ramos-Sanchez, G., Feria, O.S., Corti, H.R., (2014), "Mesoporous Carbon as Pt Support for PEM Fuel Cell", Int. J. Hydrogen Energy, 39, 8821-8826.

[18] Daş, E., Kaplan, B.Y., Gürsel, S.A., Yurtcan, A.B., (2019), "Graphene Nanoplatelets-Carbon Black Hybrids as an Efficient Catalyst Support for Pt Nanoparticles for Polymer Electrolyte Membrane Fuel Cells", Renew. Energy, 139 1099–1110.

[19] Shao, Y., Liu, J., Wang, Y., Lin, Y., (2009), "Novel Catalyst Support Materials for PEM Fuel Cells: Current Status and Future Prospects", J. Mater. Chem., 19 (1), 46–59.

[20] Arici, E., Kaplan, B.Y., Mert, A.M., Alkan Gursel, S., Kinayyigit, S., (2019), "An Effective Electrocatalyst Based on Platinum Nanoparticles Supported with Graphene Nanoplatelets and Carbon Black Hybrid for PEM Fuel Cells", Int. J. Hydrogen Energy, 44 (27), 14175–14183.

[21] Laurent, S., Forge, D., Port, M., Roch, A., Robic, C., Elst, L.V., Muller, R.N., (2008), "Magnetic Iron Oxide Nanoparticles: Synthesis, Stabilization, Vectorization, Physicochemical Characterizations and Biological Applications", Chem. Rev., 108 (6), 2064–2110.

[22] Aiken, J.D., Finke, R.G., (1999), "A Review of Modern Transition-Metal Nanoclusters: Their Synthesis, Characterization, and Applications in Catalysis", J. Mol. Catal. A Chem., 145 (1), 1–44.

[23] McCaffrey, R., Long, H., Jin, Y., Sanders, A., Park, W., Zhang, W., (2014), "Template Synthesis of Gold Nanoparticles with an Organic Molecular Cage", J. Am. Chem. Soc., 136 (5), 1782–1785.

[24] Schmid, G., (1998), "Large Metal Clusters and Colloids - Metals in the Embryonic State", Prog. Colloid Polym. Sci., 111, 52–57.

[25] Roduner, E., (2006), "Size Matters: Why Nanomaterials are Different", Chem. Soc. Rev., 35 (7), 583–592.

[26] Finney, E.E., Finke, R.G., (2008), "Nanocluster Nucleation and Growth Kinetic and Mechanistic Studies: A Review Emphasizing Transition-Metal Nanoclusters", J. Colloid Interface Sci., 317 (2), 351–374.

[27] Schmid, G.D., (2008), "General Features of Metal Nanoparticles Physics and Chemistry", Met. Nanoclusters Catal. Mater. Sci. Issue Size Control, 3–20.

[28] Thanh, N.T.K., Maclean, N., Mahiddine, S., (2014), "Mechanisms of Nucleation and Growth of Nanoparticles in Solution", Chem. Rev., 114 (15), 7610–7630.

[29] Hornstein, B.J., Finke, R.G., (2004), "Transition-Metal Nanocluster Kinetic and Mechanistic Studies Emphasizing Nanocluster Agglomeration: Demonstration of a Kinetic Method that Allows Monitoring of All Three Phases of Nanocluster Formation and Aging", Chem. Mater., 16 (1), 139–150.

[30] Thanh, N.T.K., Maclean, N., Mahiddine, S., (2014), "Mechanisms of Nucleation and Growth of Nanoparticles in Solution", Chem. Rev., 114 (15), 7610–7630.

[31] Jun, Y.S., Kim, D., Neil, C.W., (2016), "Heterogeneous Nucleation and Growth of Nanoparticles at Environmental Interfaces", Acc. Chem. Res., 49 (9), 1681–1690.

[32] Alloyeau, D., Ricolleau, C., Mottet, C., Oikawa, T., Langlois, C., Bouar, T.L., Braidy, N., Loiseau, A., (2009), "Size and Shape Effects on the Order–Disorder Phase Transition in Copt Nanoparticles", Nat. Mater., 8 (12), 940–946.

[33] Wu, Z., Yang, S., Wu, W., (2016), "Shape Control of Inorganic Nanoparticles from Solution", Nanoscale, 8 (3), 1237–1259.

[34] Iravani, S., (2011), "Green Synthesis of Metal Nanoparticles Using Plants", Green Chem., 13 (10), 2638–2650.

[35] Biswas, A., Bayer, I.S., Biris, A.S., Wang, T., Dervishi, E., Faupel, F., (2012), "Advances in Top-Down and Bottom-Up Surface Nanofabrication: Techniques, Applications & Future Prospects", Adv. Colloid Interface Sci., 170 (1–2), 2–27.

[36] Gerberich, W.W., Jungk, J.M., Mook, W.M., (2003), "The Bottom-Up Approach to Materials by Design", Elsevier Science Ltd, Oxford, 211–220.

[37] Choy, K.L., (2003), "Chemical Vapour Deposition of Coatings", Prog. Mater. Sci., 48 (2), 57–170.

[38] Yu, J., Li, J., Zhang, W., Chang, H., (2015), "Synthesis of High Quality Two-Dimensional Materials via Chemical Vapor Deposition", Chem. Sci., 6 (12), 6705–6716.

[39] Carlsson, J.O., Martin, P.M., (2010), "Chemical Vapor Deposition", Third Edit., Elsevier Ltd.

[40] Pottathara, Y.B., Grohens, Y., Kokol, V., Kalarikkal, N., Thomas, S., (2019), "Synthesis and Processing of Emerging Two-Dimensional Nanomaterials", Elsevier Inc., 1-29.

[41] Mannix, A.J., Kiraly, B., Hersam, M.C., Guisinger, N.P., (2017), "Synthesis and Chemistry of Elemental 2D Materials", Nat. Rev. Chem., 1, 1–15.

[42] Wang, Y., Zhang, S., Chen, H., Li, H., Zhang, P., Liang, G., Kong., J., (2012), "One-Pot Facile Decoration of Graphene Nanosheets with Ag Nanoparticles for Electrochemical Oxidation of Methanol in Alkaline Solution", Electrochem. Commun., 17 (1), 63–66.

[43] Mao, S., Pu, H., Chen, J., (2012), "Graphene Oxide and Its Reduction: Modeling and Experimental Progress", RSC Adv., 2 (7), 2643–2662.

[44] Shin, H.J., Kim, K.K., Benayad, A., Yoon, S.M., Park, H.K., et al., (2009), "Efficient Reduction of Graphite Oxide by Sodium Borohydride and Its Effect on Electrical Conductance", Adv. Funct. Mater., 19 (12), 1987–1992.

[45] Nair, L.S., Laurencin, C.T., (2007), "Silver nanoparticles: Synthesis and Therapeutic Applications", J. Biomed. Nanotechnol., 3 (4), 301–316.

[46] Tolaymat, T.M., El Badawy, A.M., Genaidy, A., Scheckel, K.G., Luxton, T.P., et al., (2010), "An Evidence-Based Environmental Perspective of Manufactured Silver Nanoparticle in Syntheses and Applications: A Systematic Review and Critical Appraisal of Peer-Reviewed Scientific Papers", Sci. Total Environ., 408 (5), 999–1006.

[47] Wang, H., Qiao, X., Chen, J., Wang, X., Ding, S., (2005), "Mechanisms of PVP in the Preparation of Silver Nanoparticles", Mater. Chem. Phys., 94 (2–3), 449–453.

[48] Mohanty, U.S., (2011), "Electrodeposition: A Versatile and Inexpensive Tool for The Synthesis of Nanoparticles, Nanorods, Nanowires, and Nanoclusters of Metals", J. Appl. Electrochem., 41 (3), 257–270.

[49] Li, G.R., Xu, H., Lu, X.F., Feng, J.X., Tong, Y.X., Su. C.Y., (2013), "Electrochemical Synthesis of Nanostructured Materials for Electrochemical Energy Conversion and Storage", Nanoscale, 5 (10), 4056–4069.

[50] Koehler, J.M., Visaveliya, N., Knauer, A., (2014), "Controlling formation and

assembling of nanoparticles by control of electrical charging, polarization, and electrochemical potential", Nanotechnol. Rev., 3 (6), 553–568.

[51] Rodríguez-Sánchez, M.L., Rodríguez, M.J., Blanco, M.C., Rivas, J., López-Quintela, M.A., (2005), "Kinetics and Mechanism of the Formation of Ag Nanoparticles by Electrochemical Techniques: A Plasmon and Cluster Time-Resolved Spectroscopic Study", J. Phys. Chem. B, 109 (3), 1183–1191.

[52] Yin, B., Ma, H., Wang, S., Chen, S., (2003), "Electrochemical Synthesis of Silver Nanoparticles under Protection of poly(N-vinylpyrrolidone)", J. Phys. Chem. B, 107 (34), 8898–8904.

[53] Khaydarov, R.A., Khaydarov, R.R., Gapurova, O., Estrin, Y., Scheper, T., (2009), "Electrochemical Method for the Synthesis of Silver Nanoparticles", J. Nanoparticle Res., 11 (5), 1193–1200.

[54] Boutonnet, M., Kizling, J., Stenius, P., Maire, G., (1982), "The Preparation of Monodisperse Colloidal Metal Particles from Microemulsions", Colloids and Surfaces, 5 (3), 209–225.

[55] Pileni, M.P., Motte, L., Petit, C., (1992), "Synthesis of Cadmium Sulfide in Situ in Reverse Micelles: Influence of the Preparation Modes on Size, Polydispersity, and Photochemical Reactions", Chem. Mater., 4 (2), 338–345.

[56] Baroli, B., (2010), "Penetration of Nanoparticles and Nanomaterials in the Skin: Fiction or Reality?", J. Pharm. Sci., 99 (1), 21–50.

[57] Kahlweit, M., Strey, R., Haase, D., Kunieda, H., Schmeling, T., Faulhaber, B., Borkoveç., M., Eicke, H.F., Busse, G., Eggers, F., Funck, T., Richmann, H., Magid, L., Söderman, O., Stilbs, P., Winkler, J., Dittrich, A., Jahn, W., (1987), "How to Study Microemulsions", J. Colloid Interface Sci., 118 (2), 436–453.

[58] Malheiro, A.R., Varanda, L.C., Perez, J., Villullas, H.M., (2007), "The Aerosol OT + n-butanol + n-heptane + water system: Phase Behavior, Structure Characterization, and Application to $Pt_{70}Fe_{30}$ Nanoparticle Synthesis", Langmuir, 23 (22), 11015–11020.

[59] Mooney, J.B., Radding, S.B., (1982), "Spray Pyrolysis Processing", Annu. Rev. Mater. Sci., 12 (1), 81–101.

[60] Yang, G.W., (2007), "Laser Ablation in Liquids: Applications in the Synthesis of Nanocrystals", Prog. Mater. Sci., 52 (4), 648–698.

[61] Choa, Y.-H., Yang, J.-K., Kim, B.-H., Jeong, Y.-K., Lee, J.-S., Nakayama, T., Sekino, T., Niihara, K., (2003), "Preparation and Characterization of Metal/Ceramic Nanoporous Nanocomposite Powders", J. Magn. Magn. Mater., 266 (1), 12–19.

[62] Hoffmann, N., (2012), "Photochemical Reactions of Aromatic Compounds and the Concept of The Photon as a Traceless Reagent", Photochem. Photobiol. Sci., 11 (11), 1613–1641.

[63] Albini, A., Fagnoni, M., (2010), "Handbook of Synthetic Photochemistry", Handb. Synth. Photochem.

[64] Albini, A., Fagnoni, M., (2018), "Photochemistry as a Green Synthetic Method BT - New Methodologies and Techniques for a Sustainable Organic Chemistry", Springer Netherlands, Dordrecht, 279–293.

[65] Saha, S., Pal, A., Kundu, S., Basu, S., Pal, T., (2010), "Photochemical Green Synthesis of Calcium-Alginate-Stabilized Ag and Au Nanoparticles and their Catalytic Application To 4-Nitrophenol Reduction", Langmuir, 26 (4), 2885–2893.

[66] Demazeau, G., (1999), "Solvothermal Processes: A Route to the Stabilization of New Material", J. Mater. Chem., 9 (1), 15–18.

[67] Inoue, M., (2013), "Solvothermal Synthesis of Metal Oxides", Academic Press, Oxford, 927–948.

[68] Burda, C., Chen, X., Narayanan, R., El-Sayed, M.A., (2005), "Chemistry and Properties of Nanocrystals of Different Shapes", Chem. Rev., 105 (4), 1025–1102.

[69] Daou, T.J., Pourroy, G., Bégin-Colin, S., Grenèche, J.M., Ulhaq-Bouillet, C., Pegare, P., Bernhardt, P., Leuvrey, C., Rogez, G., (2006), "Hydrothermal Synthesis of Monodisperse Magnetite Nanoparticles", Chem. Mater., 18 (18), 4399–4404.

[70] Branda, F., (2011), "The Sol-Gel Route to Nanocomposites", IntechOpen.

[71] Livage, J., Henry, M., Sanchez, C., (1988), "Sol-gel Chemistry of Transition Metal Oxides", Prog. Solid State Chem., 18 (4), 259–341.

[72] Angusmacleod, H., (2013), "Recent Developments in Deposition Techniques for Optical Thin Films and Coatings", Woodhead Publ. Ser. Electron. Opt. Mater., Woodhead Publishing, 3–25.

[73] Gedanken, A., (2004), "Using Sonochemistry for the Fabrication of Nanomaterials", Ultrason. Sonochem., 11 (2), 47–55.

[74] Suslick, K.S., Hammerton, D.A., Cline, R.E., (1986), "The Sonochemical Hot Spot", J. Am. Chem. Soc., 108 (18), 5641–5642.

[75] Suslick, K.S., Choe, S.-B., Cichowlas, A.A., Grinstaff, M.W., (1991), "Sonochemical Synthesis of Amorphous Iron", Nature, 353 (6343), 414–416.

[76] Lickiss, P.D., (1994), "Current Trends in Sonochemistry", J. Chem. Technol.

Biotechnol., 59 (2), 208.

[77] Hangxun, X., Zeiger, B.W., Suslick, K.S., (2013), "Sonochemical Synthesis of Nanomaterials", Chem. Soc. Rev., 42 (7), 2555–2567.

[78] Thomas, J.R., (1966), "Preparation and Magnetic Properties of Colloidal Cobalt Particles", J. Appl. Phys., 37 (7), 2914–2915.

[79] Kelly, C.H.W., Lein, M., (2016), "Choosing the Right Precursor for Thermal Decomposition Solution-Phase Synthesis of Iron Nanoparticles: Tunable Dissociation Energies of Ferrocene Derivatives", Phys. Chem. Chem. Phys., 18 (47), 32448–32457.

[80] Adner, D., Korb, M., Schulze, S., Hietschold, M., Lang, H., (2013), "A Straightforward Approach to Oxide-Free Copper Nanoparticles by Thermal Decomposition of a Copper(I) Precursor", Chem. Commun., 49 (61), 6855–6857.

[81] Patil, K.C., Chandrashekhar, G. V, George, M. V, Rao, C.N.R., (1968), "Infrared Spectra and Thermal Decompositions of Metal Acetates and Dicarboxylates", Can. J. Chem., 46 (2), 257–265.

[82] Hussain, I., Singh, N.B., Singh, A., Singh, H., Singh, S.C., (2016), "Green Synthesis of Nanoparticles and Its Potential Application", Biotechnol. Lett., 38 (4), 545–560.

[83] Ingale, A.G., Chaudhari, A.N., (2013), "Biogenic Synthesis of Nanoparticles and Potential Applications: An Eco-Friendly Approach", J. Nanomedicine Nanotechnol., 4 (2), 7.

[84] Kinayyigit, S., Philippot, K., (2014), "Organometallic Approach for the Synthesis of Noble Metal Nanoparticles: Towards Application in Colloidal and Supported Nanocatalysis", RSC Catal. Ser., 2014 47–82.

[85] Pan, C., Pelzer, K., Philippot, K., Chaudret, B., Dassenoy, F., Lacante, P., Casanove, M.J., (2001), "Ligand-Stabilized Ruthenium Nanoparticles: Synthesis, Organization, and Dynamics", J. Am. Chem. Soc., 123 (31), 7584–7593.

[86] Kinayyigit, S., Lara, P., Lecante, P., Philippot, K., Chaudret, B., (2014), "Probing the Surface of Platinum Nanoparticles with ^{13}CO by Solid-state NMR and IR Spectroscopies", Nanoscale, 6 (1), 539–546.

[87] Philippot, K., Chaudret, B., (2003), "Organometallic Approach to the Synthesis and Surface Reactivity of Noble Metal Nanoparticles", Comptes Rendus Chim., 6 (8), 1019–1034.

[88] Chaudret, B., Philippot, K., (2007), "Organometallic Nanoparticles of Metals or Metal Oxides", Oil Gas Sci. Technol., 62 (6), 799–817.

[89] Hall, J.L., (1987), "Cell Components", Phytochemistry, 26 (4), 1235–1236.

[90] Energy, U.S.D. of, (2002), "Fuel Cell Handbook, Sixth edition", Choice Rev. Online, 26 (11), 26-6292-26–6292.

[91] Litster, S., McLean, G., (2004), "PEM Fuel Cell Electrodes", J. Power Sources, 130 (1–2), 61–76.

[92] Shao, Y., Yin, G., Gao, Y., (2007), "Understanding and Approaches for the Durability Issues of Pt-Based Catalysts for PEM Fuel Cell", J. Power Sources, 171 (2), 558–566.

[93] Peighambardoust, S.J., Rowshanzamir, S., Amjadi, M., (2010), "Review of the Proton Exchange Membranes for Fuel Cell Applications", Int. J. Hydrogen Energy, 35 (17), 9349–9384.

[94] Lee, K., Zhang, J., Wang, H., Wilkinson, D.P., (2006), "Progress in The Synthesis of Carbon Nanotube and Nanofiber Supported Pt Electrocatalysts for PEM Fuel Cell Catalysis", J. Appl. Electrochem., 36 (5), 507–522.

[95] Alaswad, A., Olabi, A.G., Palumbo, A., Dassisti, M., (2016), "PEM Fuel Cell Cost Analysis During the Period (1998-2014)", Reference Module in Materials Science and Materials Engineering.

[96] Holton, O.T., Stevenson, J., (2013), "The Role of Platinum in Proton Exchange Membrane Fuel Cells", Platin. Met. Rev., 57 259–271.

[97] Wu, J., Yuan, X.Z., Martin, J.J., Wang, H., Zhang, J., Shen, J., Wu, S., Merida, W., (2008), " A Review of PEM Fuel Cell Durability: Degradation Mechanisms and Mitigation Strategies ", J. Power Sources., 184 (1), 104–119.

[98] Chen, Y., Sequeira, C.A.C., Chen, C., Wang, X., Wang, Q., (2003), "Metal Hydride Beds and Hydrogen Supply Tanks as Minitype PEMFC Hydrogen Sources", Int. J. Hydrogen Energy, 28 (3), 329–333.

[99] Song, C., Zhang, J., (2008), "Electrocatalytic Oxygen Reduction Reaction - PEM Fuel Cell Electrocatalysts and Catalyst Layers: Fundamentals and Applications", Springer London, 89–134.

[100] Zhang, J., (2008), "PEM Fuel Cell Electrocatalysts and Catalyst Layers: Fundamentals and Applications", Springer.

[101] Hu, P., Liu, K., Deming, C.P., Chen, S., (2015), "Multifunctional Graphene-Based Nanostructures for Efficient Electrocatalytic Reduction of Oxygen", J. Chem. Technol. Biotechnol., 90 (12), 2132–2151.

[102] Holton, O.T., Stevenson, J.W., (2013), "The Role of Platinum in Proton Exchange

Membrane Fuel Cells Evaluation of Platinum's Unique Properties for Use in both the Anode and Cathode of a Proton Exchange Membrane Fuel Cell", Platinum Met. Rev, 57 (4), 259–271.

[103] Ren, X., Lv, Q., Liu, L., Liu, B., Wang, Y., Liu, A., Wu, G., (2019), "Current Progress of Pt and Pt-based Electrocatalysts Used for Fuel Cells", Sustain. Energy Fuels, 4 (1), 15–30.

[104] Cao, M., Wu, D., (2014), "Recent Advances in the Stabilization of Platinum Electrocatalysts for Fuel-Cell Reactions", ChemCatChem, 6 26–45.

[105] Wikander, K., Ekström, H., Palmqvist, A., Lindbergh, G., (2007), "On the Influence of Pt Particle Size on The PEMFC Cathode Performance", Electrochim. Acta, 52 6848–6855.

[106] Page, C.H., (1977), "Electromotive Force, Potential Difference, and Voltage", Am. J. Phys., 45 (10), 978–980.

[107] Rao, C.R.K., Trivedi, D.C., (2005), "Chemical and Electrochemical Depositions of Platinum Group Metals and Their Applications", Coord. Chem. Rev., 249 (5–6), 613–631.

[108] Watanabe, M., Tsurumi, K., Mizukami, T., Nakamura, T., Stonehart, P., (1994), "Activity and Stability of Ordered and Disordered Co-Pt Alloys for Phosphoric Acid Fuel Cells", J. Electrochem. Soc., 141 (10), 2659–2668.

[109] Bregoli, L.J., (1978), "The Influence of Platinum Crystallite Size on the Electrochemical Reduction of Oxygen in Phosphoric Acid", Electrochim. Acta, 23 (6), 489–492.

[110] Kinoshita, K., (1990), "Particle Size Effects for Oxygen Reduction on Highly Dispersed Platinum in Acid Electrolytes", J. Electrochem. Soc., 137 (3), 845.

[111] Bonakdarpour, A., Wenzel, J., Stevens, D.A., Sheng, S., Monchesky, Löbel, R., Atanasoski, R.T., Schmoeckel, A.K., Vernstrom, G.D., Debe, M.K., (2005), "Studies of Transition Metal Dissolution from Combinatorially Sputtered, Nanostructured Pt[sub 1−x]M[sub x] (M = Fe, Ni; 0<x<1) Electrocatalysts for PEM Fuel Cells", J. Electrochem. Soc., 152 (1), A61.

[112] Zhang, J., Offer, G., (2008)., "PEM Fuel Cell Electrocatalysts and Catalyst Layers", Springer-Verlag London.

[113] Thompsett, D., (2010), "Pt Alloys as Oxygen Reduction Catalysts", Handb. Fuel Cells, Wiley Online Library.

[114] Strasser, P., (2010), "Dealloyed Pt Bimetallic Electrocatalysts for Oxygen Reduction", Handb. Fuel Cells, Wiley Online Library.

[115] Mukerjee, S., Srinivasan, S., Soriaga, M.P., McBreen, J., (1995), "Role of Structural and Electronic Properties of Pt and Pt Alloys on Electrocatalysis of Oxygen Reduction: An in Situ XANES and EXAFS Investigation", J. Electrochem. Soc., 142 (5), 1409–1422.

[116] Mukerjee, S., Srinivasan, S., (1993), "Enhanced Electrocatalysis of Oxygen Reduction on Platinum Alloys in Proton Exchange Membrane Fuel Cells", J. Electroanal. Chem., 357 (1), 201–224.

[117] Ralph, T., P, H., (2002), "Catalysis for Low Temperature Fuel Cells", Platin. Met. Rev., 46 117–135.

[118] Paffett, M.T., Beery, J.G., Gottesfeld, S., (1988), "Oxygen Reduction at $Pt_{0.65}Cr_{0.35}$, $Pt_{0.2}Cr_{0.8}$ and Roughened Platinum", J. Electrochem. Soc., 135 (6), 1431–1436.

[119] Jalan, V., Taylor, E.J., (1983), "Importance of Interatomic Spacing in Catalytic Reduction of Oxygen in Phosphoric Acid", J. Electrochem. Soc., 130 (11), 2299–2302.

[120] Min, M., Cho, J., Cho, K., Kim, H., (2000), "Particle Size and Alloying Effects of Pt-Based Alloy Catalysts for Fuel Cell Applications", Electrochim. Acta, 45 4211–4217.

[121] Nørskov, J.K., Rossmeisl, J., Logadottir, A., Lindqvist, L., Kitchin, J.R., Bligaard, T., Jonsoon, H., (2004), "Origin of the Overpotential for Oxygen Reduction at a Fuel-Cell Cathode", J. Phys. Chem. B, 108 (46), 17886–17892.

[122] Wikander, K., Ekströrn, H., Palmqvist, A.E.C., Lundblad, A., Holmberg, K., Lindbergh, G., (2006), "Alternative Catalysts and Carbon Support Material for PEMFC", Fuel Cells, 6 (1), 21–25.

[123] Marie, J., Berthon-Fabry, S., Chatenet, M., Chainet, E., Pirard, R., Lindbergh, G., (2007), "Platinum Supported on Resorcinol–Formaldehyde Based Carbon Aerogels for PEMFC Electrodes: Influence of the Carbon Support on Electrocatalytic Properties", J. Appl. Electrochem., 37 (1), 147–153.

[124] Yu, X., Ye, S., (2007), "Recent Advances in Activity and Durability Enhancement of Pt/C Catalytic Cathode in PEMFC: Part I. Physico-Chemical and Electronic Interaction Between Pt and Carbon Support, and Activity Enhancement of Pt/C Catalyst", J. Power Sources, 172 133–144.

[125] Wang, J., Yin, G., Shao, Y., Zhang, S., Wang, Z., Gao, Y., (2007), "Effect of Carbon Black Support Corrosion on the Durability of Pt/C Catalyst", J. Power Sources, 171 (2), 331–339.

[126] Saha, M., Neburchilov, V., Ghosh, D., Zhang, J., (2013), "Nanomaterials-Supported

Pt Catalysts for Proton Exchange Membrane Fuel Cells", Wiley Interdiscip. Rev. Energy Environ., 2.

[127] Geim, A.K., Novoselov, K.S., (2007), "The Rise of Graphene", Nat. Mater., 6 (3), 183–191.

[128] Ramachandran, R., Mani, V., Chen, S.-M., Ramiah, S., Lou, B., (2013), "Recent Trends in Graphene based Electrode Materials for Energy Storage Devices and Sensors Applications", Int. J. Electrochem. Sci., 8 11680–11694.

[129] Antolini, E., (2012), "Graphene as a New Carbon Support for Low-Temperature Fuel Cell Catalysts", Appl. Catal. B Environ., 123–124 52–68.

[130] Rao, C.N.R., Sood, A.K., (2012), "Graphene: Synthesis, Properties, and Phenomena", Wiley Online Library.

[131] Shao, Y., Zhang, S., Wang, C., Nie, Z., Liu, J., Wang, Y., Lin, Y., (2010), "Highly Durable Graphene Nanoplatelets Supported Pt Nanocatalysts for Oxygen Reduction", J. Power Sources, 195 (15), 4600–4605.

[132] Daş, E., Alkan Gürsel, S., Bayrakçeken Yurtcan, A., (2020), "Pt-Alloy Decorated Graphene as an Efficient Electrocatalyst for PEM Fuel Cell Reactions", J. Supercrit. Fluids, 165 104962.

[133] Barim, S.B., Bozbag, S.E., Yu, H., Kızılel, R., Aindow, M., Erkey, C., (2018), "Mesoporous Carbon Aerogel Supported PtCu Bimetallic Nanoparticles via Supercritical Deposition and Their Dealloying And Electrocatalytic Behaviour", Catal. Today, 310 166–175.

[134] Mani, P., Srivastava, R., Strasser, P., (2011), "Dealloyed Binary PtM_3 (M=Cu, Co, Ni) and Ternary $PtNi_3M$ (M=Cu, Co, Fe, Cr) Electrocatalysts for the Oxygen Reduction Reaction: Performance in Polymer Electrolyte Membrane Fuel Cells", J. Power Sources, 196 (2), 666–673.

[135] Yılmaz, M.S., Kaplan, B.Y., Gürsel, S.A., Metin, Ö., (2019), "Binary CuPt Alloy Nanoparticles Assembled on Reduced Graphene Oxide-Carbon Black Hybrid as Efficient and Cost-Effective Electrocatalyst for PEMFC", Int. J. Hydrogen Energy, 44 (27), 14184–14192.

[136] Monteverde Videla, A.H.A., Alipour Moghadam Esfahani, R., Peter, I., Specchia, S., (2015), "Influence of the Preparation Method on Pt_3Cu/C Electrocatalysts for the Oxygen Reduction Reaction", Electrochim. Acta, 177 51–56.

[137] Chen, D., Zhao, Y., Peng, X., Wang, X., Hu, W., Jing, C., Tian, S., Tian, J., (2015), "Star-like PtCu Nanoparticles Supported on Graphene with Superior Activity for Methanol Electro-Oxidation", Electrochim. Acta, 177 86–92.

[138] Alekseenko, A.A., Moguchikh, E.A., Safronenko, O.I., Guterman, V.E., (2018), "Durability of De-Alloyed PtCu/C Electrocatalysts", Int. J. Hydrogen Energy, 43 (51), 22885–22895.

[139] El-Deeb, H., Bron, M., (2015), "Electrochemical Dealloying of PtCu/CNT Electrocatalysts Synthesized by $NaBH_4$-Assisted Polyol-Reduction: Influence of Preparation Parameters on Oxygen Reduction Activity", Electrochim. Acta, 164 315–322.

[140] Garcia-Cardona, J., Sirés, I., Alcaide, F., Brillas, E., Centellas, F., Cabot, P.L., (2020), "Electrochemical Performance of Carbon-Supported Pt(Cu) Electrocatalysts for Low-Temperature Fuel Cells", Int. J. Hydrogen Energy, 45 (40), 20582–20593.

[141] Liu, Y., Chen, L., Cheng, T., Guo, H., Sun, B., Wang, Y., (2018), "Preparation and Application in Assembling High-Performance Fuel Cell Catalysts of Colloidal PtCu Alloy Nanoclusters", J. Power Sources, 395 66–76.

[142] Sun, J., Yu, G., Liu, L., Li, Z., Kan, Q., Hou, Q., Guan, J., (2014), "Core–Shell Structured Fe_3O_4@SiO_2 Supported Cobalt(ii) or Copper(ii) Acetylacetonate Complexes: Magnetically Recoverable Nanocatalysts for Aerobic Epoxidation of Styrene", Catal. Sci. Technol., 4 (5), 1246–1252.

[143] Gründer, Y., Lucas, C.A., (2016), "Surface X-Ray Diffraction Studies of Single Crystal Electrocatalysts", Nano Energy, 29 378–393.

[144] Ferraro, J.R., Nakamoto, K., Brown, C.W., (2003), "Introductory Raman Spectroscopy", Second Edition, Elsevier.

[145] Zgang, S.L., (2012), "Basic Knowledge of Raman Spectroscopy", Raman Spectrosc. Its Appl. Nanostructures, 1–17.

[146] Jung, J.H., Park, H.J., Kim, J., Hur, S.H., (2014), "Highly Durable Pt/Graphene Oxide and Pt/C Hybrid Catalyst for Polymer Electrolyte Membrane Fuel Cell", J. Power Sources, 248 1156–1162.

[147] Reina, A., Jia, X., Ho, J., Nezich, D., Son, H., Bulovic, V., Dresselhaus, M.S., Kong, J., (2009), "Large Area, Few-Layer Graphene Films on Arbitrary Substrates by Chemical Vapor Deposition", Nano Lett., 9 (1), 30–35.

[148] Nguyen, V.T., Le, H.D., Nguyen, V.C., Ngo, T.T.T., Le, D.Q., Nguyen, X.N., Phan, N.M., (2013), "Synthesis of Multi-Layer Graphene Films on Copper Tape by Atmospheric Pressure Chemical Vapor Deposition Method", Adv. Nat. Sci. Nanosci. Nanotechnol., 4 (3).

[149] Hofmann, S., (1986), "Practical Surface Analysis: State of the Art and Recent Developments in AES, XPS, ISS and SIMS", Surf. Interface Anal., 9 (1), 3–20.

[150] Alderucci, V., Pino, L., Antonucci, P.L., Roh, W., Cho, J., Kim, H., Cocke, D.L., Antonucci, V., (1995), "XPS Study of Surface Oxidation of Carbon-Supported Pt Catalysts", Mater. Chem. Phys., 41 (1), 9–14.

[151] Peng, J.C., Yang, B., Yang, Y., Zhao, Y.M., Zhao, Z.J., (2017), "Effects of Copper Doping and Electrolytic Corrosion on the Structure and Catalytic Performance of PtCu/C Catalysts", Mater. Res. Innov., 21 (1), 40–44.

[152] Okada, K., Kawai, J., Kotani, A., (1993), "Triple-Peak Feature of Cu 2p X-ray-Photoemission Spectrum in Copper Acetylacetonate", Phys. Rev. B, 48 (15), 10733–10738.

[153] Elgrishi, N., Rountree, K.J., McCarthy, B.D., Rountree, E.S., Eisenhart, T.T., Dempsey, J.L., (2018), "A Practical Beginner’s Guide to Cyclic Voltammetry", J. Chem. Educ., 95 (2), 197–206.

[154] Glass, J.T., Cahen, G.L., Stoner, G.E., (1989), "The Effect of Phosphoric Acid Concentration on Electrocatalysis", J. Electrochem. Soc., 136 (3), 656–660.

[155] Garsany, Y., Baturina, O.A., Swider-Lyons, K.E., Kocha, S.S., (2010), "Experimental Methods for Quantifying the Activity of Platinum Electrocatalysts for the Oxygen Reduction Reaction", Anal. Chem., 82 (15), 6321–6328.

[156] Shrestha, S., Ashegi, S., Timbro, J., Lang, C.M., Mustain, W.E., (2019), "ORR and Fuel Cell Performance of Pt Supported on N-Functionalized Mesoporous Carbon", ECS Trans., 41 (1), 1183–1191.

[157] Singh, V., Joung, D., Zhai, L., Das, S., Khondaker, S.I., Seal, S., (2011), "Graphene Based Materials: Past, Present and Future", Prog. Mater. Sci., 56 (8), 1178–1271.

[158] Ferrari, A.C., Basko, D.M., (2013), "Raman Spectroscopy as a Versatile Tool for Studying the Properties of Graphene", Nat. Nanotechnol., 8 (4), 235–246.

BIOGRAPHY

Zeynep Aydın is a Master of Science Student at Institute of Nanotechnology, Gebze Technical University. She graduated from Yıldız Technical University Chemistry Department in 2018. She studied on synthesis of gold nanoparticles via photochemical synthesis method with different photoinitiators and their use in determination of dopamine based on colorimetric diffrence during her undergraduate thesis. After beginning her MSc education at GTU, she started to work as Project Assistant at Nanocatalyst and Clean Energy Application Laboratory for one year, focusing in particular on the synthesis, characterization and application of bimetallic Pt-based nanoparticles for PEM fuel cell and amide hydrogenation processes. Currently, she is working at Şişecam R&D Center, Atmosferic Coating Technology Department as junior researcher.